**Institut für Physikalische Chemie**
**TU Dresden**

# Structural, electronic and optical properties of cadmium sulfide nanoparticles

von

Diplomchemiker Johannes Frenzel

2007

Institut für Physikalische Chemie
Fakultät Mathematik und Naturwissenschaften
Technische Universität Dresden

# Structural, electronic and optical properties of cadmium sulfide nanoparticles

Dissertation
zur Erlangung des
Doktorgrades der Naturwissenschaften
(Doctor rerum naturalium)

vorgelegt von
Diplomchemiker Johannes Frenzel
geboren in Dresden

Dresden 2007

Eingereicht am 17. Oktober 2006

1. Gutachter: Prof. Dr. Gotthard Seifert

2. Gutachter: Prof. Dr. Michael Springborg

3. Gutachter: Prof. Dr. Alexander Eychmüller

Verteidigt am 19. Dezember 2006

# Acknowledgment

This work has been completed under supervision of Prof. Dr. Gotthard Seifert at the Technische Universität Dresden and the Max-Planck-Institut für Chemische Physik fester Stoffe Dresden from 2003 to 2006. Special thanks go to

Prof. Dr. Gotthard Seifert for providing me the possibility to work on this interesting topic, guidance and motivation throughout this work, many fruitful and interesting discussions;

Prof. Dr. Michael Springborg for refereeing this work, discussions and the collaboration in the DFG Schwerpunktprogramm SPP 1072, Halbleiter- und Metallcluster als Bausteine für organisierte Strukturen;

Prof. Dr. Alexander Eychmüller for refereeing this work, discussions and the insight in the experimental nanoscience;

Prof. Dr. Yuri Grin for funding my work and conference participation during my work at the Max-Planck-Institut für Chemische Physik fester Stoffe;

Prof. Dr. Hélio Anderson Duarte from the Universidade Federal de Minas Gerais, Belo Horizonte and his group, for the opportunities and the hospitableness at my visits in Brazil;

Dr. Thomas Heine for providing me his efficient DFTB computer code, the possibility of participation in international collaboration, the introductions to molecular dynamics simulations and the Fortran90 programming language, the discussions and especially for companionship and friendship;

Dr. Jan-Ole Joswig for fruitful discussions and proof-reading this thesis, Dipl.-Chem. Robert Barthel for providing his `povray`-based visualisation tool and proof-reading this thesis, and Dipl.-Phys. Knut Vietze for supporting me in computer-technical questions;

Susanne Wohlgemuth for exercising patience, my parents for their support and Pete Josephs for the instruction in the *F. M. Alexander* technique;

Deutsche Forschungsgemeinschaft, DFG, through the SPP 1072 (project Sp 439/9-1) and Deutscher Akademischer Austauschdienst, DAAD, in cooperation with the Brazilian Agency Coordenação de Aperfeiçoamento de Pessoal de Nível Superior (CAPES) for financial support.

# Contents

# 1 Introduction

## 1.1 Semiconductor nanoparticles

Semiconductor and metal nanoparticles are in the focus of scientific research: It has been shown that size of these particles determines their properties [1, 2]. Because their unique electronic nature privileges them for a large variety of potential applications, e. g., biological labels [3, 4, 5], displays [6], solar cells [7, 8] and quantum-dot lasers [9, 10]. Examples of such systems are quantum-dots embedded in solid-state structures, particles on surfaces or clusters in the gas phase.

Beside zinc oxide and zinc sulphide the cadmium chalcogenides are the prototypical systems of the II–VI semiconductor compounds. Already for some hundred years cadmium sulphide (CdS) has been used as a pigment because of its colour. Solid CdS is a yellow material, due to its band gap of 2.58 eV [11]. It provides useful properties for optoelectronic devices, such as photosensitive and photovoltaic devices or as photoresistors [12].

At the nanometre scale these materials are at an intermediate level between atomic, molecular and bulk revealing new physical properties. In 1982 *Henglein* observed a blue shift in the absorption spectra of a colloidal solution of CdS with respect to the bulk band gap [13]. One year later, this effect was explained by *Brus*, who discovered its quantum mechanical nature [14]. Much progress has been achieved in the controlled synthesis of such nanoparticles with a narrow size distribution [15]. In 1993 *Murray, Noris* and *Bawendi* developed a method, which allowed the size selective synthesis of cadmium chalcogenide nanoparticles on a macroscopic scale [16]. This method opened the field for detailed investigations of the properties of these nanoparticles, as well as their application [1, 2].

In the size regime below approximately 10 nm the macroscopic physical properties of nanoparticles and nanocrystals are dominated by quantum mechanical rules. The spatial restriction of nanoparticle affects the wavelength of the electrons, which is reduced compared to the bulk. This effect is referred as quantum-confinement or quantum-size effect (QCE/QSE). The simplest model of this effect is the non-atomistic quantum mechanical problem of the "particle in a box". This is the basis for the effective mass approximation for the description of the electronic structure of these nanoparticles [14, 17, 18, 19, 20].

The second important effect of clusters, in particular of small nanoparticles, is the surface effect: The number of surface atoms is a large fraction of the total number of atoms in the nanoparticles. Even though the surface atoms are responsible for distinct contributions to the free energy and, thus, large changes in thermodynamic characteristics [21, 22]. In solu-

tion, the chemistry of the surface is determined by protective ligand. The optical processes of such semiconductor nanoparticles, especially the technologically interesting luminescence properties, are found to be affected by the structure of the surface [23, 24].

For instance dangling bonds partially or fully quench the luminescence quantum yield. This effect could be of interest for an application in solar cells. In contrast, a maximum luminescence quantum yield is obtained within a defect free surface, such as reported for single nanoparticles [25, 26, 27] and embedded structures, viz. core/shell systems [28, 29, 30, 31].

## 1.2 The Role of Theory

Theoretical studies help to understand and to overcome some of the problems in the production of semiconductor nanoparticles and in interpretation of their properties. An important part of the bulk properties and crystal structures is known through experiments. Detailed information of the atomic surface structure has to be, however, derived largely from quantum-mechanical models. The spectrum of applicable theoretical methods for atomic structure calculations ranges from high-accuracy techniques based on configuration interactions (CI) over the large realm of Hartree-Fock (HF) and density-functional theory (DFT) based methods to empirical force fields. Each class of methods has its particular domain of applicability, given by the system size, i. e., the number of basis functions, which can comfortably be handled at a desired level of accuracy.

Surfaces and interfaces are in general more complex than highly symmetric bulk systems and, therefore, have to be handled as large cluster models or periodic boundary conditions. This fact curtails the applicability of high-accuracy wavefunction and density-functional based methods alike. Classical potentials, on the other hand, allow the investigation of mesoscopic phenomena like crack propagation or surface roughening, but cannot provide a description of the electronic properties of the material. A compromise of the medium-accuracy level, which provides a quantum-mechanical description of chemical bonding sufficiently accurate to investigate the electronic and atomic structure of large-scale bulk, surface and interface systems, are the tight-binding methods, such as the one employed in this work. They may also give insights into system evolution and dynamics, e. g., during growth processes and phase transitions.

## 1.3 Outline

The subject of the present work is the investigation of the effects of surface saturation on the properties of CdS nanoparticles as one representative of the II-VI semiconductor systems. Due to the reasons given above, a particular density-functional based tight-binding method

(DFTB) is employed. The work is divided into two major parts: The first is addressed to the methodological and theoretical framework, while the second part focuses in the applications.

The calculation of the electronic and optical properties of CdS nanoparticles requires an accurate description of the unoccupied states. Therefore, the goal of part one is to systematically improve the DFTB formalism in the context of density-functional theory to achieve an improved charge-transfer description. The standard DFTB scheme uses a non-self-consistent solution of the *Kohn-Sham* equations, which excludes a recoupling of the density to wavefunctions. Additionally, density fluctuations have been considered by a self-consistent charge (SCC-DFTB) correction scheme using the non-self-consistent DFTB potentials. Hence, one objective of this thesis is to extend this standard DFTB scheme systematically by a self-consistent field (SCF) treatment within applying the DFTB approximations.

The background of density-functional theory is presented in Chapter 2 and the DFTB formulation is derived directly in Chapter 3. Time-dependent density-functional linear response theory (TD-DFRT) and the therefrom derived efficient calculation scheme – the $\gamma-$approximation – are introduced in short. The newly implemented extension of the standard DFTB method into an SCF formulation is given subsequently in Chapter 4.

Chapter 5 addresses questions related to the accuracy of the electronic structure description within the DFTB approximations. It will be shown that the standard DFTB scheme and its extension SCC-DFTB only calculate the occupied states correctly, but they fail for the unoccupied states. To correct this, the new SCF-DFTB is tested on CdS structures and compared to SCF-DFT calculations.

In the second part of this thesis, the DFTB scheme is applied to several problems of interest focusing on CdS nanoparticles. Chapter 6 addresses to structural aspects of the nanoparticles, especially their surface saturation. First, a saturation scheme is developed and tested. Then it is applied to generate the structures of saturated and non-saturated nanoparticles. These are subsequently investigated with the standard DFTB method using geometry optimisation techniques and molecular-dynamics simulations.

In the following two chapters, the properties of CdS nanoparticles with respect to quantum size effects (QSE) are focused. While the basic physics is believed to be largely understood, the dominating influence of the surface is lacking in these models. To shed light upon this, SCF-DFTB is applied to study the electronic structure of these nanoparticles, especially that of surface. This includes charge distributions, electronic density of states (DOS), HOMO-LUMO gap energies* and spatial distribution of the frontier orbitals, and finishes with the investigation of defects of the surface saturation (dangling bonds).

The optical properties of the CdS nanoparticles are investigated in Chapter 8. For the efficient calculation of the excitation energies and oscillator strengths of the relatively large structures the $\Gamma-$approximation is applied. Using this scheme the effect of surface saturation

*The HOMO-LUMO gap energy $\Delta_G$ is defined as energy difference of the lowest unoccupied molecular orbital (LUMO) $\epsilon_{LUMO}$ and the highest occupied molecular orbital (HOMO) $\epsilon_{LUMO}$: $\Delta_G = \epsilon_{LUMO} - \epsilon_{HOMO}$.

on the optical properties is studied. Furthermore, the impact of partial saturation and dangling bonds is investigated to obtain insight in the excitation process and subsequent conclusions for the luminescence properties.

The organisation of CdS nanoparticles in macroscopic crystals is addresses Chapter 9 to the organisation of CdS nanoparticles in macroscopic crystals. By a 3D organisation of the tetrahedrally shaped CdS particles into a diamond-like superstructure the photoluminescence quantum yield is improved compared to single nanoparticles in solution. In this context the structures and electronic properties are investigated to gain further insight.

Supplementary material is provided in the appendices: In Appendix A the systematic of the structural build-up of CdS nanoparticles in different series is reviewed. Supplementary figures of this work are collected in Appendix B.

# 2 Density-functional theory

## 2.1 Fundamentals of quantum-mechanical calculations

The interactions of electrons and nuclei in the non-relativistic quantum mechanical theory are described by the *Schrödinger* equation [32, 33, 34]:

$$\mathbb{H}\,\Phi = i\hbar\frac{\partial}{\partial t}\,\Phi\,, \tag{2.1}$$

where the wavefunction $\Phi$ is explicitly time dependent:

$$\Phi = \Phi(\mathbf{R}_1, \mathbf{R}_2, \ldots, \mathbf{R}_{N_K}; \mathbf{x}_1, \mathbf{x}_2, \ldots, \mathbf{x}_{N_E}; t). \tag{2.2}$$

The vectors $\mathbf{R}_\alpha$ denote the coordinates of the nuclei $N_K$ and $\mathbf{x}_\nu$ the coordinates and spins of the electrons $N_E$.

In the case of a time-independent potential the wavefunction $\Phi$ can be factorised into two terms:

$$\Phi(x,t) = \Psi(x)A(t). \tag{2.3}$$

The first term, depends only on time, the second one, depends on positions and spins. The result of this factorisation is the stationary many-particle *Schrödinger* equation:

$$\mathbb{H}\,\Psi = E\,\Psi\,. \tag{2.4}$$

The *Hamilton* operator $\mathbb{H}$ is a differential operator that includes all internal and external interactions of the system reads as follows:

$$\begin{aligned}\mathbb{H} = &\underbrace{\sum_{\nu=1}^{N} -\frac{1}{2}\nabla_\nu^2}_{T_e} + \underbrace{\frac{1}{2}\sum_{\mu}^{N}\sum_{\nu\neq\mu}^{N}\frac{1}{|\mathbf{r}_\mu - \mathbf{r}_\nu|}}_{V_e} + \underbrace{\sum_{\alpha=1}^{N_K} -\frac{1}{2}\nabla_\alpha^2}_{T_K} \\ &+ \underbrace{\frac{1}{2}\sum_{\alpha}^{N_K}\sum_{\beta\neq\alpha}^{N_K}\frac{Z_\alpha Z_\beta}{|\mathbf{R}_\alpha - \mathbf{R}_\beta|}}_{V_K} - \underbrace{\sum_{\nu}^{N}\sum_{\alpha}^{N_K}\frac{Z_\alpha}{|\mathbf{r}_\nu - \mathbf{R}_\alpha|}}_{V_{e-K}}\,,\end{aligned} \tag{2.5}$$

with the kinetic energy $T_e$ of the $N_E$ electrons, the potential energy $V_e$, of the electron-electron interactions and the electron-nuclei's interaction $V_{e-K}$ with the nuclear charge $Z_\alpha$, form the electronic *Hamilton* operator $\mathbb{H}_e$. In a similar way, the *Hamilton* operator $\mathbb{H}_K$ is constructed for the motion of the $N_K$ nuclei $T_K$ and the nuclei-nuclei interaction $V_K$.

## 2.2 Quantum chemical methods

Quantum chemical methods are mainly based on the *Born-Oppenheimer* approximation. This approach consists of the separation in the fast electron and the slow nuclear motion enables us to decouple their wave functions [35]. The result leads to is the pure electronic *Schrödinger* equation:

$$\mathbb{H}_{\mathrm{e}}\Psi_e = E_k\Psi_e \ , \tag{2.6}$$

where $\Psi_e$ represents the electron wavefunction in the field of the nuclei. Hence, the *Born-Oppenheimer* approximation is often named **adiabatic** approximation. All calculations, which are performed in this work, base on this approximation. Since, in the following the electronic wavefunction is considered the corresponding indices are omitted.

The *Schrödinger* equation (2.6) covers a many-particle problem. With *Hartree's* product approach its solution is simplified by the wavefunction of the $N$ electrons $q_i$:

$$\Psi(\{q_i\}) = \prod_{j=1}^{N} \psi_j \ . \tag{2.7}$$

This product of $N$ single particle wavefunction describes the molecular orbitals (MO) $\psi_j$. Because of the elementary property of the electron (*Pauli* principle), *Slater* determinants have to be introduced. They concern simple anti-symmetric permutations of the *Hartree* function, which covers a specific choice of the electronic orbitals – a configuration. The *Slater* determinants of all configurations form complete set of functions, in which the wavefunction $\Psi$ can be expanded. A possible and nowadays well-defined *ab initio* method for the solution of the *Schrödinger* equation is the approach following *Hartree* and *Fock*, the so-called HF method. This method determines that configuration (*Slater* determinant), which represents the best approximation for the total wavefunction within the anti-symmetrised product approach.

However, through the single-determinant representation the quantitative accuracy of the HF method is not guaranteed. Therefore, so-called post HF methods are applied, e. g., the configuration-interaction (CI), which uses finite number of configurations for the description of the wavefunction. Another method is the *Møller* and *Plesset* procedure (MP2, MP4) [36]. The *post* HF methods require high computational costs, which can exceed those of a DFT calculation by some orders of magnitude. HF methods are inappropriate for the description of small band gap materials, e. g., metals.

HF and derived methods* represent *ab initio* methods, in which no empirical parameters enter. The only used parameters are the type and the number of the atoms, and the electron number.

*See e. g., Ref. [37]

## 2.3 Density-functional Theory[38, 39]

The DFT is based upon the work of *Hohenberg, Kohn* and *Sham* [40, 41]. The advantage of this theory is the simplified representation of the electronic structure of the investigated system. The exact knowledge of the many-particle wavefunction is not necessary. *Thomas* and *Fermi* proposed [42, 43, 44, 45], that instead, the many-electron system is entirely described by the time-averaged probability density of all electrons. This is called the electron density $\varrho(\mathbf{r})$. It reduces the N-electron problem, with formal exactness, to 3 instead of $3N$ variables only.

The important equations within the density-functional theory are the expressions of the ground-state energy as functional of the electron density (*Hohenberg-Kohn* theorem), and the equations for the calculation of the wavefunction (*Kohn-Sham* equations). These equations result from the minimisation of the total energy expression of a many-particle system and are solved self-consistently. The variety of applications of density-functional theory encompasses all scopes of the theoretical description of molecules, clusters, solid-state and liquids.

The following sections comprise a summary of fundamentals of density-functional theory– the *Hohenberg-Kohn* theorem and the *Kohn-Sham* equations. Approximations for the exchange-correlation potential and concepts of basis sets are discussed.

### 2.3.1 The Hohenberg-Kohn theorems

The basic principle of DFT are the *Hohenberg-Kohn* theorems[40]:

> [1.] If the **electron charge density** $\varrho(\mathbf{r})$ of an $N$-electron system in a non-degenerated ground state is given, then the external potential $V_{\text{ext}}(\mathbf{r})$ is uniquely defined, when this density adjusts itself on it. The total (electronic) energy $E$ of this system is a unique functional of $\varrho(\mathbf{r})$.

$$\varrho(\mathbf{r}) = N \int \Psi_0(\mathbf{x}, \mathbf{x}_2 \ldots \mathbf{x}_N)\ \Psi_0^*(\mathbf{x}, \mathbf{x}_2 \ldots \mathbf{x}_N)\ \mathrm{d}\mathbf{r}_2 \ldots\ \mathrm{d}\mathbf{r}_N \tag{2.8}$$

$$E = E[\varrho(\mathbf{r})]. \tag{2.9}$$

> The total number of electrons of the system of interest is also defined by $\varrho(\mathbf{r})$:

$$N = \int \varrho(\mathbf{r})\ \mathrm{d}\mathbf{r} \tag{2.10}$$

> [2.] When starting from the exact electron density $\varrho(\mathbf{r})$ a variation of the of the ground-state electron density, $\tilde{\varrho}(\mathbf{r}) = \varrho(\mathbf{r}) + \delta\varrho(\mathbf{r})$, result a positive change of the total ground-state energy:

$$E[\tilde{\varrho}(\mathbf{r})] > E[\varrho(\mathbf{r})]\ . \tag{2.11}$$

The variational principle holds for the energy as density functional, because the variation of the electron density does not change the number of electrons in the system:

$$\int \tilde{\varrho}(\mathbf{r})\ \mathrm{d}\mathbf{r} = \int \varrho(\mathbf{r})\ \mathrm{d}\mathbf{r}\ . \tag{2.12}$$

The starting point of DFT is the stationary, time-independent many-particle *Schrödinger* equation (2.1). In consideration with the *Born-Oppenheimer* approximation, the total energy of an $N$-electron system results from the expectation value of the electronic *Hamilton* operator $\mathsf{H}_e$:

$$E = \left\langle\ \mathsf{H}_e\ \right\rangle\ = \left\langle\ T_\mathrm{e}\ \right\rangle\ + \int V_\mathrm{ext}(\mathbf{r})\ \varrho(\mathbf{r})\ \mathrm{d}\mathbf{r}\ +\ \left\langle\ V_\mathrm{e}\ \right\rangle\ , \tag{2.13}$$

where $\mathsf{H}_e$, $T_\mathrm{e}$, $V_\mathrm{ext}(\mathbf{r})$ and $V_\mathrm{e}$ have been defined in Section 2.1 in Eq. (2.5). In DFT the electron-electron interaction is written:

$$\left\langle\ V_\mathrm{e}\ \right\rangle\ = \frac{1}{2}\iint \frac{\varrho(\mathbf{r}')\varrho(\mathbf{r})}{|\mathbf{r}'-\mathbf{r}|}\ \mathrm{d}\mathbf{r}'\ \mathrm{d}\mathbf{r}\ +\ E_\mathrm{xc}\ , \tag{2.14}$$

with the exchange correlation energy $E_\mathrm{xc}$:

$$E_\mathrm{xc} = \sum_s \int \varrho_s(\mathbf{r})\epsilon_\mathrm{xc}[\varrho(\mathbf{r},s)]\ \mathrm{d}\mathbf{r} \tag{2.15}$$

and the so called exchange correlation energy per particle $\epsilon_\mathrm{xc}$ [38, 46]. The external potential $V_\mathrm{ext}(\mathbf{r})$ is determined by the *Coulomb* potentials of the nuclei of the system and may, moreover, contain additional potentials, e. g., electrostatic or gravitational.

### 2.3.2 The Kohn-Sham equations

The *Schrödinger* equation of an $N$-electron system can be written as $N$ coupled differential equations of second order. In DFT it is transformed to $N$ differential equations of a non-interacting system, the so-called *Kohn-Sham* equations [41]. This approach of *Kohn* and *Sham* replaces the electron-electron interaction by an external potential in such a way, that the electronic density and, thus, the total energy of the system keep unchanged. This external potential is the exchange-correlation potential $V_\mathrm{xc}$ and the *Kohn-Sham* equations are single-particle equations similar to the HF method:

$$\left[-\frac{1}{2}\nabla^2 + V_\mathrm{ext}(\mathbf{r}) + \int \frac{\varrho(\mathbf{r}')}{|\mathbf{r}'-\mathbf{r}|}\ \mathrm{d}\mathbf{r} + V_\mathrm{xc}(\mathbf{r})\right]\phi_\nu(\mathbf{r}) = \varepsilon_\nu\phi_\nu(\mathbf{r})\ . \tag{2.16}$$

the integral the *Hartree* potential $V_H$. The complete expression in the brackets is referred to as *Kohn-Sham* operator (single-particle operator). The three potentials are summarised to the effective potential $V_\mathrm{eff}$. Now, the ground-state energy of the electronic system reads

$$E_e[\varrho(\mathbf{r},s)] = \sum_\nu^N \varepsilon_\nu - \frac{1}{2}\iint \frac{\varrho(\mathbf{r})\varrho(\mathbf{r}')}{|\mathbf{r}-\mathbf{r}'|}\ \mathrm{d}\mathbf{r}'\ \mathrm{d}\mathbf{r} + E_\mathrm{xc}[\varrho] - \int \varrho(\mathbf{r})V_\mathrm{xc}[\varrho(\mathbf{r},s)]\ \mathrm{d}\mathbf{r}\ . \tag{2.17}$$

The solution of the *Kohn-Sham* equations is only possible iteratively, e. g., by using the self-consistent-field technique (SCF). In a first step, a *Kohn-Sham* potential is calculated from a starting density. This potential is used to obtain a new density, which again is inserted into the *Kohn-Sham* equations, etc.

### 2.3.3 The exchange-correlation potential

The exchange-correlation potential is uniquely defined as the functional derivative

$$V_{\mathrm{xc}}[\varrho_s(\mathbf{r})] = \frac{\delta E_{\mathrm{xc}}}{\delta \varrho_s(\mathbf{r})} \; . \tag{2.18}$$

contains the contributions of the electron-electron interactions, the self-interaction correction and the part of the kinetic energy which is not described within the non-interacting system. Thus, the calculation of $V_{\mathrm{xc}}$ requires approximations.

A possible approximation for the exchange-correlation potential is represented by the $\mathrm{X}_\alpha$ method

$$V_{\mathrm{xc}}^{(X_\alpha)}(\mathbf{r}) = -3\alpha \sqrt[3]{\frac{3\varrho(\mathbf{r})}{8\pi}} \; . \tag{2.19}$$

Based on the HF method, *Slater* [47] proposes $\alpha = 1$, whereas *Gaspar* gives $\alpha = \frac{2}{3}$ (based on *Thomas-Fermi*) [48]. Later on, optimal values for $\alpha$ were calculated for all elements of the periodic system [49].

#### The local density approximation

Within the local density approximation (LDA), the local exchange-correlation potential is obtained from the exchange-correlation energy per particle ${\epsilon_{\mathrm{xc}}}^{\mathrm{hom}}$ of a homogeneous electron gas with the same density. Therein, a functional relation on the basis of quantum-Monte-Carlo simulations (QMC) [50] for the exchange-correlation energy is approximated to:

$$E_{\mathrm{xc}} \approx \int {\epsilon_{\mathrm{xc}}}^{\mathrm{hom}} \, \varrho(\mathbf{r}) \; \mathrm{d}\mathbf{r} \; . \tag{2.20}$$

The advantage of the LDA is its computational efficiency. In case of homogeneous densities, the LDA exhibits high accuracy. In general, the LDA over-estimates the binding energies and underestimated band-gap energies. This overbinding effect is caused by inhomogeneous densities, e. g., spin-polarisation in free atoms. In this case, the approximate description can partially be corrected with an unrestricted approach – the local spin-density approximation (LSDA):

$$V_{\mathrm{xc}} = V_{\mathrm{xc}}(\varrho_\uparrow(\mathbf{r}), \varrho_\downarrow(\mathbf{r})) \; . \tag{2.21}$$

The first LDA approach was introduced by *Hedin* and *Lundqvist* [51]. Nowadays, the formulation of *Vosko, Wilk* and *Nusair* (VWN) [52] is used as standard solution for the L(S)DA.

Improvements, especially of the convergence and for the binding energies, came up with the generalised gradient approximation (GGA) by *Pedrew* [53]. Therein, the exchange-correlation potential has the following form:

$$V_{\mathrm{xc}}(\mathbf{r}) = V_{\mathrm{xc}}(\varrho(\mathbf{r}), \nabla\varrho(\mathbf{r}), \Delta\varrho(\mathbf{r}), \ldots). \tag{2.22}$$

The coefficients for this expansion are obtained from reference calculations on test sets of molecules, e. g., PW86 or BLYP [54, 55], or from physical considerations, e. g., in PW91 [56, 57] or the BPE-functional [58]. The gradient approximation (GA) corrects the exchange-correlation potential of the LDA by a *Taylor* expansion of the position variables of the electron density – the gradient of the electron density $\nabla\rho(\mathbf{r})$. This expansion is not convergent.

The advantages of the GGA are the more precise binding- and atomisation energies. The gain of exactness demands the time-consuming computation of the density gradients.

In this work the LDA is has been used if not stated otherwise.

## 2.4 The LCAO method

For the solution of the *Kohn-Sham* equations the molecular orbitals (MO) are typically represented by a linear combination (LC) of a finite set of appropriate functions, e. g., GTO[†] or STO[‡]. Both, the type and the number of these functions are determining the accuracy of the *Kohn-Sham* orbitals.

The LCAO method uses atomic orbitals (AO) $\phi$ as basis functions, with the aim to minimise the number of basis functions *Slater*-type functions (STO's) are most commonly used for the representation of the AO's:

$$\phi_{lm} = \sum_{p=1}^{N_p} A_{np} r^{l+p-1} e^{\xi_n r} Y_{lm}\left(\frac{\mathbf{r}}{r}\right) \tag{2.23}$$

with *Slater* exponent $\xi_n$, the spherical harmonic $Y_{lm}$. The radial symmetric part contains $(N_p - 1)$ contributions of different angular moments. The expansion coefficients $A_{np}$ are obtained from calculations of single atoms.

Details on the LCAO-DFT method are given within Ref. [59]. The DFTB method, an approximated LCAO method, is described in the following Chapter.

[†]gaussian type orbitals (LCGTO)
[‡]slater type orbitals (LCSTO)

# 3 The density-functional tight-binding Method

The density-functional tight-binding (DFTB) is the most prevalently used method in this work. Originally, it was developed by *Seifert* and co-workers [60] for the efficient calculation of small molecules. Numerical integration and iterative solving algorithms are avoided [61, 62, 63]. The mathematical approach in solving the *Kohn-Sham* equations corresponds to that of the non-orthogonal tight-binding methods (see review article [64]). In contrast to the empirical TB methods all matrix elements in DFTB are obtained from DFT-LDA calculations. The estimation procedure of the matrix elements is generically valid and, therefore, the method becomes transferable for all elements of the periodic system.

From its origins, that date back more than 20 years by now, the DFTB method was systematically improved. By now, this comprise a self-consistent-charge extension (SCC-DFTB) as derived from second-order expansion of the *Kohn-Sham* energy with respect to atomic charge fluctuations [65], a spin-dependent formulation [66], and a time-dependent description of excited states [67]. Furthermore, it was largely prompted by demands that became evident in course of implementation and application to real systems, such as calculation of vibrational properties [68], infrared and *Raman* intensities [69], calculation of spatial charge densities providing links to scanning tunnelling microscopy (STM) measurements on crystalline surfaces [70], nuclear magnetic resonance (NMR) shifts [71, 72, 73] and linear-scaling formulation of the secular problem [74].

The standard DFTB and SCC-DFTB schemes are excellently qualified for the determination of geometries and calculation of electronic properties, binding energies and relative energies of numerous systems, cf. e. g., [71, 73, 75, 76, 77, 78, 79, 80, 81, 82, 83, 84, 85, 86, 87].

At the moment, there are two major computer-codes available which provide the DFTB method: One is `dftb`$^+$ [88], a successor of the old `dftb`-code, maintained by the *Frauenheim* group at the Universität Bremen. The second is part of the `deMon` DFT-package [89], maintained by *Thomas Heine* from the Technische Universität Dresden.

In this work, the `deMon` package was applied and the DFTB part have been extended by an efficient implementation of the approximate method for the time-dependent description of excited states (cf. Ref. [67] and Section 3.8).

## 3.1 The Kohn-Sham equations in DFTB

In the DFTB formalism the *Kohn-Sham* single-particle wavefunction $\psi_i$ are represented as LCAO:

$$\psi_i(\mathbf{r}) = \sum_{\nu} c_{\nu i}\phi_\nu(\mathbf{r} - \mathbf{R}_\alpha) \tag{3.1}$$

with the nuclei $\alpha$ centred at $\mathbf{R}_\alpha$. The atomic orbitals $\phi_\nu$ are determined by self-consistent calculations of the neutral atoms. Using this approach the *Kohn-Sham* equations can be transformed to the secular problem:

$$\sum_{\nu=1}^{N} c_{\nu i}\left(H_{\mu\nu} - \varepsilon_i S_{\mu\nu}\right) = 0; \qquad \forall\, i, \mu \tag{3.2}$$

with the Hamiltonian matrix elements denoted by $H_{\mu\nu}$ (*Kohn-Sham* matrix) and the non-orthogonal overlap matrix elements by $S_{\mu\nu}$

$$S_{\mu\nu} = \left\langle\, \phi_\mu \,\middle|\, \phi_\nu \,\right\rangle \tag{3.3}$$

$$H_{\mu\nu} = \left\langle\, \phi_\mu \,\middle|\, \hat{T} + V_{\text{eff}}(\mathbf{r}) \,\middle|\, \phi_\nu \,\right\rangle . \tag{3.4}$$

To achieve a **two-centre** representation for the Hamiltonian matrix elements, the **non self-consistent** effective (*Kohn-Sham*) potential $V_{\text{eff}}(\mathbf{r})$ is formally decomposed into atomic-like contributions, viz. superposition of potentials of neutral pseudo-atoms [60, 61].

The solution of the *Kohn-Sham* equations in the form of the secular problem (3.2) results in approximate molecular orbitals $\psi(\mathbf{r})$ and, thus, the density $\varrho(\mathbf{r})$ of the investigated system. From these equations, the total energy $E_{\text{tot}}$ and the forces of the system $\mathbf{F}_\alpha$ acting on a nucleus $\alpha$ can be obtained by introducing repulsive pair potentials, as described in Sections 3.4 and 3.5.

## 3.2 The effective potential

The effective potential $V_{\text{eff}}(\mathbf{r})$ of an ensemble of nuclei and electrons with the known or approximated exchange-correlation potential $V_{\text{xc}}$ and density $\varrho(\mathbf{r})$ reads:

$$V_{\text{eff}}(\mathbf{r}) = V_{\text{ext}}(\mathbf{r}) + V_{\text{H}}(\mathbf{r}) + V_{\text{xc}}(\mathbf{r}) . \tag{3.5}$$

It can be represented by an angular-momentum expansion over all $N_K$ atoms $\alpha$ in the system [90]:

$$V_{\text{eff}}(\mathbf{r}) = \sum_{\alpha=}^{N_K} V_{\text{eff}}^{(\alpha)}(\mathbf{r}) \tag{3.6}$$

$$= \sum_{\alpha=1}^{N_K}\sum_{l=1}^{\infty}\sum_{m=-l}^{l} V_{lm}^{(\alpha)}(r_\alpha) Y_{lm}\left(\frac{\mathbf{r}_\alpha}{r_\alpha}\right) \qquad \text{with } \mathbf{r}_\alpha = \mathbf{r} - \mathbf{R}_\alpha. \tag{3.7}$$

In this expansion of the effective potential, all non-spherical contributions ($l, m \neq 0$) are neglected, because the neutral atoms are centre-symmetric.

Analogous to the cellular method by *Wigner* and *Seitz* [91, 92], it is further assumed, that the nucleus $\beta$ in the region of nucleus $\alpha$ is completely screened. The expression of the effective potential from (3.6) can be further approximated by neglecting all crystal-field terms and, in analogy, the three centre contributions [60]:

$$\left\langle \mu \left| V_{\text{eff}}^{(\beta)}(\mathbf{r}) \right| \nu \right\rangle \approx 0 \,, \qquad \mu, \nu \in \{\alpha\} \tag{3.8}$$

$$\left\langle \mu \left| V_{\text{eff}}^{(\alpha)}(\mathbf{r}) \right| \nu \right\rangle \approx 0 \,, \qquad \mu, \nu \ni \{\alpha\} \tag{3.9}$$

Now the *Kohn-Sham* matrix elements reduce to:

$$H_{\mu\nu} = \begin{cases} \left\langle \mu \left| -\frac{1}{2}\nabla^2 + V_{\text{eff}}^{(\alpha)}(\mathbf{r}) + V_{\text{eff}}^{(\beta)}(\mathbf{r}) \right| \nu \right\rangle \,, & \mu \in \{\alpha\}, \nu \in \{\beta\} \\ \left\langle \mu \left| -\frac{1}{2}\nabla^2 + V_{\text{eff}}^{(\alpha)}(\mathbf{r}) \right| \nu \right\rangle \,, & \mu, \nu \in \{\alpha\}. \end{cases} \tag{3.10}$$

Within this two-centre approximation the effective potential $V_{\text{eff}}$ is then composed of the superposition of atomic effective potentials. These are determined by the self-consistent calculation of modified atoms (pseudo atoms).

## 3.3 The atomic effective potential

In DFTB the atomic contributions to the effective potential $V_{\text{eff}}^{(\alpha)}$ and the electronic density $\varrho_\alpha^0(\mathbf{r}) = \varrho_\alpha^0(r)$ are chosen to be central symmetric. This Section 3.3 contains only single-atom calculations and, therefore, the atomic index $\alpha$ will be neglected. The atomic *Kohn-Sham* operator $\hat{H}$ reads now:

$$\begin{aligned} \hat{H} &= \hat{T} \;+\; V_{\text{eff}}(r) \;+\; V_{\text{add}}(r) \\ &= \hat{T} \;+\; V_{\text{ext}}(r) + V_{\text{H}}(\varrho(r)) + V_{\text{xc}}[\varrho(r)] + V_{\text{add}}(r) \\ &= -\frac{1}{2}\nabla^2 - \frac{Z}{r} + \int \frac{\varrho(r')}{|\mathbf{r} - \mathbf{r}'|}\, \mathrm{d}^3\mathbf{r}' + V_{\text{xc}}[\varrho(r)] + \left(\frac{r}{r_0}\right)^n . \end{aligned} \tag{3.11}$$

Herein the effective potential of the pseudo atom is the **self-consistent** potential of a free, **neutral** atom modified by an additional additive harmonic contribution $V_{\text{add}}$ [93, 59]:

$$V_{\text{add}}(r) = \left(\frac{r}{r_0}\right)^n . \tag{3.12}$$

This harmonic auxiliary potential $V_{\text{add}}(r)$ compresses the density and the effective potential $V_{\text{eff}}$ as well as the wavefunctions of the pseudo atom compared to the free atom case. Since the densities of free atoms are too diffuse (long-ranged potentials), the compressed densities anticipate the density modification of free atoms due to a molecular or crystalline environment. The harmonic auxiliary potential is characterised by its cut-off radius $r_0$ and

its exponent $n$. For the latter $n = 2$ or $n = 4$ are used. For $r_0$ it can be shown within self-consistent LCAO calculations, that its choice does not change the results of the calculations when it is chosen greater than

$$r_0 = 2r_c \; . \tag{3.13}$$

Here, $r_c$ is the double covalent radius of the atom. In this work Eq. (3.13) and $n = 2$ are chosen.

Due to the contraction of the effective potential – and the wavefunction– the single-particle energies are changed. In order to ensure the correct calculation of the dissociation energies the single-particle energies of the free, neutral and spherical atoms $\varepsilon_\mu^{0,\text{free}}$ are used for the calculation of the *Kohn-Sham* matrix elements [61]:

$$H_{\mu\nu} = \begin{cases} \left\langle \mu \right| -\frac{1}{2}\nabla^2 + V_{\text{eff}}^{(\alpha)}(\mathbf{r}) + V_{\text{eff}}^{(\beta)}(\mathbf{r}) \left| \nu \right\rangle \; , & \mu \in \{\alpha\}, \nu \in \{\beta\}, \alpha \neq \beta \\ \varepsilon_\mu^{0,\text{free}} \; , & \mu = \nu \\ 0 \; , & \text{otherwise.} \end{cases} \tag{3.14}$$

The results of the atomic calculations are the atomic orbitals and effective potential. These are used to build the Hamiltonian and overlap matrices.

## 3.4 The total energy in DFTB

The total energy of an electronic system within the DFT scheme is given by Eq. (2.17). Using the density calculated with DFTB and the atomic effective potential the total energy in DFTB is given by:

$$\begin{aligned} E_{\text{tot}}[\varrho] = &\sum_i \varepsilon_i n_i - \frac{1}{2}\sum_{\alpha,\beta} \int V_{\text{eff}}^{(\alpha)}(\mathbf{r}) \varrho_\beta(\mathbf{r}) \; \mathrm{d}^3\mathbf{r} - \frac{1}{2}\sum_{\alpha,\beta} \int \frac{Z_\alpha \varrho_\beta(\mathbf{r})}{r_\alpha} \; \mathrm{d}^3\mathbf{r} \\ &+ \frac{1}{2}\sum_{\alpha \geq \beta} \int V_{\text{xc}}[\varrho_\alpha(\mathbf{r}), \varrho_\beta(\mathbf{r})] \; \mathrm{d}^3\mathbf{r} + \frac{1}{2}\sum_{\alpha \neq \beta} \frac{Z_\alpha Z_\beta}{R_{\alpha\beta}}, \end{aligned} \tag{3.15}$$

with

$$R_{\alpha\beta} = \left| \, \mathbf{R}_\alpha \, - \, \mathbf{R}_\beta \, \right| . \tag{3.16}$$

However, calculating the ground state-energy through this Eq. (3.15) would cause unproportional high computational effort* compared to the DFTB approximations. Within a further approximation all terms except the sum of the eigenvalues are written as a repulsive

*The contribution of the exchange-correlation potential is calculated by numerical integration over the whole position space with the relaxed density of the system.

potential $U_{\text{rep}}$ [94]:

$$\sum_{\alpha\neq\beta} U_{\text{rep}}(R_{\alpha\beta}) := \sum_{\alpha\neq\beta} U_{\text{rep}}(\alpha,\beta,R_{\alpha\beta}) \tag{3.17}$$

$$\begin{aligned} &= -\frac{1}{2}\sum_{\alpha,\beta}\int V_{\text{eff}}^{(\alpha)}(\mathbf{r})\varrho_\beta(\mathbf{r})\,\mathrm{d}^3\mathbf{r} - \frac{1}{2}\sum_{\alpha,\beta} Z_\alpha \int \frac{\varrho_\beta(\mathbf{r})}{r_\alpha}\,\mathrm{d}^3\mathbf{r} \\ &+ \frac{1}{2}\sum_{\alpha\geq\beta}\int \widetilde{V}_{\text{xc}}[\varrho_\alpha(\mathbf{r}),\varrho_\beta(\mathbf{r})]\,\mathrm{d}^3\mathbf{r} + \frac{1}{2}\sum_{\alpha\neq\beta}\frac{Z_\alpha Z_\beta}{R_{\alpha\beta}}. \end{aligned} \tag{3.18}$$

This leads to the simple expression for ground state energy:

$$E_{\text{tot}} = \sum_i \varepsilon_i n_i \; + \sum_{\alpha>\beta} U_{\text{rep}}(R_{\alpha\beta}). \tag{3.19}$$

The repulsive potential $U_{\text{rep}}$ is short ranged. Its value is derived from reference calculations (LDA or GGA) of dimers, small molecules or bulk systems for a range of typical bond lengths.

With the introduction of the repulsive potential not only the computational effort is reduced, but also methodological and numerical inaccuracies in calculation of the electronic contributions to the total energy are avoided.

## 3.5 The forces

The forces acting on the atoms are calculated from the derivation of the total energy with respect to the nuclear positions. In DFTB they are used within the representation of the repulsive potential (3.18). By considering the secular equations (3.2) the forces on atom $\alpha$ in the component $u = (x, y, z)$ can be written as:

$$F_u^{(\alpha)} = \sum_i n_i \sum_{\mu\nu} c_{\mu i} c_{\nu i} \left[ -\frac{\partial H_{\mu\nu}}{\partial (R_\alpha)_u} + \varepsilon_i \frac{\partial S_{\mu\nu}}{\partial (R_\alpha)_u} \right] + \sum_\beta \frac{\partial}{\partial (R_\alpha)_u} U_{\text{rep}}(R_{\alpha\beta}). \tag{3.20}$$

## 3.6 The self-consistent charge correction – SCC-DFTB

The approximations made in the DFTB method give fine results for polar and strong covalent systems. For heteroatomic systems with elements of quite similar electronegativities small energy differences have to be compared with each other. Therefore partial charge redistribution have to be taken into account. For this reason, *Elstner et al.* developed a self-consistent charge correction (SCC) [65] to allow the DFTB method a more accurate description of heteronuclear systems, especially large biomolecules.

In SCC-DFTB a second-order *Coulomb* correction term is introduced to the total energy expression of Eq. (3.4):

$$E_{\text{tot}} = \sum_i \varepsilon_i n_i \; + \; \frac{1}{2}\sum_{\alpha\beta} \Delta Q_\alpha \Delta Q_\beta \gamma_{\alpha\beta}(R_{\alpha\beta}) \; + \; U_{\text{rep}}(\alpha,\beta,R_{\alpha\beta}). \tag{3.21}$$

Therein, $Q_\alpha$ denotes charge centred at atom $\alpha$ (*Mulliken*) [95]);

$$\Delta Q_\alpha = Q_\alpha \; + \; Z_\alpha = \sum_i n_i \sum_{\mu\epsilon\alpha} \sum_\nu c_{\mu i} c_{\nu i} S_{\mu\nu} \; + \; Z_\alpha, \tag{3.22}$$

and $\gamma_{\alpha\beta}(R_{\alpha\beta})$ is a parameter related to the *chemical hardness* $\eta_\alpha$ [38] or the *Hubbard* parameter $U_\alpha$: $\gamma_{\alpha\alpha} \approx 2\eta_\alpha \approx U_\alpha$. Within DFT, this parameter is calculated as the second derivative of the total energy of the neutral atom with respect to the occupation number $n_{\text{HOMO}}$ of the highest occupied molecular orbital (HOMO):

$$U_\alpha = \frac{\partial^2 E_\alpha^0}{\partial n_{\text{HOMO}}^2} = \frac{\partial \varepsilon_{\text{HOMO}}}{\partial n_{\text{HOMO}}}. \tag{3.23}$$

The second order *Coulomb*-correction commits to the *Kohn-Sham* matrix elements directly:

$$H_{\mu\nu} = H_{\mu\nu}^{(0)} \; + \; \frac{1}{2} S_{\mu\nu} \sum_\gamma \Delta Q_\gamma \left( \gamma_{\alpha\gamma}(R_{\alpha\gamma}) + \gamma_{\beta\gamma}(R_{\beta\gamma}) \right). \tag{3.24}$$

However, this correction implies some disadvantages compared to the standard DFTB. In particular the self-consistency cycle increases the computation time considerably and numerous new parameters have to be introduced.

## 3.7 Practical realisation

In the non-self-consistent DFTB scheme, first, the pseudo atomic wavefunctions and the effective potential are calculated in the representation of STO's (2.23). Once these values are calculated, the integrals (3.4) and (3.3) are computed and tabulated as functions of the distance between the two atomic centres for an adequate dense grid of nodes. These tables are the so-called *Slater-Koster* tables [96]. Due to symmetry, only 10 integrals between basis functions remain non-zero for angular moments up to $l = 2$.

The set of repulsive potentials are represented numerically by a minimisation procedure that fits them into polynomials. This guarantees a smooth development of the dissociation curve:

$$U_{\text{rep}}(r) = \sum_n a_n (R_c - r)^n, \quad r < R_c, (r = R_{\alpha\beta}) \tag{3.25}$$

The powers are typically chosen $n \leq 8$. The cut-off radius $R_c$ represents the distance beyond the potential has subsidised, which is $1.5 - 2$ equilibrium bond lengths. Diatomic molecules are typically chosen as reference structures. For solid-state calculations, e. g., CdS, the crystal structure is used, too. Depending on the coordination numbers and different bond distances, several references can be used for fitting, e. g., for CdS the dimer, $(\text{CdS})_4$ and the crystal structure are chosen.

## 3.8 Calculation of optical properties within DFTB

### 3.8.1 The time-dependent density-functional response theory

Within the time-dependent density-functional linear response theory (TD-DFRT) the optical properties of finite systems are calculated using the coupling matrix. It gives the linear response of the SCF potential to a change in the electronic density. In the adiabatic approximation it has the following form:[97, 98]

$$K_{ij\sigma,kl\tau} = \iint \psi_i(\mathbf{r})\psi_j(\mathbf{r}) \left( \frac{1}{\mathbf{r}-\mathbf{r}'} + \frac{\partial^2 E_{\mathrm{xc}}}{\partial \varrho_\sigma(\mathbf{r}) \partial \varrho_\tau(\mathbf{r}')} \right) \psi_k(\mathbf{r}')\psi_l(\mathbf{r}') \, \mathrm{d}\mathbf{r}\mathrm{d}\mathbf{r}' \quad . \tag{3.26}$$

The excitation energies $\omega_I$ are obtained via solving the eigenvalue problem

$$\sum_{ij\sigma} \left[ \omega_{ij}^2 \delta_{ik}\delta_{jl}\delta_{\sigma\tau} + 2\sqrt{\omega_{ij}} K_{ij\sigma,kl\tau} \sqrt{\omega_{kl}} \right] F_{ij\sigma}^I = \omega_I^2 F_{kl\tau}^I \; ; \tag{3.27}$$

where $\omega_{ij} = \varepsilon_j - \varepsilon_i$ and $i, k$ denote the occupied, $j, l$ the unoccupied *Kohn-Sham* orbitals, which have to be calculated in advance.

The essentially manageable system size is mainly restricted by the dimension of the coupling matrix and the integral evaluation for each matrix element. For larger systems, the matrix size can be reduced similar to the complete active space method (CAS). Further reduction of the computational effort can be achieved by avoiding the integral evaluation in Eq. (3.26).

### 3.8.2 The $\gamma-$approximation

The so called $\gamma-$approximation gives a simplified calculation scheme for the coupling matrix (3.26) in TD-DFRT [67]. The functional derivative in the $V_{\mathrm{xc}}$ is rewritten using the set of variables: The total density $\varrho = \varrho_\uparrow + \varrho_\downarrow$ and the magnetisation $m = \varrho_\uparrow - \varrho_\downarrow$. For a spin-unpolarised ground state (closed-shell system) and no spin-orbit coupling, the functional derivative of the $V_{\mathrm{xc}}$ then results in

$$\frac{\partial^2 E_{\mathrm{xc}}}{\partial \varrho_\sigma(\mathbf{r}) \partial \varrho_\tau(\mathbf{r}')} = \frac{\partial^2 E_{\mathrm{xc}}}{\partial \varrho(\mathbf{r}) \partial \varrho(\mathbf{r}')} + (2\delta_{\sigma\tau} - 1) \frac{\partial^2 E_{\mathrm{xc}}}{\partial m(\mathbf{r}) \partial m(\mathbf{r}')} \quad . \tag{3.28}$$

As a second step, the transition density between different orbitals is decomposed into atomic contributions

$$p_{ij}(\mathbf{r}) = \psi_i(\mathbf{r})\psi_j(\mathbf{r}) = \sum_\alpha p_{ij\alpha}(\mathbf{r}), \tag{3.29}$$

which are further approximated by the monopolar term of a multipol expansion:

$$p_{ij\alpha}(\mathbf{r}) \approx q_{ij\alpha} F_\alpha(\mathbf{r}). \tag{3.30}$$

$F_\alpha(\mathbf{r})$ denotes a normalised spherical density fluctuation on atom $\alpha$ and the transition charges $q_{ij\alpha}$ are assigned by the *Mulliken* approximation:[95]

$$q_{ij\alpha} = \frac{1}{2}\sum_{\mu\in\alpha}\sum_{\nu}\left(c_{i\mu}c_{j\nu}S_{\mu\nu} + c_{i\nu}c_{j\mu}S_{\nu\mu}\right). \tag{3.31}$$

With Eq. (3.28) the approximated coupling matrices for singlet $K^S_{ij,kl}$ and triplet $K^T_{ij,kl}$ write as:

$$K^S_{ij,kl} = \sum_{\alpha\beta} q_{ij\alpha}q_{kl\beta}\widetilde{\gamma}_{\alpha\beta} \quad \text{and} \quad K^T_{ij,kl} = \sum_{\alpha\beta} q_{ij\alpha}q_{kl\beta}\widetilde{m}_{\alpha\beta}, \tag{3.32}$$

with the remaining two functionals:

$$\widetilde{\gamma}_{\alpha\beta} = \iint' \frac{1}{\mathbf{r}-\mathbf{r}'} + \frac{\partial^2 E_{\mathrm{xc}}}{\partial\varrho(\mathbf{r})\partial\varrho(\mathbf{r}')}\bigg|_{\varrho} F_\alpha(\mathbf{r})F_\beta(\mathbf{r}')\,\mathrm{d}\mathbf{r}\mathrm{d}\mathbf{r}' \tag{3.33}$$

$$\widetilde{m}_{\alpha\beta} = \iint' \frac{\partial^2 E_{\mathrm{xc}}}{\partial m(\mathbf{r})\partial m(\mathbf{r}')}\bigg|_{\varrho} F_\alpha(\mathbf{r})F_\beta(\mathbf{r}')\,\mathrm{d}\mathbf{r}\mathrm{d}\mathbf{r}' \tag{3.34}$$

that have to be estimated: $\widetilde{\gamma}_{\alpha\beta}$ can be taken exactly as the *Hubbard* parameter $\gamma_{\alpha\beta}$ introduced in SCC-DFTB. Because the term of $\widetilde{m}_{\alpha\beta}$ is short-ranged too, it is also considered as one-centre contribution $\widetilde{m}_{\alpha\beta} = \delta_{\alpha\beta}M_\alpha$ with:

$$M_\alpha = \frac{1}{2}\left(\frac{\partial\varepsilon^{HOMO}_{\uparrow}}{\partial n_{\uparrow}} - \frac{\partial\varepsilon^{HOMO}_{\uparrow}}{\partial n_{\downarrow}}\right). \tag{3.35}$$

Using Equation (3.32) for the construction of the coupling matrix and solving the secular equation (3.27), one determines the excitation energies and the oscillator strengths $f^I$ is determined by:

$$f^I = \frac{2}{3}\sum_{k=x,y,z}\left|\sum_{ij}\sum_{\alpha}\mathbf{R}_\alpha q_{ij\alpha}\sqrt{\frac{\omega_{ij}}{\omega_I}}\left(F^I_{ij\uparrow} + F^I_{ij\downarrow}\right)\right|^2. \tag{3.36}$$

Instead of an explicit integration of the transition-dipole matrix elements the *Mulliken* approximation is chosen:

$$\left\langle \psi_i \,\middle|\, \mathbf{r}_k \,\middle|\, \psi_j \right\rangle = \sum_{\alpha}\mathbf{R}_\alpha q_{ij\alpha}, \tag{3.37}$$

with $\mathbf{R}_\alpha$ being the position vector of atom $\alpha$.

### 3.8.3 Quality of the $\gamma-$approximation

The quality of the electronic excitation spectra is depends on the quality of the DFTB parameterisation. Especially the description of the unoccupied levels is influenced by the charge density representation, from which the atomic potentials are generated, e. g., in the standard DFTB method or the systematically improved SCF-DFTB (cf. Chapter 4).

So far, $\gamma-$approximation has been successfully applied for the calculation of small organic molecules.[67] The singlet states have been reproduced in remarkable agreement with the

experiment. Similarly to the values obtained by *first-principle* calculations values with a minimal basis set, the one-particle energy differences $\omega_{KS}$ are over-estimated. The main reason for this agreement can be attributed to the contraction of the density by the additive harmonic potential contribution $V_{\text{add}}$ (cf. Section 3.3).

A second reason is the monopole approximation and the resulting screened interactions. Here the coupling correction ($\gamma-$approximation) results in smaller excitation energies than TD-DFRT, with the full interaction (3.26). Thus, through the only small deviations between the *Kohn-Sham* orbitals from DFTB and coupling correction relative to *ab initio* results with expanded basis sets, the agreement of the singlet excitation energies according to the experiment arises. Whereas the TD-DFRT results are in general smaller than the experimental values.

For the same reason, the triplet states are less accurate described. Since they have only small contributions to the optical spectra and are not calculated in this work explicitly, these deviations are not discussed in further detail.

# 4 Systematic improvement of the DFTB method

One objective of this work is the calculation of optical properties of CdS nanoparticles. This requires an accurate description of occupied and unoccupied bands closest to the *Fermi* level. However in DFTB and SCC-DFTB the description of unoccupied bands the results are inaccurate, especially for heteroatomic systems (cf. Section5.1). These inaccuracies may be addressed to the minimum basis sets and to the DFTB approximations in general. Nonetheless, for hetero-atomic systems these inaccuracies can be addressed to an inaccurate charge-transfer (CT) description, which constitutes the non-self-consistent treatment of the effective potential (cf. Section 3.2).

Solving this problem, herein a new parameter-free self-consistent-field DFTB (SCF-DFTB) is formulated. Therefore, it includes the electron redistribution the overlap region of the atoms by recoupling the electronic density to atomic potentials. Hence, SCF-DFTB represents a systematic improvement of the standard DFTB method towards the full DFT scheme, which provides further arguments for the validation of the DFTB approximations.

## 4.1 Charge-transfer within the DFTB approximations

Within the DFTB approximations the full screening of the nuclei (neglecting the pseudo potential contributions (3.8)) and charge neutrality (neglecting the crystal field/three-centre contributions (3.9)) are assumed for the electronic system. In analogy, it may be related to the cellular *Wigner-Seitz* methods representation (System constructed of neutral atoms)[91, 92]. Additionally, DFTB includes two-centre interactions for the bonding region (overlap region) by neutral pseudo atoms.

In the standard DFTB scheme the effective potential (3.2), and thus, the electronic wavefunctions are not recoupled to the electronic density. For heteroatomic systems it has inaccuracies in the description of the inter-atomic charge redistribution. Thus, especially the unoccupied states/bands are wrongly described.

As a first attempt to this a second-order *Coulomb* correction (SCC-DFTB) was introduced. It handles the CT with a monopole expansion of the atom centred charges (cf. Chapter 3 and references therein). The charge-density rebalance of the SCC-DFTB scheme mainly effect a shifting of the orbital/band energies (onsite shift). Beside the time consuming computation of such very long ranged lattice sums, the model of atom centred charges represented as monopoles or multipoles also leads to an inappropriate physical picture. Since

the charge-redistribution in such a scheme is incorporated in real-space, and, not in the orbital-space of the molecular system (overlap region).

The idea is to incorporate charge-density redistribution (in the orbital space) in the DFTB scheme, such the effective potential (cf. Section 3.2) is treated in a self-consistent way, similar to the full-DFT scheme. This self-consistency allows the change of the shape of the atomic potentials, which affects mainly the bonding region in between the atoms. This new self-consistent-field DFTB (SCF-DFTB) method will be introduced in the following sections. The first application and test calculation follow in Chapter 5.

## 4.2 The Kohn-Sham-equations in SCF-DFTB

In the same way as in the standard DFTB method, the *Kohn-Sham* single-particle wave-function $\psi_i$ in SCF-DFTB are expressed within the LCAO approach (3.1). This allows the transformation of the *Kohn-Sham* equations into the secular problem:

$$\sum_{\nu} c_{\nu i} \left( \widetilde{H}_{\mu\nu} - \varepsilon_i \, \widetilde{S}_{\mu\nu} \right) = 0 \qquad \text{with} \quad \begin{aligned} \widetilde{S}_{\mu\nu} &= \left\langle \, \phi_\mu \, \middle| \, \phi_\nu \, \right\rangle \\ \widetilde{H}_{\mu\nu} &= \left\langle \, \phi_\mu \, \middle| \, \hat{T} + \widetilde{V}_{\text{eff}}(\mathbf{r}) \, \middle| \, \phi_\nu \, \right\rangle . \end{aligned} \tag{4.1}$$

Herein, the *Kohn-Sham* matrix is build up using a **self-consistent** effective potential $\widetilde{V}_{\text{eff}}(\mathbf{r})$, which is constructed by the superposition of potentials of pseudo ions. In analogy to the full DFT scheme, but in contrast to standard DFTB, the solution of the *Kohn-Sham* equations in the form of the secular problem (4.1) is carried out iteratively, within using the SCF technique. Therefore, the molecular orbitals $\psi(\mathbf{r})$ within the standard DFTB scheme can be used as initial guess for the density $\varrho(\mathbf{r})'$, from which the first effective potential $\widetilde{V}_{\text{eff}}(\mathbf{r})$ is constructed.

## 4.3 The self-consistent effective Potential

In analogy to the standard DFTB scheme [cf. Eq. (3.6)], the *self-consistent* effective potential $\widetilde{V}_{\text{eff}}$ is represented by atom-like effective potentials. In SCF-DFTB these are *self-consistent* effective potentials of **pseudo ions** $\widetilde{V}_{\text{eff}}^{(\alpha)}(\mathbf{r})$:

$$\widetilde{V}_{\text{eff}}(\mathbf{r}) = \sum_{\alpha}^{N_K} \widetilde{V}_{\text{eff}}^{(\alpha)}(\mathbf{r}) + \frac{q_\alpha}{\mathbf{r}} \tag{4.2}$$

$$\widetilde{V}_{\text{eff}}^{(\alpha)}(\mathbf{r}) = \sum_{l=1}^{\infty} \sum_{m=-l}^{l} \widetilde{V}_{lm}^{(\alpha)}(r_\alpha) \, Y_{lm} \left( \frac{\mathbf{r}_\alpha}{r_\alpha} \right)^n , \qquad \text{with } \mathbf{r}_\alpha = \mathbf{r} - \mathbf{R}_\alpha \, . \tag{4.3}$$

By the same reasons discussed in section 3.3, also the effective potentials of the pseudo ions $\widetilde{V}_{\text{eff}}^{(\alpha)}(\mathbf{r})$ will be compressed by an additional additive harmonic contribution $V_{\text{add}}$.

The *Kohn-Sham* matrix elements read now:

$$\widetilde{H}_{\mu\nu} = \left\langle \phi_\mu \,\middle|\, -\frac{1}{2}\nabla^2 + \widetilde{V}_{\text{eff}}^{(\alpha)}(\mathbf{r}) + \frac{q_\alpha}{\mathbf{r}} + \sum_{\beta\neq\alpha}^{N_K} \widetilde{V}_{\text{eff}}^{(\beta)}(\mathbf{r}) + \sum_{\beta\neq\alpha}^{N_K} \frac{q_\beta}{\mathbf{r}} \,\middle|\, \phi_\nu \right\rangle \ , \tag{4.4}$$

including the conservation of the charge neutrality.

$$\sum_{\alpha=1}^{N} q_\alpha = 0 \ . \tag{4.5}$$

The introduction of $\frac{q}{\mathbf{r}}$ appears somewhat unfavourable for the description of the charge balance in-between the nuclei, but is due to technical reasons. The exact determination of those charges $q$ is given in Section 4.4.

By applying the DFTB approximations (3.8 and 3.9), the expression for the *Kohn-Sham* matrix elements reads similar to Eq. (3.10):

$$\widetilde{H}_{\mu\nu} = \begin{cases} \left\langle \mu \,\middle|\, -\frac{1}{2}\nabla^2 + \widetilde{V}_{\text{eff}}^{(\alpha)}(\mathbf{r}) + \frac{q_\alpha}{\mathbf{r}} + \widetilde{V}_{\text{eff}}^{(\beta)}(\mathbf{r}) + \frac{q_\beta}{\mathbf{r}} \,\middle|\, \nu \right\rangle \ , & \mu \in \{\alpha\}, \nu \in \{\beta\} \\ \left\langle \mu \,\middle|\, -\frac{1}{2}\nabla^2 + V_{\text{eff}}^{(\alpha)}(\mathbf{r}) \,\middle|\, \nu \right\rangle \ , & \mu, \nu \in \{\alpha\}. \end{cases} \tag{4.6}$$

Furthermore, the introduced compression of the effective potential changes single particle energies. Also in SCF-DFTB the approach of *Porezag et al.* is applied to obtain the correct dissociation limits [61]:

$$\widetilde{H}_{\mu\nu} = \begin{cases} \left\langle \mu \,\middle|\, -\frac{1}{2}\nabla^2 + \widetilde{V}_{\text{eff}}^{(\alpha)}(\mathbf{r}) + \frac{q^{(\alpha)}}{\mathbf{r}} + \widetilde{V}_{\text{eff}}^{(\beta)}(\mathbf{r}) + \frac{q^{(\beta)}}{\mathbf{r}} \,\middle|\, \nu \right\rangle \ , & \begin{array}{l} \mu \in \{\alpha\}, \\ \nu \in \{\beta\}, \\ \alpha \neq \beta \end{array} \\ \varepsilon_\mu^{0,\text{free}} \ , & \mu = \nu \\ 0 \ , & \text{otherwise.} \end{cases} \tag{4.7}$$

The onsite contributions $V_{\text{eff}}^{(\alpha)}(\mathbf{r})$ are represented by potentials of free and neutral atom. The charge-density redistributions in the electronic system are, thus, **only** considered in the two-centre interactions.

This scheme represents an alternative of the cellular method by *Wigner* and *Seitz*.[91, 92] The poly-atomic electronic systems are described to consist mainly of atoms. Variations of electron density in-between those atoms due to chemical binding are covered to a great extend by two-centre contributions.

## 4.4 Realisation of the SCF within SCF-DFTB

The above given description for the iterative solution of the *Kohn-Sham* equations (4.1) can be chosen in analogy to that, which is applied in the full-DFT scheme. In this work the

density of the system is not used directly to propagate the effective potential (4.2). Instead a projection of it to atomic contributions is applied.

Thus, in each iteration step the new effective potential is obtained by using the atomic charges $q_\alpha$ in the investigated system following Eq. (4.14), as well as the atomic orbital population $N_\mu^\alpha$ (4.12), which specify the electronic occupation numbers of pseudo atom/ion (4.3).

The total number of electrons $N$ in the system result from the spatial integration of the single-particle charge density $\varrho(\mathbf{r})$:

$$N = \int \varrho(\mathbf{r})\, \mathrm{d}^3\mathbf{r}\ , \quad \text{with the Ansatz:} \quad \varrho(\mathbf{r}) = \sum_i^{occ} n_i \mid \phi_i \mid^2 , \tag{4.8}$$

which can be transformed to:

$$N = \sum_i^{occ} n_i \sum_{\mu\nu} c_\mu^i c_\nu^i \left\langle \phi_\mu \mid \phi_\nu \right\rangle , \tag{4.9}$$

$$= \sum_\alpha \sum_{\mu\in\alpha} n_\mu + \sum_{\alpha\neq\beta} \sum_{\substack{\mu\in\alpha \\ \nu\in\beta}} D_{\mu\nu} S_{\mu\nu} , \qquad \text{with} \quad \begin{array}{lcl} n_\mu & \equiv & \sum_i n_i {c_\mu^i}^2, \\ D_{\mu\nu} & \equiv & \sum_i n_i c_\mu^i c_\nu^i, \\ S_{\mu\nu} & \equiv & \left\langle \phi_\mu \mid \phi_\nu \right\rangle . \end{array} \tag{4.10}$$

In Eq. (4.10) $n_\mu$ is the orbital net population, the $D_{\mu\nu}$ the density matrix elements and $S_{\mu\nu}$ the overlap integral. Using the LCAO approach and a minimum basis set (valence only), the representation of the atomic-orbital densities can be uniquely defined by *Mulliken* populations.[95] Following *Mulliken*, the overlap population between two centres,

$$n(\alpha,\beta) = 2 \sum_{\substack{\mu\in\alpha \\ \nu\in\beta}} D_{\mu\nu} S_{\mu\nu} , \tag{4.11}$$

is divided up equally on both sites. Thus, the so-called gross population $N_\alpha$ at atom $\alpha$ reads

$$N_\alpha = \sum_{\mu\in\alpha} N_\mu^\alpha = \sum_{\mu\in\alpha} n_\mu^\alpha + \sum_{\beta\neq\alpha} \sum_{\mu\in\beta} D_{\mu\nu} S_{\mu\nu}. \tag{4.12}$$

With the nuclear charge $Z_\alpha$ at centre $\alpha$, the gross charge $q_\alpha$ is defined as

$$q_\alpha = Z_\alpha - N_\alpha \tag{4.13}$$

In case of using a valence basis set, the core electrons $N_\alpha^{\mathrm{core}}$ have to be added to the $N_\alpha$ valence electrons resulting in

$$q_\alpha = Z_\alpha - (N_\alpha + N_\alpha^{\mathrm{core}}) \ . \tag{4.14}$$

In conclusion, with this approach the CT in the electronic system is controlled by the atomic charges $q_\alpha$. These charges can be related to the ionicity of the atoms. In SCF-DFTB the regarded CT will be more pronounced with an increasing differences of the electronegativities of the atoms.

A drawback of the self-consistent treatment of the effective potential $V_{\text{eff}}$ is the increase of the computational effort. For SCF-DFTB it is in the order of magnitude of full DFT schemes. A first application of the new method follows in the next Chapter 5. There also an approximate realisation of the SCF will be introduced, which provides the efficiency of the standard DFTB method. Nonetheless, SCF-DFTB can be applied as single-point calculation using the structure that has been obtained with standard DFTB.

## 4.5 SCC-SCF-DFTB

SCF-DFTB incorporates charge-transfer effects in the two-centre interactions, while the onsite energies are taken from the free neutral atoms [cf. Eq. (4.7]. Therefore, the SCC correction scheme is applied for SCF-DFTB.

The SCC iterations are carried out on the converged SCF-DFTB effective potential 4.3 : The *Coulomb* correction to the *Kohn-Sham* matrix elements reads

$$\widetilde{H}_{\mu\nu} = \widetilde{H}^{(0)}_{\mu\nu} \; + \; \frac{1}{2}\widetilde{S}_{\mu\nu} \sum_{\gamma} \Delta Q_{\gamma} \left( \boldsymbol{\gamma}_{\alpha\gamma}(R_{\alpha\gamma}) + \boldsymbol{\gamma}_{\beta\gamma}(R_{\beta\gamma}) \right) . \tag{4.15}$$

Here the same atomic parameters $\boldsymbol{\gamma}$ are used as for the SCC-DFTB. The $Q_{\alpha}$ represent the atom centred charges (*Mulliken*) obtained with SCF-DFTB:

$$\Delta Q_{\alpha} = Q_{\alpha} \; + \; Z_{\alpha} = \sum_{i} n_i \sum_{\mu \epsilon \alpha} \sum_{\nu} c_{\mu i} c_{\nu i} \widetilde{S}_{\mu\nu} \; + \; Z_{\alpha} \tag{4.16}$$

# 5 Electronic structure calculation with SCF-DFTB

Improving the charge-transfer description in the context of the DFTB approximations the SCF-DFTB method has been introduced in Chapter 4. This Chapter is addressed to tests on the accuracy of this new scheme for CdS compounds, as well as, further heteroatomic systems. At first, the insufficiency of the standard DFTB schemes in the description of the unoccupied states will be highlighted. Subsequently, the details of the computation for SCF-DFTB, as well as, for full SCF-DFT reference are given.

## 5.1 Electronic structure of CdS within standard DFTB

The electronic band structure of zinc blende CdS calculated with the standard DFTB method is depicted in Figure 5.1 It is compared to the corresponding result obtained with full SCF-DFT. The details of these calculations are given in the next Section 5.2. The obtained bandstructures are very good agreement for the occupied bands. In contrast, the unoccupied bands are shifted to higher energies. Using DFTB with the valence basis set Cd $4d5s5p$ and S $3s3p$, a band gap ($\Gamma$-point) of approximately 5.0 eV at the $\Gamma-$point is obtained. This is twice as large compared to the experimental value of 2.58 eV [11].

However, the full-DFT reference calculation results a too small band gap energy, which is approximately half of the experimental one. This deviation can be addressed to the applied LDA.

Moreover, it has to be tested, if the deviations in the description of the unoccupied bands with DFTB are due to an insufficient basis set. Hence, the valence basis set of atomic functions is expanded by additional polarisation functions. The recalculated DFTB band structure is shown in the upper right column of Figure 5.1: The additional S $3d$ functions cause a shift of the unoccupied bands to lower energies. At the $\Gamma$-point these bands are shifted from 10 eV to 5.5 eV. The conduction band, which consists of mainly Cd $5s$, becomes localised. The band gap energy remains unchanged compared to the calculation with the smaller basis set.

Since, CdS represents a hetero-atomic system, for which in case of the DFTB method density redistributions should be considered within the SCC-DFTB correction. The calculated SCC-DFTB band structure of zinc blende CdS is depicted in the lower panels of Figure 5.1: The bands are corrected with a small shift of the band energy toward the DFT reference bandstructure. According to the discussion in Section 4.1, SCC-DFTB only the

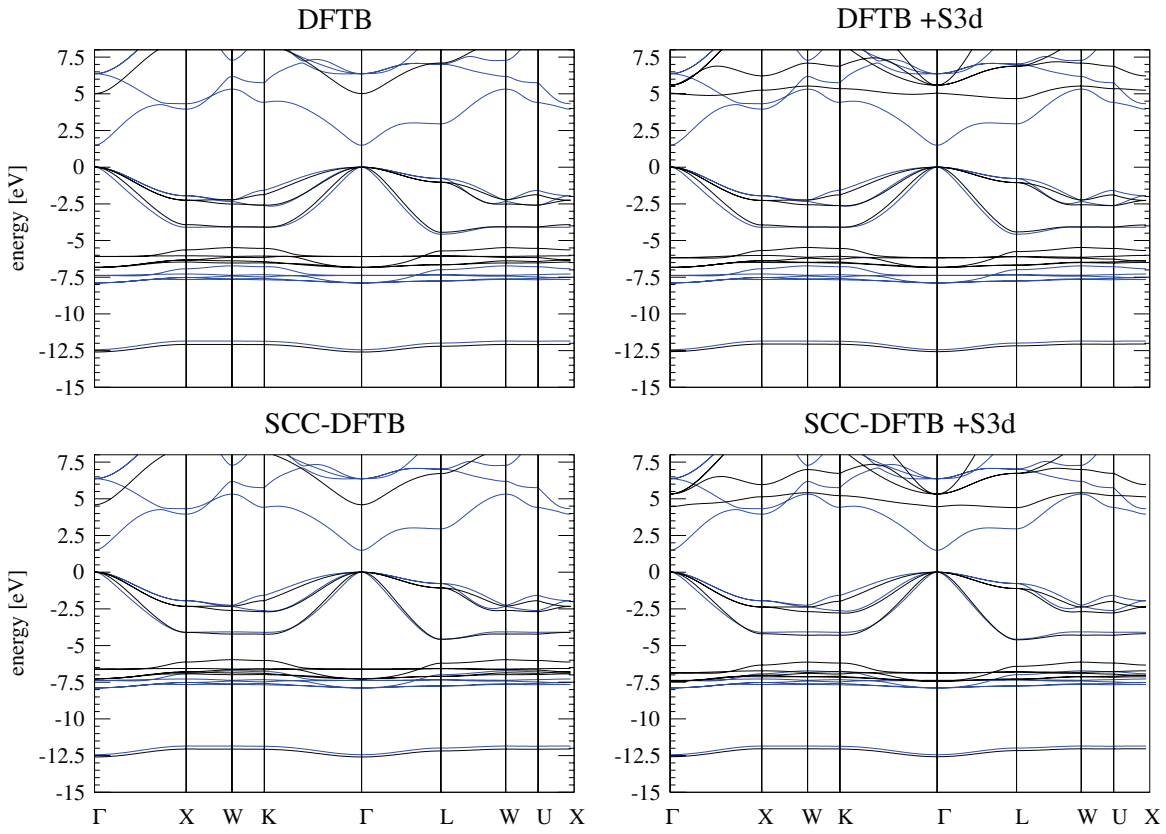


Figure 5.1: *Bandstructure of zinc blende CdS calculated with standard DFTB (upper panels, black curves) and SCC-DFTB (lower panels, black curves). The panels in the left column denote to DFTB calculation with a Cd* $4d5s5p$*, S* $3s3p$ *valence basis, whereas that in the right column include additional the S* $3d$ *functions. The reference bandstructure is calculated with SCF-DFT. For better depiction the valance band edge is shifted to* $0eV$*. Further details of the calculations are given in Sect. 5.2.*

band energies by an onsite shift. However, SCC-DFTB is not able to deviations for the unoccupied bands remain basically unchanged for the smaller and the extended basis set.

## 5.2 Details of the calculation

### 5.2.1 DFT reference calculation

The reference calculations are performed with the full potential local orbital LCAO band-structure code* [99]. This calculation scheme solves the *Kohn-Sham* equations self-consistently. In the effective potential $V_{\text{eff}}$ all tree-centre, as well as the crystal field contributions are included. These are neglected in the DFTB approximations. An additional harmonic potential $V_{\text{add}}$ is used for contraction of the long-ranging contributions of the atomic potential [93, 59]. The advantage of using the FPLO code as the reference is, that it provides the same atomic basis representation (local orbitals), as it is applied within DFTB in this work.

The details of the computationally details of FPLO are chosen to correspond with those of the DFTB computation: For the exchange-correlation potential the parameterisation following *v. Barth* and *Hedin* is chosen [100], the exponent of the $V_{\text{add}}$ is taken to $n = 2$, as well as, the semi-relativistic corrections are applied herein. In contrast, the values of the contraction radii $r_0$ of $V_{\text{add}}$ are fixed values within the DFTB method, whereas in FPLO they are optimised. Thus, the optimal values are calculated in each step of the SCF for each valence function with a different angular momentum $l$, exclusively. The atomic levels at lower energies are treated within a frozen core approximation, which finally corresponds to the following configuration of the atomic basis set:

| atom type | core function | valence function |
|---|---|---|
| Cd : | $1s2s2p3s3p3d4s4p$ | $4d5s5p$ |
| S : | $1s2s2p$ | $3s3p3d$ |

For the further computational details, e. g., numeric integration meshes, the the default values of FPLO program are used.

### 5.2.2 Details on SCF-DFTB calculation – parameter generation

The new SCF-DFTB scheme is tested with a calculation of the electronic structure of the bulk polymorphs of CdS. The obtained atomic charges $q_\alpha$ Eq. (4.14) $q_\alpha$ Eq. (4.14) and angular-momentum resolved orbital populations $N_l^\alpha$ (4.12) are summarised in Table 5.1 for zinc blende, wurtzite and rock salt. The given reference values have been obtained from a full SCF-DFT calculation using the FPLO code.

*The version 5.00-18 of the FPLO-code is used (also see www.fplo.de)

Table 5.1: *Calculated atomic valence orbital populations $N_l^\alpha$ and atomic charges $q_\alpha$ for the CdS bulk modifications zinc blende, wurtzite and rock salt using SCF-DFTB. The reference values are obtained from SCF-DFT. Further details of the computation are given in Section 5.2.*

| structure[a] | atom | *Mulliken*-population $N_l^\alpha$ and atomic charges $q_\alpha$: [b] | | | | | | | |
|---|---|---|---|---|---|---|---|---|---|
| | | DFT[c] | | | | SCF-DFTB | | | |
| | | $q_\alpha$ | s | p | d | $q_\alpha$ | s | p | d |
| zinc blende | Cd | 0.62 | 0.74 | 0.74 | 9.90 | 0.60 | 0.71 | 0.92 | 9.77 |
| | S | -0.62 | 1.83 | 4.66 | 0.13 | -0.60 | 1.86 | 4.53 | 0.21 |
| wurtzite | Cd | 0.67 | 0.73 | 0.70 | 9.90 | 0.52 | 0.71 | 1.11 | 9.66 |
| | S | -0.67 | 1.84 | 4.68 | 0.13 | -0.52 | 1.79 | 4.42 | 0.31 |
| rock salt | Cd | 0.77 | 0.68 | 0.64 | 9.91 | 0.71 | 0.71 | 0.71 | 9.87 |
| | S | -0.77 | 1.87 | 4.72 | 0.18 | -0.71 | 1.95 | 4.62 | 0.14 |

[a] The experimental values for the unit cell parameters structures are used (cf. Table 6.2.2).

[b] For Cd the $l = s, p, d$ denote to the $5s, 5p$, $4d$, whereas for S to the $3s, 3p$, $3d$ functions.

[c] using the FPLO code [99]. Details are given in Section 5.2.1.

Comparing the values of SCF-DFTB and the reference calculation values a relatively good agreement is found for the atomic charges $q_\alpha$. These are slightly underestimated for zinc blende, approximately 8% for rock salt and approximately 25% for wurtzite. These different deviations are mainly due to the used two centre approximation in DFTB and the distinct structures. While the wurtzite structure exhibit a relatively large barelanoid-like cavity and the zinc blende a smaller adamantine-like cavity, whereas the rock salt structure has the smallest one. Thus, the values of the orbital populations $N_l^\alpha$ change within SCF-DFTB compared to the reference: The electrons are shifted from the more localised S $3p$ and Cd $4d$ functions toward the diffuse S $3d$ and Cd $5p$ functions. This effect is also observed for the zinc blende structure, but less pronounced, whereas the values of the rock salt structure corresponds much better to the DFT results.

However, the self-consistent solution of the *Kohn-Sham* equations increases the computational effort drastically. The gain compared to the full DFT calculation is in the order of a factor of 2 compared to the FPLO calculation. The bandstructure calculations on bulk CdS structures included a maximum of four atoms which is still valuable, but, becomes impossible for structures with some thousand of atoms, e. g., nanoparticles.

Reducing the computational effort, further approximations have to be made, in particular to avoid the integral evaluation: It have been shown, that the electronic structure of CdS bulk and that of the nanoparticles are rather similar to each other [101, 102, 103, 104].

Hence, in SCF-DFTB the two-centre integrals are also very similar and can be calculated in advance for a reference system, e. g., CdS bulk. Finally, they are stored in *Slater-Koster* tables and used to calculate distinct CdS structures.

However, in this approximate SCF-DFTB scheme the transferability towards structural changes may not be given, since the parameters only represent the electronic structure of the reference system. Nonetheless, it has been shown that for different structures, i. e., zinc blende, wurtzite and rock salt CdS, the values of the atomic charges $q_\alpha$ and occupation numbers of the atomic orbitals $N_l^\alpha$ are rather similar (cf. Table 5.1). Furthermore, with this approximate SCF-DFTB scheme electronic band structure calculations are carried out to verify the transferability of the *Slater-Koster* tables: At first the integral tables are generated for the three structures zinc blende, wurtzite and rock salt using SCF-DFTB. Subsequently, with each of parameter table the band structures of zinc blende, wurtzite and rock salt CdS are calculated. For each structure three very similar band structures are obtained. E. g., the band structures of wurtzite calculated with the zinc blende *Slater-Koster* tables and that using the wurtzite tables are resemble each other. This transferability allows using only one integral table set for all three structural modifications of CdS.

In this work, this approximate variant of SCF-DFTB will be applied for the investigations of the electronic structure of CdS nanoparticles. The corresponding *Slater-Koster* tables are obtained from the bulk CdS zinc blende structure.

## 5.3 Test calculations on CdS compounds with SCF-DFTB

In this Section the electronic structures of CdS bulk and CdS molecule are calculated with DFTB and SCF-DFTB and compared to the reference results obtained by full SCF-DFT calculations.

In Figure 5.2 the band structures of CdS bulk CdS (zinc blende modification) are contrasted: The standard DFTB method, the new SCF-DFTB and as reference the SCF-DFT. With the SCF-DFTB method the bands is in overall agreement to the full potential SCF-DFT reference. The conduction band is reproduced at with its characteristic dispersion at the $\Gamma-$point and exhibit a direct band gap. Minor deviations compared to the DFT reference, result at the lower symmetry points. However, these deviations are due to the DFTB approximations, since they are present in the occupied bands for SCF-DFTB, as well as, for standard DFTB.

Further correction is obtained by applying additionally the SCC scheme in SCF-DFTB. Clear from the lower panels in Figure 5.2, the relative band energies the valence as well as the conduction bands fit to the reference DFT result.

Moreover, with the same accuracy the band structure of the wurtzite CdS bulk is obtained with SCF-DFTB and SCC-SCF-DFTB (cf. Figure B.1).

The values of the band gap energy are underestimated by all calculation schemes. This

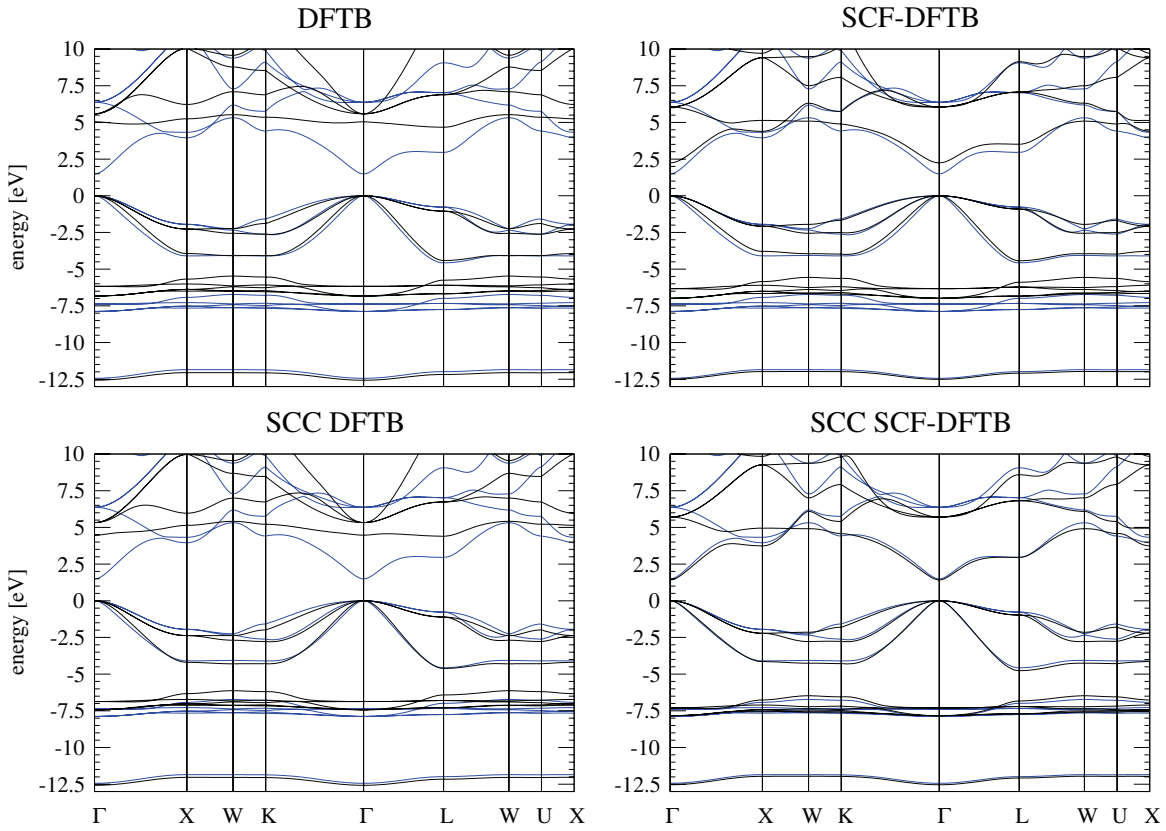


Figure 5.2: *Calculated bandstructures of zinc blende CdS calculated using DFTB (left panels), SCF-DFTB (right panels) and the results which include the SCC-correction (lower panels). The reference bandstructure is represented by a SCF-FPLO calculation (blue curves). Further details of the calculations are given in Section 5.2.*

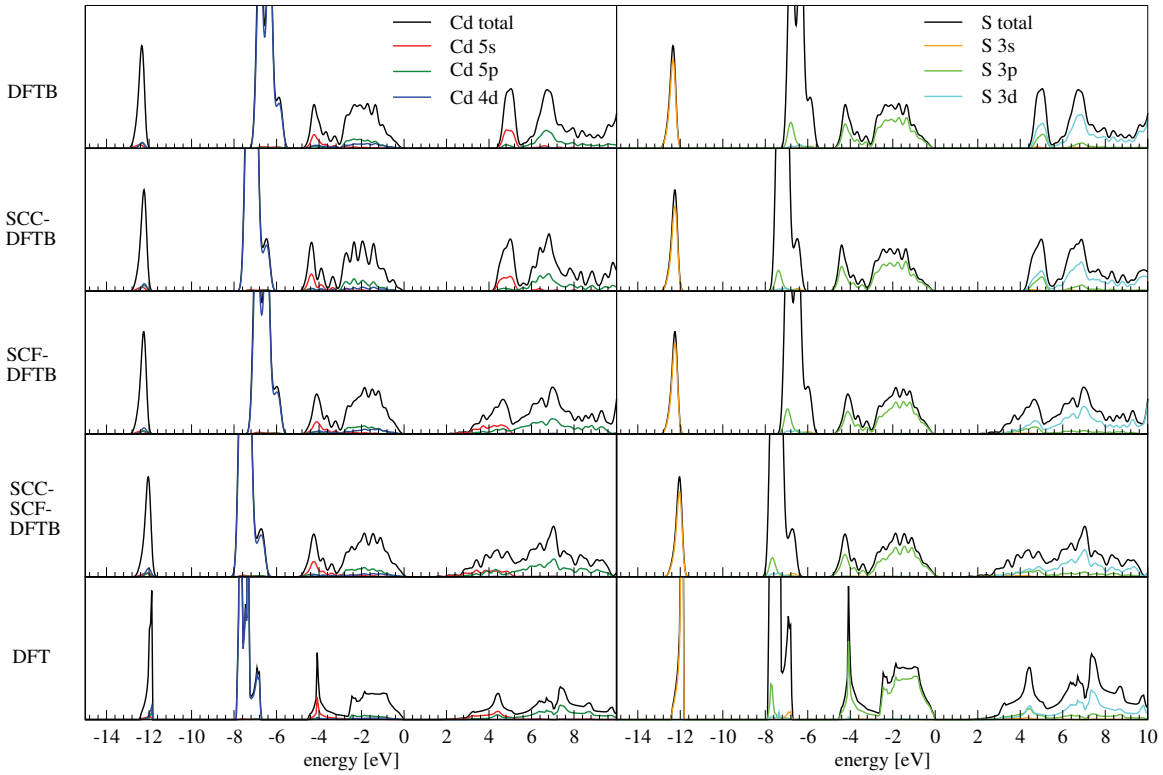


Figure 5.3: *Calculated electronic DOS of zinc blende CdS bulk corresponding to the band-structures in Figure 5.2. Additionally the projected DOS (p-DOS) to the atomic functions of Cd (left column) and S (right column) is depicted. The valence band edge is shifted to* 0 *eV. Further details of the calculations are given in section 5.2.*

is due to the overbinding effect of the used LDA. Nonetheless, the band gap energy as well as the states closest to the *Fermi* are obtained systematically improved with SCF-DFTB compared to standard DFT. Hence, the inaccuracies of the standard DFTB scheme are not due to the DFTB approximations in general. In contrast these are validated by the present results.

Furthermore, the corresponding electronic DOS are plotted for the zinc blende structure in Figure 5.3 and wurtzite in Figure B.2. In agreement to the previous investigations [105, 106, 107, 108, 109, 110], both electronic DOS profiles are found to be very similar to each other: Including the projection to the atomic contributions (pDOS), The valence bands consist of three separate bands: two occupies with contributions of mainly S $3s$ functions at $-12$ eV and the Cd $4d$ at $-7.5$ eV. These are localised and have a high DOS, whereas the third broads over 5 $eV$ with the main contributions from S $3p$ and minor ones from Cd $5s5p$ at the lower energy edge. At the valence band edge the states originate from S $3p$ functions. The conduction band starts above at a band gap of approximately 2 eV with a low electronic DOS, which is similar to the free electron behaviour. The pDOS assigns this to consist mainly of the Cd $5s$ function. At higher energies the bands have again a higher DOS, that originate from Cd $5p$ and S $3d$ functions.

The comparison of these electronic DOS and the DFT references results shows no noteworthy differences and likewise the pDOS are in agreement. Minor discrepancies in the electronic DOS curves between the SCF-DFTB (DFTB) calculation and the DFT results are of technical reasons, since different broadening schemes for the electronic states have been applied. Furthermore, the usage of the SCC correction in combination with DFTB, as well as, SCF-DFTB effectuates an onsite shift of the band energy, which mainly affect the Cd $4d$ states.

In conclusion, this reference calculation of the electronic structure of CdS bulk structures corroborates, that a correct charge-transfer description is archived by the new SCF-DFTB scheme. The values of the band gap energy are underestimated by all applied calculation schemes, which is due to the used LDA. Nonetheless, the band gap energy as well as the states closest to the *Fermi* are obtained systematically improved with SCF-DFTB compared to standard DFT. Hence, the inaccuracies of the standard DFTB scheme are not due to the DFTB approximations in general. In contrast, these are validated by the present results.

# 6 From bulk to finite structures in the nano regime

This chapter is addressed to the structural properties CdS nanoparticles and in particular to the influence of surface. In this size regime it has a major impact on the physical and chemical properties of the particle. Experimental and theoretical investigations found that the nanoparticles behaviour is mainly governed by the properties of the extended crystal structure. The core structure of CdS nanoparticles is found to resemble the corresponding bulk, while the surface atoms are found partially or completely saturated (e. g., see in Ref.[2]) Only for small cluster the exact position of these ligands has been determined (cf. Appendix A). For the larger ones it can only be guessed.

Therefore, in the following a surface saturation scheme is developed. It is able to describe different structures that are bare, partially and completely saturated surfaces as well as the distinct shapes of nanoparticles. After testing the capability of the standard DFTB method in the accurate description of the CdS structures, This scheme is applied to generate several series of bare and saturated structures. Finally, the structural properties and stability of these structures are studied.

## 6.1 Modelling structures of CdS nanoparticles

### 6.1.1 The bulk CdS and surface structures

Two modifications of CdS are known that are stable under ambient conditions – namely Hawleyite (zinc blende structure, colourised diamond) and Greenockite (hexagonal wurtzite, colourised lonsdaleite) [111]. A third is crystallising in the rock salt structure, which is observed under high pressure (above $2.5 - 3.5$ GPa) [112]. Both polymorphs – zinc blende and wurtzite – are found energetically degenerated, while experimental evidences indicate the latter one being slightly more stable [11]. Both comprise a tetrapodal building block in which each atom of one sort is surrounded by four of the other one. In terms of Bravais lattices, the zinc blende crystal structure is a face-centred cubic (fcc) lattice with a diatomic basis. This basis can be taken as one corner atom plus the centre of the cubic building block. The wurtzite structure has hexagonal symmetry with typically a four-atomic basis.

Following common rules of chemistry for covalently bound compounds, e. g., valence rules, structural build-up and electronic structure of CdS can be understood to a large extent. There are some variants and generalisations of these rules in use, i. e., the *Grimm-*

*Sommerfeld* rule or the so-called *Mooser-Pearson* relation. The *Grimm-Sommerfeld* rule describes the structural similarity:

> A binary compound of elements of group $N - k$ and group $N + k$ owe the same properties of the group $N$ of the periodic system of elements (PSE).*

The *Mooser-Pearson* relation in contrast is based on an ionic approach and suited for semiconductor compounds:

$$\frac{N_e + B^{(a)} - B^{(c)}}{N_a} = 8$$

with

| | |
|---|---|
| $N_e$ | number of valence electrons per formula unit, |
| $B^{(a)}$ | number of electrons in anion-anion bonds, |
| $B^{(c)}$ | number of electrons in cation-cation bonds or, free electrons at the cation, |
| $N_a$ | number of anions. |

Binary *Grimm-Sommerfeld* compounds, such as II-VI semiconductor systems with tetrahedral networks (i. e., zinc blende or wurtzite type), are representing a special case herein:

$$\begin{aligned} N_e &= 2 + 6 = 8 \\ B^{(a)} &= B^{(c)} = 0 \\ N_a &= 1 \\ \frac{8 + 0 - 0}{1} &= 8. \end{aligned}$$

In this simple model, the metal atoms (electron donator) provide two electrons to the chalcogenide atoms (electron acceptor), which result "stable" closed-shell configurations, e. g., $Cd^{2+}$ ([Kr]$d^{10}$-configuration) and $S^{2-}$ ([Ar]-configuration). In the tetrahedral coordination sphere this results in a "charge-transfer" of 0.5 electrons per bond from Cd to S. Considering the electronic structure in bulk of CdS, this is mirrored in a large band gap (2.58 eV) [11], which arises due to the complete filling of the $S$ $3p$ like states (shell closing). The two $5s$ electrons per Cd atom first fill up this $S$ $3p$-like state (two unoccupied orbitals per atom) to form the bonds with mainly covalent character in a tetrahedral coordination. A further discussion of the structure-electronic structure interplay in CdS nanoparticles follows in Chapter 7.

*Eg., zinc blende (ZnS) as generalisation of the element structure of carbon (diamond structure) or GeSe as variant of the grey phosphorus.

Table 6.1: *Some geometric properties of spherical, cuboctahedral and tetrahedral nanoparticles.*

| property [a] | tetrahedron[b] | cuboctahedron[b] | sphere |
|---|---|---|---|
| A | $\sqrt{3}a^2$ | $\left(6+2\sqrt{3}\right)a^2$ | $4\pi r^2$ |
| V | $\frac{1}{12}\sqrt{2}a^3$ | $\frac{5}{3}\sqrt{2}a^3$ | $\frac{4}{3}\pi r^3$ |
| $r_S$ | $\frac{1}{4}\sqrt{6}a$ | $a$ | $r$ |
| $\frac{V}{V_S}$ | $\frac{2}{3\pi}\sqrt{2}\approx 0.3$ | $\frac{5}{4\pi}\sqrt{2}\approx 0.56$ | 1 |
| $\frac{V}{A}$ | $\frac{1}{9}r_S\approx 0.11r_S$ | $\frac{\frac{5}{3}\sqrt{2}}{6+2\sqrt{3}}r_S\approx 0.25r_S$ | $\frac{1}{3}r$ |

[a] $A$ denotes the surface, $V$ the volume, $r$ the radius and the index $S$ the circumscribed sphere of the polyhedron with the radius $r_S$.

[b] The variable $a$ is the edge length of the corresponding polyhedron.

### 6.1.2 Modelling bare CdS nanoparticles

Experimentally determined structures of CdS nanoparticles were found to resemble the bulk CdS structure, even for the smallest CdS nanoparticles [113, 114, 115, 116, 117, 118, 119, 120]. All of these structures have protecting ligands on their surface. Their "core" (inner) structure is following that of the CdS bulk, which is experimentally evidenced for the structures of larger nanoparticles. In appendix A a systematic overview of the characterised series of CdS cluster structures is given.

Following this experimental results, the structures were modelled such, that they represent a part from the infinite periodic crystal, i. e., with either a zinc blende or wurtzite structure. These studies investigate CdS and CdSe clusters and nanoparticles using empirical tight-binding models [121, 122, 101, 123, 124, 125], whereas a parameter-free density-functional method was used for small CdSe clusters by *Eichkorn* and *Ahlrichs* [126], *Troparevsky* and *Chelikowsky* [127], and *Galli et al.* [128]. Within standard DFTB, these were carried out for a variety of II-VI semiconductor systems [129, 102, 130, 131, 78]. Recently, *Kasuya et al.* suggested, that other structures than that of the bulk polymorphs may also be relevant, for example cage-like structures that have been found for boron nitride [132].

### Shape

For these small particles, the number of surface atoms is significant compared to those in the core of the particle, so that their contribution to the energetic and the electronic properties is crucial. So that, a minimisation of the surface energy dominates the structural build up.

However, in case of the smallest nanoparticles, which are mostly found with a tetrahedral shape (cf. Appendix A). This is due to local the geometry of the surface, viz. the tetrahedral coordination, allowing an ideal faceting (for zinc blende only (111)-faces). Hence, the larger surface to volume ratio compared to the sphere is compensated. The spherical geometry will become favourable for very large structures, when the portion of the surface energies becomes negligible. However, for structures in-between, the cuboctahedral shape is a compromise. It possesses both – an ordered surface and a relatively low surface to volume ratio (cf. Table 6.1).

Considering the **spherical shape** for CdS nanoparticles' structures, (cf. i. e., Refs. [133, 16]) and starting from the bulk zinc blende or wurtzite structures, essentially, two types of structures can be derived:

- **stoichiometric** [$(CdS)_n$], when the centre of the spherical cluster is the midpoint of a Cd–S nearest-neighbour bond [102], in the centre of adamantine (zinc blende structure) or barelanoid (wurtzite structure) like cavities, and
- **non-stoichiometric** [$Cd_mS_n$], with $n \neq m$, when the centre is on an atom position [102].

Size series of **cuboctahedral shaped** structures can be obtained for the zinc blende as well as for the wurtzite structure. They are obtained, when starting from the smallest building block – the tetrahedral $CdS_4$ or respectively $SCd_4$ cluster. Then continuing with the crystal structure shells of Cd–S (S–Cd) atoms are added (cf. Appendix A). The resulting particles are **non-stoichiometric** with the surface atoms being exclusively of one type depending on the number of added atom shells.

Based on the zinc blende only, **tetrahedral shaped** nanoparticles are observed experimentally, while none seem to exhibit the wurtzite structure exclusively. This type of shape is derived similar as the cuboctahedral one and also starting from the tetrahedral building block. The structure is continued only in one, i. e., (111), crystallographic direction of the corresponding zinc blende bulk structure. Also this structure series are of **non-stoichiometric** composition.

With a further modification on the vertices of these tetrahedral structures, one obtains slightly different, but tetrahedral nanoparticles with a mixed zinc blende-wurtzite structure (cf. Appendix A and Figure 6.1).

#### Electronic structure of the surface

For a single unsaturated particle, due to the finite surface structure, the electronic structure balance of the bulk is locally disturbed and, thus, the stable electron octet configuration can not be reached for either type of the atom (cf. Section 6.1.1). It is not satisfied for nanoparticles with a stoichiometric composition $[(CdS)_n]$.

The possible surface defects, which arise through the modelling via "cutting" the infinite bulk structure, are summarised in Table 6.2). The therein used nomenclature is the following: $(\cdots S)_3 \equiv Cd$ denotes a surface Cd atom, which miss one S with respect to the bulk (one dangling bond). The nearest neighbour (NN) atoms in the core of the nanoparticles are written in the brackets. They are fourfold coordinated and their environment corresponds to the bulk. Such, $(\cdots S)_2 = Cd$ misses two S and $(\cdots S)_1 - Cd$ three S respectively. Additionally, a number for the deficit of electrons to the stable octet configuration is defined: For surface-located S atom $N_{e_S}$ have negative numbers (missing electrons) and positive $N_{e_{Cd}}$ for Cd atoms, which excess electrons (charge).

An example which demonstrates the disturbed charge balance of the particles is given in the upper part of Table 6.4. Therein, the electronic structures of the surface of nanoparticles with stoichiometric composition $[(CdS)_n]$ and spherical shape are analysed. These structures not only owe an equal number of atoms of both type in total, but also equal numbers of surface atoms, as well as, their type of coordination and dangling bonds respectively. Such an alternation of local positive and negative surface charges is not observed in experimental observations, rather than a saturation of these reactive centres.

However, for gas-phase structures, which are found to be non-saturated, reconstruction of the surface atoms can be an alternative for stabilising the surface structure [132]. Nonetheless, the nanoparticles are generally synthesised in the solution in which defects (dangling bonds) as reactive centres are easily find a counterpart reactant for stabilisation.

### 6.1.3 Modelling surface-saturated CdS nanoparticles[†]

Due to the size scale of the nanoparticles, the properties of the surface determine mainly that of the whole particle. The particles are synthesised mostly in solutions of *Lewis*-base type organic solvents, leading to cadmium chalcogenide nanoparticles saturated with tri-octyl phosphine/tri-octyl phosphine oxide (TOP/TOPO) [16, 103], polyphosphate [134], or thiol groups [116, 117, 135, 136, 118, 119, 120]. During the growth process these in most cases surfactants are essential for the electronic stabilisation of the nanoparticles surfaces. Nonetheless, this bonding must be reversible to some extent to allow further growth [137, 16]. A stable surface is needed to stop the growth process (ligand exchange) and, further, avoid phenomena such as dissolution and photodegradation [138]. While an incomplete coverage

[†]In more general this is valid for all type II-VI semiconductors of AB-stoichiometry.

Table 6.2: *Possible surface defects and their electron balance for II–VI semiconductors with zinc blende or wurtzite structure (herein represented by CdS). The given saturation scheme takes into consideration, that all metal atoms (Cd) are in a bulk-like environment, viz. tetrahedral coordinated by the chalcogenide atoms (S).*

| | coordination of the surface atom[a] | | |
|---|---|---|---|
| | threefold | twofold | single |
| defect | $(\cdots S)_3 \equiv Cd$ | $(\cdots S)_2 = Cd$ | $(\cdots S)_1 - Cd$ |
| No. dangling bonds at Cd | 1 | 2 | 3 |
| VE ($-0.5e^-$ per bond) | $3 \cdot -0.5 + 2 = \mathbf{0.5}$ | $2 \cdot -0.5 + 2 = \mathbf{1.0}$ | $1 \cdot -0.5 + 2 = \mathbf{1.5}$ |
| octet deficit[b] $N_{e_{Cd}}$ | 0.5 | 1 | 1.5 |
| defect | $(\cdots Cd)_3 \equiv S$ | $(\cdots Cd)_2 = S$ | $(\cdots Cd)_1 - S$ |
| No. dangling bonds at S | 1 | 2 | 3 |
| VE ($+0.5e^-$ per bond) | $3 \cdot 0.5 + 6 = \mathbf{7.5}$ | $2 \cdot 0.5 + 6 = \mathbf{7.0}$ | $1 \cdot 0.5 + 6 = \mathbf{6.5}$ |
| octet deficit $N_{e_S}$ | -0.5 | -1 | -1.5 |
| saturation | $(\cdots Cd)_3 \equiv S - R$ | $(\cdots Cd)_2 = S - R$ | $(\cdots Cd)_1 - S - R$ |
| VE ($+1e^-$per R) | $3 \cdot 0.5 + 6 + 1 = \mathbf{8.5}$ | $2 \cdot 0.5 + 6 + 1 = \mathbf{8.0}$ | $1 \cdot 0.5 + 6 + 1 = \mathbf{7.5}$ |
| octet deficit[b] $N_{e_S}$ | 0.5 | 0 | -0.5 |

[a] With respect to the non-saturated surface atom.

[b] A positive value denotes to an electron excess to the corresponding stable octet configuration.

(missing surfactants) causes surface-trapped states in the luminescence spectra [125, 103, 139, 140].

When comparing the experimental determined structures of the small nanoparticles (cf. appendix A), all Cd atoms are found fourfold coordinated by S atoms, which is verified for the larger particles by extended x-ray-absorption fine structure (EXAFS) and *Fourier*-transform infrared (FTIR) spectroscopy [140]. Furthermore, in this study most of the surface chalcogenide atoms were characterised having non-saturated (dangling) bonds.

Surfactant molecules have been treated in previous studies by theoretical models, e. g., within DFT [126], tight-binding [125, 124], semi-empirical [141] or classical force field approaches [142]. However, for those nanoparticle structures the surfactants' positions were known from experiment (small nanoparticles) or added by geometrical considerations. A systematic investigation, and especially a theoretical foundation of the nanoparticle surface saturation over a larger size range, which includes the electronic structure balance, is lacking.

Therefore in the following, a structure saturation scheme is introduced, which combines experimental results and chemical valence-bond theory (cf. Section 6.1.1).

### Complete saturation scheme

In this scheme, according to the experimentally characterised structures, all Cd atoms are considered to be full fourfold coordinated as in the bulk. In terms of valence-bond theory, this can be understood, since the electron donator Cd owes dangling bond(s). These are reactive centres, which attract electron acceptors. Accordingly, the surface S atom's coordination, the number of its valence electrons, and thus its deficit to the stable octet, was already discussed above. For a surface S atom the tetrahedral coordination results three different environments (cf. Table 6.2).

By saturating the dangling bonds, by substituting the surface covering S atoms by a sulphur-containing surfactants, e. g., S−R with R = organic residue (thiol or thiophenol), the chemical nature of sulphur being just twofold coordinated is exploited. However, not in all cases the local electron deficit of the surface S atom $N_{e_S}$ can be compensated completely (cf. lower part in Table 6.2): Only for $(\cdots\mathrm{Cd})_2{=}\mathrm{S}{-}\mathrm{R}$ the surface S atom reaches the stable octet ($N_{e_S} = 0$). In contrast, with $N_{e_S} = -0.5$, electrons are missing for $(\cdots\mathrm{Cd})_1{-}\mathrm{S}{-}\mathrm{R}$, while $(\cdots\mathrm{Cd})_3{\equiv}\mathrm{S}{-}\mathrm{R}$ has an electron excess of $N_{e_S} = 0.5$ with respect to the octet rule.

Additionally, also the non-saturated $(\cdots\mathrm{Cd})_3{\equiv}\mathrm{S}$ should be taken into consideration for the surface termination, since it has a comparable deficit $N_{e_S} = -0.5$, too. It is furthermore present in the experimentally determined crystal structure of the $[\mathrm{Cd}_{32}\mathrm{S}_{14}(\mathrm{SR})_{36}]^0$ compound. It owes four of such non-saturated surface atoms [120, 118]. Concerning larger nanoparticle structures these may correspond to those identified by *Carter et al.* [140].

In short, the used **saturation scheme** for II–VI semiconductor nanoparticles with zinc blende or wurtzite structure reads the following:[‡]

1. Full tetrahedral coordination of all Cd-atoms, with respect to the bulk structure (zinc blende and wurtzite).

2. Saturation at the four distinct surface positions:

$$(\cdots\mathrm{Cd})_3{\equiv}\mathrm{S}, \quad (\cdots\mathrm{Cd})_3{\equiv}\mathrm{S}{-}\mathrm{R}, \quad (\cdots\mathrm{Cd})_2{=}\mathrm{S}{-}\mathrm{R}, \quad (\cdots\mathrm{Cd})_1{-}\mathrm{S}{-}\mathrm{R}.$$

After applying this saturation scheme the nanoparticles are of composition:

$$[\mathrm{Cd_mS_n(SH)_i}]^{\mathrm{q}}, \text{ with } \mathrm{q}{=}2(\mathrm{m}{-}\mathrm{n}){-}\mathrm{i}$$

with q representing the charge of the nanoparticles, which is obtained by summing up the deficit (excess) valence electrons at the surface S-atoms. This additional charge q is needed to stabilise the nanoparticles electronically, it guarantees the complete filling of the valence states (S 3*p*). Otherwise, if the structures has more or less electrons, the electronic properties

[‡]In analogy, for the rock salt structure the scheme has to be extended, that it satisfy the charge balance for an octahedral coordination.

are changed, since an almost zero HOMO-LUMO gap would result. However, this charge can easily be compensated in solution by the counter ions.

Furthermore, for clusters (nanoparticles), stability is often discussed in relation to the existence of a significant large band gap between valance and conduction band. In terms of molecular orbital theory, the gap between the highest occupied and lowest unoccupied molecular orbitals (the HOMO-LUMO gap) [143]. Moreover, the existence of magic numbers, i. e., of particularly stable clusters, is associated to the occurrence of those gaps [144, 145]. When discussing the stability of II–VI semiconductor nanoparticles, one finds interplay between structural and electronic effects.

### Examples and implementation of the structure generation and saturation algorithm

With Table 6.3 as a first example the saturation scheme is tested on small, experimental characterised CdS nanoparticles.[§] For all compounds, the above introduced saturation scheme describes their surface structure correctly.

For these small compounds the generation of the structures is feasible by "hand" or using common molecular structure editors (`molden`, `molekel`, etc.). Thus, for efficiency the introduced structure generation and saturation algorithms are implemented in a computer code: On the basis of a certain bulk structure, spherical, cuboctahedral or tetrahedral nanoparticles are generated. This is realised by cutting them out from an extended structure of thee corresponding unit cell, which serves as input for the program. New structures are found by increasing the cutting-radius. Optionally, these bare nanoparticles can be saturated following the saturation scheme.

A second example for the saturation scheme, which is given in the lower part of Table 6.4, is generated using this tool. In this example stoichiometric, spherical nanoparticles with the composition $[(CdS)_n]$ have been saturated. After this saturation the values of q are relatively small ($q = 6, \ldots, 18$). This is due to the complete saturation of the surface. In contrast, much higher charges q would result form the a saturation which includes the non-passivated $(\cdots Cd)_3 \equiv S$ instead of $(\cdots Cd)_3 \equiv S-R$.

In the following investigations of the structural, electronic and optical, size dependent properties of type II-VI semiconductor nanoparticles the structures are modelled respectively to the above given schemes. Whereas the saturated are based on bare structures. As follows, the threefold coordinated, but in one bond unsaturated $(\cdots Cd)_3 \equiv S$ is not included. Furthermore, the surfactant residue R is approximated by H atoms.

[§]These structures are further used as reference for the investigations in the following.

Table 6.3: *Validation of the saturation scheme for II-VI semiconductor nanoparticles structures: Experimentally characterised, small CdS clusters and nanoparticles compounds following* $[Cd_mS_n(SH)_i]^q$ *with* $q=2(m-n)-i$ *representing the charge of the nanoparticles. Their corresponding structures are depicted in Figure 6.1.*

| $[Cd_mS_n(SH)_i]^q$ | Lit. | $N_{\equiv S}$ | $N_{-S-R}$ | $N_{=S-R}$ | $N_{\equiv S-R}$ | $\sum N_{e_S}$ |
|---|---|---|---|---|---|---|
| | $N_{e_S}$ | –0.5 | –0.5 | 0.0 | 0.5 | |
| $[Cd(SR)_4]^{2-}$ | [146] | 0 | 4 | 0 | 0 | -2 |
| $[Cd_4(SR)_{10}]^{2-}$ | [147, 146] | 0 | 4 | 6 | 0 | -2 |
| $[Cd_4S(SR)_{10}]^{4-}$ | [24] | 1 | 7 | 3 | 0 | -4 |
| $[Cd_4S(SR)_{12}]^{6-}$ | [122] | 0 | 12 | 0 | 0 | -6 |
| $[Cd_8S(SR)_{16}]^{2-}$ | [148] | 0 | 4 | 12 | 0 | -2 |
| $[Cd_{10}S_4(SR)_{16}]^{4-}$ | [113, 114, 146] | 4 | 4 | 12 | 0 | -4 |
| $[Cd_{13}S_4(SR)_{24}]^{6-}$ | [122] | 0 | 12 | 12 | 0 | -6 |
| $[Cd_{17}S_4(SR)_{28}]^{2-}$ | [119] | 0 | 4 | 24 | 0 | -2 |
| $[Cd_{20}S_{13}(SR)_{22}]^{8-}$ | [149] | 12 | 4 | 18 | 0 | -8 |
| $[Cd_{28}S_{13}(SR)_{42}]^{12-}$ | [122] | 0 | 24 | 18 | -0 | -12 |
| $[Cd_{32}S_{14}(SR)_{36}]^{0}$ | [120, 118] [a] | 0 | 4 | 36 | 0 | -2 |
| $[Cd_{32}S_{14}(SR)_{40}]^{4-}$ | [b] | 4 | 4 | 36 | 0 | -4 |
| $[Cd_{35}S_{28}(SR)_{28}]^{14-}$ | [149] | 24 | 4 | 24 | 0 | -14 |
| $[Cd_{54}S_{32}(SR)_{48}]^{4-}$ | [a] | 12 | 0 | 48 | 0 | -6 |
| $[Cd_{54}S_{32}(SR)_{52}]^{8-}$ | [b] | 12 | 4 | 48 | 0 | -8 |
| $[Cd_{55}S_{28}(SR)_{64}]^{10-}$ | [122] | 0 | 24 | 36 | 4 | -10 |
| $[Cd_{92}S_{55}(SR)_{92}]^{18-}$ | [122] | 0 | 40 | 48 | 4 | -18 |

[a] These structures are missing the ligands at the four edges ($(\cdots S)_3 \equiv Cd$), additionally $2e^-$ (0.5 each) have to be considered in the total charge balance.

[b] These structures are modelled by adding the four additional ligands each to the edges of the experimental structures $[Cd_{32}S_{14}(SR)_{36}]^0$ and $[Cd_{54}S_{32}(SR)_{48}]^{4-}$.

Table 6.4: *[Surface structure of bare (upper part) and saturated (lower part) II-VI semiconductor nanoparticles structures (CdS). Their shape is spherical and the crystal structure is zinc blende. The centre of the particle in on a Cd–S nearest neighbour bond which result a stoichiometric composition* $(CdS)_m$*. After saturation, these structures have the composition* $[Cd_mS_n(SH)_i]^q$*, with* $q=2(m-n)-i$ *representing the charge of the nanoparticles.*

| $(CdS)_m$ | $N_{-S}$ | $N_{=S}$ | $N_{\equiv S}$ | $N_{S_{bulk}}$ | |
|---|---|---|---|---|---|
| | $N_{e_S}=-1.5$ | –1.0 | –0.5 | 0.0 | $\sum N_{e_S}$ |
| | $N_{-Cd}$ | $N_{=Cd}$ | $N_{\equiv Cd}$ | $N_{Cd_{bulk}}$ | |
| | $N_{e_{Cd}}=1.5$ | 1.0 | 0.5 | 0.0 | $-\sum N_{e_{Cd}}$ |
| $(CdS)_{16}$ | 3 | 3 | 6 | 4 | -10.5 |
| $(CdS)_{28}$ | 6 | 3 | 9 | 10 | -16.5 |
| $(CdS)_{37}$ | 3 | 12 | 6 | 16 | -19.5 |
| $(CdS)_{43}$ | 0 | 12 | 15 | 16 | -19.5 |
| $(CdS)_{68}$ | 3 | 15 | 16 | 34 | -27.5 |
| $(CdS)_{95}$ | 9 | 12 | 22 | 52 | -36.5 |
| $(CdS)_{104}$ | 6 | 21 | 19 | 58 | -39.5 |
| $(CdS)_{119}$ | 0 | 27 | 25 | 67 | -39.5 |
| $(CdS)_{132}$ | 4 | 18 | 39 | 71 | -43.5 |
| $(CdS)_{144}$ | 1 | 24 | 36 | 83 | -43.5 |
| $(CdS)_{180}$ | 0 | 30 | 39 | 111 | -49.5 |
| $(CdS)_{306}$ | 3 | 39 | 60 | 204 | -73.5 |
| $[Cd_mS_n(SH)_i]^q$ | $N_{\equiv S}$ | $N_{-S-R}$ | $N_{=S-R}$ | $N_{\equiv S-R}$ | |
| | $N_{e_S}=-0.5$ | –0.5 | 0.0 | 0.5 | $\sum N_{e_S}$ |
| $[Cd_{16}\,S_4\,(SH)_{30}\,]^{-6}$ | 0 | 18 | 6 | 6 | -6 |
| $[Cd_{26}\,S_8\,(SH)_{46}\,]^{-10}$ | 0 | 31 | 4 | 11 | -10 |
| $[Cd_{37}\,S_{16}\,(SH)_{54}\,]^{-12}$ | 0 | 30 | 18 | 6 | -2 |
| $[Cd_{43}\,S_{16}\,(SH)_{60}\,]^{-6}$ | 0 | 27 | 18 | 15 | -6 |
| $[Cd_{68}\,S_{34}\,(SH)_{77}\,]^{-9}$ | 0 | 34 | 27 | 16 | -9 |
| $[Cd_{95}\,S_{52}\,(SH)_{104}]^{-18}$ | 0 | 61 | 18 | 25 | -18 |
| $[Cd_{104}S_{58}\,(SH)_{107}]^{-15}$ | 0 | 49 | 39 | 19 | -15 |
| $[Cd_{119}S_{67}\,(SH)_{119}]^{-15}$ | 0 | 55 | 39 | 25 | -15 |
| $[Cd_{132}S_{71}\,(SH)_{130}]^{-14}$ | 0 | 55 | 36 | 39 | -14 |
| $[Cd_{144}S_{83}\,(SH)_{136}]^{-14}$ | 0 | 64 | 36 | 36 | -14 |
| $[Cd_{180}S_{111}(SH)_{153}]^{-15}$ | 0 | 69 | 45 | 39 | -15 |
| $[Cd_{306}S_{204}(SH)_{222}]^{-18}$ | 0 | 96 | 66 | 60 | -18 |

## 6.2 Reference calculations on CdS bulk and molecular structures

For the test of the DFTB method both size extremes of CdS structures small molecules (clusters) and the bulk polymorph of CdS are chosen. Especially the structures of the small clusters have been intensively studied experimentally (cf. previous sections and references therein). Not only for the larger nanoparticles, but even for the very small ones the structure is found almost identical to that of the bulk CdS.

At first, the CdS bulk and, secondly, the small clusters' structural properties are investigated with standard DFTB method (cf. Section 3). Therein, geometry optimisations are performed on the structures and compared to the results of other methods reported in the literature. Beside DFTB, these include empirical potentials (force fields), semi-empirical methods, HF and DFT formalisms.

### 6.2.1 Generation of the (standard) DFTB parameters

For the investigation of CdS nanoparticles with the DFTB method, the *Slater-Koster* tables have to be generated (cf. Section 3.7). According to the recent investigations of *Joswig et al.* [102, 150], a similar parameterisation for the Cd and S integral calculations are chosen, which consider also semi-relativistic corrections. The repulsive potential (3.18), in addition to the small (diatomic) molecules used by *Joswig et al.*, is including the fit for the bulk CdS zinc blende structure. Further, *Slater-Koster* tables for the ligand-nanoparticle interactions are calculated in analogy.

Therein the *Slater-Koster* tables where generated including the following atomic functions in the minimum basis sets:

| element | $r_0$[a.u.] | valence functions |
|---|---|---|
| Cd : | 5.6 | $4d5s5p$ |
| S : | 3.9 | $3s3p$ |
| O : | 2.7 | $2s2p$ |
| C : | 2.7 | $2s2p$ |
| H : | 1.3 | $1s$ |

with $r_0$ being the compression radius for atomic functions (cf. section 3.3).

### 6.2.2 Bulk CdS structures

The calculations of CdS bulk – zinc blende, wurtzite and rock salt– are summarised in Table 6.2.2. For zinc blende and rock salt, the primitive unit cell representation, which includes two atoms per cell, is chosen, preliminary to provide consistency for the comparison of standard DFTB and the DFT reference[¶]. In all cases the number of **K** points for sampling

[¶]The full-potential local-orbital (FPLO) LCAO-DFT formalism is used (cf. Section 5.2.1).

Table 6.5: *Reference values of the CdS bulk polymorph structures by standard DFTB calculation: Lattice constants, bond lengths r, and relative total energies in comparison to other theoretical and experimental values.*

| structure | parameter | DFTB | DFT[a] | exp.[b] | theory[c] |
|---|---|---|---|---|---|
| wurtzite | $a$ [pm] | 409.7 | 412.3 | 412.5 | 412.1 |
| | $c$ [pm] | 670.4 | 674.6 | 674.9 | 668.2 |
| | $r_{\mathrm{wz}}$(Cd−S) [pm] | 251.0 | 252.5 | 252.7 | 252.2 |
| zinc blende | $a$ [pm] | 579.0 | 583.0 | 581.8 | 581.1 |
| | $r_{\mathrm{wz}}$(Cd−S) [pm] | 250.7 | 252.4 | 251.9 | 251.6 |
| rock salt | $a$ [pm] | 552.0 | 548.0 | 530.2 | |
| | $r_{\mathrm{rs}}$(Cd−S) [pm] | 276.0 | 274.0 | 265.1 | |
| | $\Delta E_{\mathrm{wz-zb}}/N_{\mathrm{atom}}$[d] [eV] | 0.0033 | | | -0.0011 |
| | $\Delta E_{\mathrm{rs-zb}}/N_{\mathrm{atom}}$[d] [eV] | 0.885 | | | |

[a] Using the FPLO code [99]. Details are given in Section 5.2.1.

[b] Ref. [11] for zinc blende and wurtzite, Ref. [112] for rock salt.

[c] Refs. [151, 107].

[d] $\Delta E_{x-\mathrm{zb}}$ has a positive value, if zinc blende is more stable than wurtzite or rock salt ($x = \{\mathrm{wz}, \mathrm{rs}\}$).

the *Brillouin* zone are chosen such that the total energy is converged to a threshold of $10^{-6} a.u.$.

Subsequently, the equilibrium lattice constants are obtained by varying the lattice parameters. The results are in good agreement with the other theoretical values and compared to the experimental ones. In particular the bond lengths differ by less than 1 %. Only for the rock salt structure, the bond lengths $r_{rs}$ in DFTB (and DFT) are about 3 % larger than the experimental value [112]. It has to be noted, that despite using only the zinc blende structure fitting the repulsive potential in DFTB the bond length compared result in an astonishingly good.

Furthermore, the calculation reproduces the near-degeneracy of the two crystal structures – zinc blende and wurtzite– within 3.3meV the zinc blende phase being more stable. Experimental investigations [11] show indications for the opposite: A slightly more stable wurtzite polymorph. But, up to now no relative total energies are available. Moreover, the high pressure rock salt structure results in a local energy minimum, which is almost 1eV above the zinc blende structure.

In comparison to *Joswig et al.* [102], the additional consideration of the bulk structure in the repulsive potential for the Cd–S interaction does not improve the results for the bulk CdS structures remarkably, but it allows the accurate description of the rock salt structure, too.

### 6.2.3 Small CdS cluster and nanoparticle structures

A second test of the DFTB parameters comprises the calculation of the structural properties of small nanoparticles, from which the structures have been determined in experiments. The complete set of these structures is summarised in Table 6.3, which contains also the literature references. We have added two structures to this set: The tetrahedral shaped $[Cd_{32}S_{14}(SR)_{40}]^{4-}$ and $[Cd_{54}S_{32}(SR)_{52}]^{8-}$. They are derived from $[Cd_{32}S_{14}(SR)_{36}]^{0}$ and $[Cd_{54}S_{32}(SR)_{48}]^{4-}$, which miss one ligand molecule at each of the four vertices of the structure. A systematic classification of structures of small CdS nanoparticles is given in Appendix A.

The experimental geometries are used as a starting point for the geometry relaxation. This is performed using the standard DFTB method. The structures are optimised below a maximal gradient of $10^{-4}$ Ha/Bohr within single MD simulations.[‖]

In the calculated initial structures the original (experimental used) surfactants are approximated with hydrogen atoms. Their final optimised geometries are qualitatively reproduced with these DFTB parameters (cf. Figure 6.1). Quantitatively, the Cd–S bond distances and angles in the centre of the nanoparticle are in agreement with the experiment. Thus they are significantly less, but also close to the experimental values for the corresponding bulk structures (cf. Table 6.2.2). While those of the atoms at the cluster surface are slightly smaller (1-2%) compared to the experimental values. This is not due to the approximated surfactants (R=H). Since the explicit consideration of larger and experimentally used ligand molecules $[Cd_{17}S_4(SR)_{28}]^{2-}$ and $[Cd_{32}S_{14}(SR)_{40}]^{4-}$) with (R=$CH_2CH_2OH$, R=$Ph(C_6H_5)$ in the DFTB simulation did not cause significant changes in the Cd–S bond lengths at the particles surface and, thus, validates the H-approximation.

## 6.3 Structural properties of CdS nanoparticles

Up to here, the structure generation and saturation scheme for the CdS nanoparticles' was introduced, implemented and successfully tested using the DFTB method. On this basis, in the following the structural properties of CdS nanoparticles up to approximately 1000 atoms are investigated. First, bare (non-saturated) structures are studied, subsequently that of completely saturated ones. Finally, the effects of an incomplete saturation, i. e., defects or dangling bonds, on the structural properties are investigated by a successive saturation of the surface.

### 6.3.1 Bare nanoparticles

In recent investigations spherical, bare (non-saturated) II–VI semiconductor nanoparticles and their structural properties were investigated with the standard DFTB method [129,

[‖]The computational details of this MD simulations are described in detail in the following section.

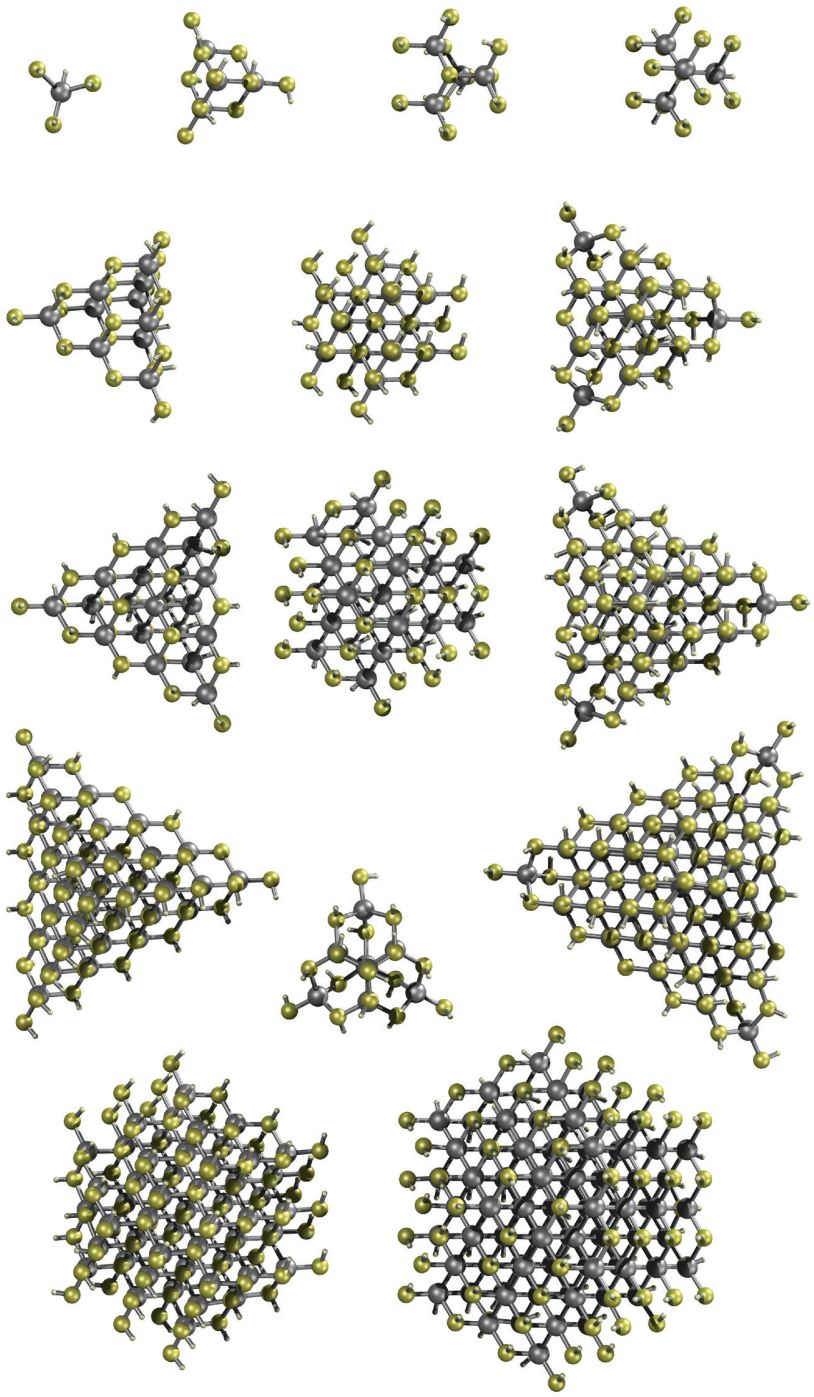

Figure 6.1: *Optimised structures (DFTB) of experimentally characterised surface-saturated nanoparticles. The Cd atoms are represented by grey, S by yellow and H atoms by white spheres. More information on the structures is given in Table 6.3. The corresponding optical excitation spectra are resented in Table 8.1 and Figure 8.2.*

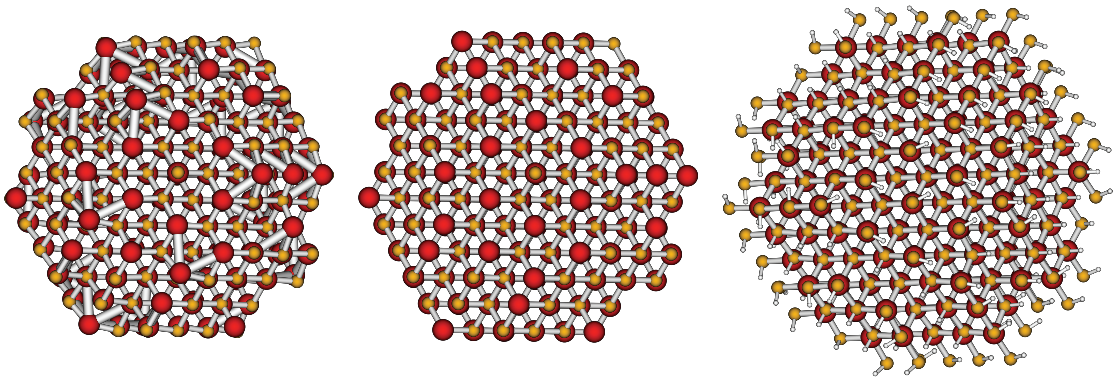

Figure 6.2: *CdS nanoparticles as spherical part of the zinc blende bulk structure* $[CdS]_{192}$ *(middle). The Cd atoms are represented by red, S atoms surface is reconstructed including the shortening of Cd–Cd distances (left), while explicit surfactants maintain the initial structure of the bulk in the nanoparticles* $[Cd_{192}S_{118}(SH_{0\,164}]^{16-}$.

102, 152, 153, 130, 131]. According to Ref. [102], here CdS structures are calculated, where additional to spherical shape also the cuboctahedral and the tetrahedral ones are considered.

The investigations comprises the structure generation starting from the equilibrium structure of the corresponding bulk CdS polymorph, which is in detail explained elsewhere (cf. Section 6.1). Subsequently, the geometries of the nanoparticles with an effective radius $r \leq 1.7$ nm are relaxed with MD simulations that the maximal gradient results below $10^{-4}$ Ha/Bohr. These MD simulations are carried out applying a NVT ensemble with the following parameters: MD temperature $T = 0$ K, which is controlled by a *Berendsen* thermostat [154] applied to each atom independently, and a MD time step $\Delta t = 2$ fs.

The result are in full agreement with *Joswig et al.* [102]. In Figure 6.2 the relaxed structure of a bare, spherical CdS nanoparticles is shown exemplarily. Independent of the initial structure, for nanoparticles with a large number of singly bonded surface atoms, nearest-neighbour (NN) bonds are formed in the structural relaxation neither between Cd atoms nor between S atoms. However the Cd–Cd bond distances result within $3.6 - 3.8$ pm, which is shorter than 4.1 pm in CdS bulk, but still much larger than $\approx 3$ pm in Cd bulk. By analysing the radial distribution of the atoms (cf. Figure 1 in [102]) an outward displacement of the sulfur atoms and inward displacement of the cadmium atoms can be seem for the investigations herein. The inner parts of the nanoparticles largely kept the initial structure of the bulk material. A surface region occurs, whose size is independent of the particle size and consists of the outermost two layers of atoms (corresponding to a thickness of about $2 - 3$ pm).

Similar results are reported by other theoretical studies of CdS and CdSe nanoparticles

[124, 102, 108, 107, 109]. *Galli et al.* [128] describes a self healing of the surface similar to previous reports [127, 155].

Additionally, here also cuboctahedral, as well as, tetrahedral structures are investigated. Their geometries are generated following the scheme, which is given in the beginning of this chapter. The compounds are non-stoichiometric and have the sum formula $(Cd_mS_n)^q$. For both types of structure the same results comparing to the spherical structures are obtained.

Furthermore, nanoparticles with the wurtzite crystal structure of CdS are considered. The results correspond to those of the zinc blende and agree with Ref. [102].

### 6.3.2 Saturated nanoparticles

According to the saturation scheme (cf. Section 6.1.3 the initial structure of bare CdS nanoparticles are saturated, with results compounds with the sum formula $[Cd_mS_n(SH)_i]^q$. These structures with an effective radius $r \leq 1.8$ nm are investigated with the standard DFTB method with respect to their structural properties. Here, the same relaxation scheme (MD simulation) is applied used for the bare structures above. Also this investigations address to the shape, i. e., spherical,** cuboctahedral and tetrahedral, of the particles, as well as, the zinc blende and wurtzite crystal structure.

The relaxed geometries of the saturated CdS nanoparticles result only in marginal structural distortion relative to the initial bulk structure. An example therefore is given in Figure 6.2. The ligand circumvent any diffusion of atoms or formation of homonuclear NN bonds at the nanoparticles' surface. There is no dependence on the result, whether the underlying structure was derived from the zinc blende or wurtzite crystal structure or has a spherical, cuboctahedral and tetrahedral shape.

These findings are in agreement with experimental results for structurally characterised particles (cf. Section 6.2.3 and references therein). Explicit surfactants have already been considered in the studies by *Eichkorn* and *Ahlrichs*, who investigated only small CdSe clusters with DFT [126], as well as by *Gurin* for $Cd_mS_n$ compounds with $m \leq 20$ using *ab initio* methods [104]. In contrast, *Galli et al.* did not find any differences in the structures of surfactant-capped and naked CdSe clusters investigating them with DFT [156].

### 6.3.3 Partial saturation

Corresponding to experimental results, *Talapin et al.* [26] and *Qu et al.* [25] observed the nanoparticles as defect free (completely saturated) when they reach the point of "zero growth", and thus charge-carrier trap free surface. A single missing ligand at one Cd atom already results in a dangling bond, which, in turn, leads to a midgap state which can reduce the luminescence quantum yield (QY) drastically (cf. Section 8.4). The same is observed for a S or Se atom which has two or more dangling bonds [103, 139, 140, 125]. However,

**Cf. Table 6.4 for additional information on the saturation.

these dangling bonds are reactive centres, which should easily find a reaction partner for stabilisation in a solution.

Thus, the question arises how these defects are compensated, thus, the particle is stabilised. Therefore, following the saturation scheme zinc blende type structure, cuboctahedral shaped CdS particles $[Cd_mS_n(SH)_i]^q$ are generated by systematic saturation (cf. Table 6.6):

a) No saturation and only Cd-atoms at the surface,

b) No saturation and only S-atoms at the surface,

c) Structure of 2. and saturation of $(\cdots Cd)_1{-}S$ to $(\cdots Cd)_1{-}S{-}R$

d) Structure of 3. and saturation of $(\cdots Cd)_2{=}S$ to $(\cdots Cd)_2{=}S{-}R$

e) Structure of 4. and saturation of $(\cdots Cd)_3{\equiv}S$ to $(\cdots Cd)_3{\equiv}S{-}R$ which corresponds to a complete saturation.

The number of the compensating charge[††] is minimal for completely saturated structures. In contrast, for partial or non-saturated structures it increases rather fast to values which could not be compensated even in ionic solution. Therefore, two sets of these model structures – one using the compensating charge and the other ignoring any compensation q are used for investigations of their structural stability.

The nanoparticles structures are threaten with MD simulations, applying a NVT ensemble with a MD time step of $\Delta t = 2$fs and the temperature being controlled by a *Berendsen* thermostat [154]. By using the *simulated annealing* technique [157], the structures are slowly heated up to a temperature of 700K, then further propagated at this temperature until equilibration and finally it is cooled down to 0K.

The results of this investigation are summarised in Table 6.6. All structures, with or without charge result in stable structures, except for those having only Cd atoms at their surface. For these particles the surface atoms fragmentise and form Cd clusters. If these structures are not charged they balance their local structure at the surface by reconstruction, forming also S–S and shorter Cd–Cd NN distances (cf. Table 6.6). Of course, these reconstructions are less pronounced with increasing number of ligands (cf. Table 6.6 a)→e) ), that balance the surface charge distribution.

In contrast, the initial CdS bulk structure – even that at the surface – is kept for the nanoparticles structures which are **additionally** stabilised by a compensating charge q (cf. Table 6.6). Nonetheless, within these results the structures missing surfactants, especially that are completely bare, can be electronically stabilised by counter charge. In the present case, the simple adding or subtracting of electrons (counter charge) adjust the electron balance corresponding to the CdS bulk. This is only possible because of a homogenous

[††]Technically in the computation the number of electrons in modified, therefore electrons are added if the charge of the structure is negative or subtracted for positive values.

surface structure of only one atom type. It is not possible in case of inhomogeneous surface structure, i. e., spherical structures (cf. previous two sections). In the most unfavourable case of a stoichiometric, spherical nanoparticles the total charge is zero (cf. Table 6.4). However, the local charge balance at the surface is alternating, which leads to an instable surface structure.

From these results for the structural stabilisation of the CdS nanoparticles the following can be summarised: The structure at the nanoparticles surface is stabilised by the local electronic charge balance. This is realised through surfactants in the first instance and charge q (counter-ions) secondly. If there are no counter-ions available this will lead to distortions at the surface which may cause dangling bonds (and trapped states respectively).

Furthermore, the same can be stated for the case of a single saturation defect, with only one ligand missing in the saturation shell, which also has been calculated, but not presented explicitly. Further discussion and investigations of the impact of defects on the optical properties of CdS nanoparticles are given in Section 8.4.

Table 6.6: *Systematic saturation with ligands and the impact on the structural stability of the nanoparticles as well as the influence of the charge q (cf. Section 6.1.3): Results of a simulated annealing MD study ($T_{max} = 700K$) using the standard DFTB method. The nanoparticles structures are of cuboctahedral shape and having a zinc blende crystal structure. Further details the computation cf. Section 6.3.3.*

| structure $[Cd_mS_n(SH)_i]^q$ | extra charge q=2(m−n)−i | no extra charge q=0≠2(m−n)−i |
|---|---|---|
| a) No saturation and only Cd-atoms at the surface | | |
| $[Cd_{13}S_4]^{18+}$<br>$[Cd_{55}S_{28}]^{54+}$<br>$[Cd_{147}S_{92}]^{110+}$ | stable [a] | fragmented and rebuild surface (Cd-Cd bonds), in core bulk structure stable |
| b) No saturation and only S-atoms at the surface | | |
| $[Cd_{13}S_{28}]^{30-}$<br>$[Cd_{55}S_{92}]^{74-}$<br>$[Cd_{147}S_{216}]^{138-}$ | stable | rebuild surface (S-S bonds and shorten Cd–Cd bonds [a]), in core bulk structure stable |
| c) Saturation only $(\cdots Cd)_1-S-R$ | | |
| $[Cd_{13}S_{16}(SR)_{12}]^{18-}$<br>$[Cd_{55}S_{68}(SR)_{24}]^{50-}$<br>$[Cd_{147}S_{176}(SR)_{40}]^{98-}$ | stable | rebuild surface (S-S bonds and shorten Cd–Cd bonds [a]), in core bulk structure stable |
| d) Saturation only $(\cdots Cd)_2=S-R$ and $(\cdots Cd)_1-S-R$ | | |
| $[Cd_{13}S_4(SR)_{24}]^{6-}$<br>$[Cd_{55}S_{32}(SR)_{60}]^{14-}$<br>$[Cd_{147}S_{104}(SR)_{112}]^{26-}$ | stable | overall stable, but single distortion at surface (S-S bonds and shorten Cd–Cd bonds [a]) |
| e) completely saturated | | |
| $[Cd_{13}S_4(SR)_{24}]^{6-}$<br>$[Cd_{55}S_{28}(SR)_{64}]^{10-}$<br>$[Cd_{147}S_{92}(SR)_{124}]^{14-}$ | stable | overall stable, but single distortion at surface (S-S bonds and shorten Cd–Cd bonds [a]) |

[a] The "shorten" Cd–Cd bonds have NN distances of 3.6 − 3.8pm, which are in the shorter than 4.1pm in CdS-bulk, but still much larger than ≈ 3pm in cadmium bulk.

# 7 Bare versus saturated CdS nanoparticles: electronic properties

With the help of theory and experiment the quantum confinement effect (QCE) was found to govern the physical properties of semiconductor nanoparticles. On the one hand, optical spectroscopy has been the most important method for experimental characterisation, e. g., cf. Refs. [18, 16, 158, 23, 159]. On the other hand, their electronic and optical properties where studied by theory, e. g., cf. Refs. [14, 160, 122, 161, 162, 101, 121, 163, 164, 165, 166, 167, 126, 124, 125, 168, 169, 170, 102, 171]. However, the applied models are in most cases neglecting the atomic structure of the nanoparticles at all or that of the surfactants. If surfactants where included, the structures of the nanoparticles were relatively small compared to the experimentally investigated ones. Thus, a complete picture, i. e., the theory of those, that includes also the surface effects, is still lacking.

In the previous chapter it was shown, that the SCF-DFTB method is able to calculate the electronic structure with a high level of accuracy and moderate calculation time. In the following chapter it will be applied for the systematic investigation of the properties of CdS nanoparticles with sizes up to $r \approx 2$nm for the effective radius ($N_{at} \approx 2000$). The results will be compared to the previous work of *Joswig et al.* [171], who used the standard DFTB method.

The influence of ligands on the surface atoms is studied by contrasting the calculated electronic structures between non and completely saturated nanoparticles. Additionally, the impact on the variation of the underlying crystal structure, as well as the shape of the particles is studied.

## 7.1 Details to the calculation

All structures of the nanoparticles are modelled following schemes, which have been introduced in Chapter 6. Unless, if not stated otherwise, the surface of the nanoparticles has either no ligands attached (bare) or is completely saturated (R=H, cf. 6.2.3).

For nanoparticles of sizes smaller than a radius $r < 1.8$nm) the relaxed geometries, are used (cf. Section 6.3). The larger ones with sizes up to $r \approx 2$nm are treated differently to obtain their minimum energy structure: For the atoms in the core of the nanoparticles the relaxed (using DFTB) crystal structure of CdS is used. By applying the DFTB method,

these atoms are kept fixed at their positions and only the atoms in a surface region of $\approx 0.3$nm thickness are considered in the relaxation.

Exceptions are the CdS nanoparticles with the rock salt crystal structure. Their geometries are modelled, in the first instance similar to the above-mentioned ones by cut-outs of the relaxed bulk structure. In contrast, all Cd, as well as, S atoms are kept fixed for the bare, as well as, for the saturated particles. Thus, only the atomic positions of the ligands are optimised.

Finally, the electronic structure of these nanoparticles is investigated by applying the newly developed SCF-DFTB formalism in the approximate scheme, which has been introduced and successfully tested in Sections 5.2.2 and 5.3.

For the determination of orbital populations and atomic charges the *Mulliken* technique is applied [95]. Additionally, a spherical averaged orbital density is defined, with $N_{ij}$ being the *Mulliken* gross population for the $j$th atom and $i$th orbital:

$$\rho_i(\mathbf{r}) = \sum_j N_{ij} \left(\frac{2\alpha}{\pi}\right)^{\frac{2}{3}} e^{-\alpha(\mathbf{r}-\mathbf{R}_j)^2} \tag{7.1}$$

The value of $\alpha$ is chosen in a way that illustrative figures result.

## 7.2 Electronic structure

In this section, the effects of no and complete surface saturation on the size dependence of the electronic structure of CdS nanoparticles will be investigated in detail. Only one set of structures of nanoparticles is chosen to allow a general survey on the effects of the ligand: The underlying structure is that of the zinc blende modification. The composition is stoichiometric* and the shape is spherical.

### 7.2.1 Surface ionicity

Recent investigations of the electronic structure of bare CdS nanoparticles by *Joswig et al.*, have been using the standard DFTB method [102]. They result in a distinct ionicity of the surface atoms, which are similar to the electronic properties found for surfaces of crystalline CdS and CdSe [108, 107, 109]. Using the own SCF-DFTB, the analysis of the radial charge-distribution of the nanoparticles indicates a surface region. This has a thickness of about 0.3nm (cf. Figure 7.1). In this region in a nanoparticle the charge transfer between Cd and S atoms is much stronger than in the inner part.

Since this ionicity is caused by dangling bonds at the surface of the nanoparticle, a complete saturation of the surface atoms the effect vanishes (cf. Figure 7.1): All over, the

*The classification of stoichiometric and non-stoichiometric structures of CdS nanoparticles is given in Section 6.1.

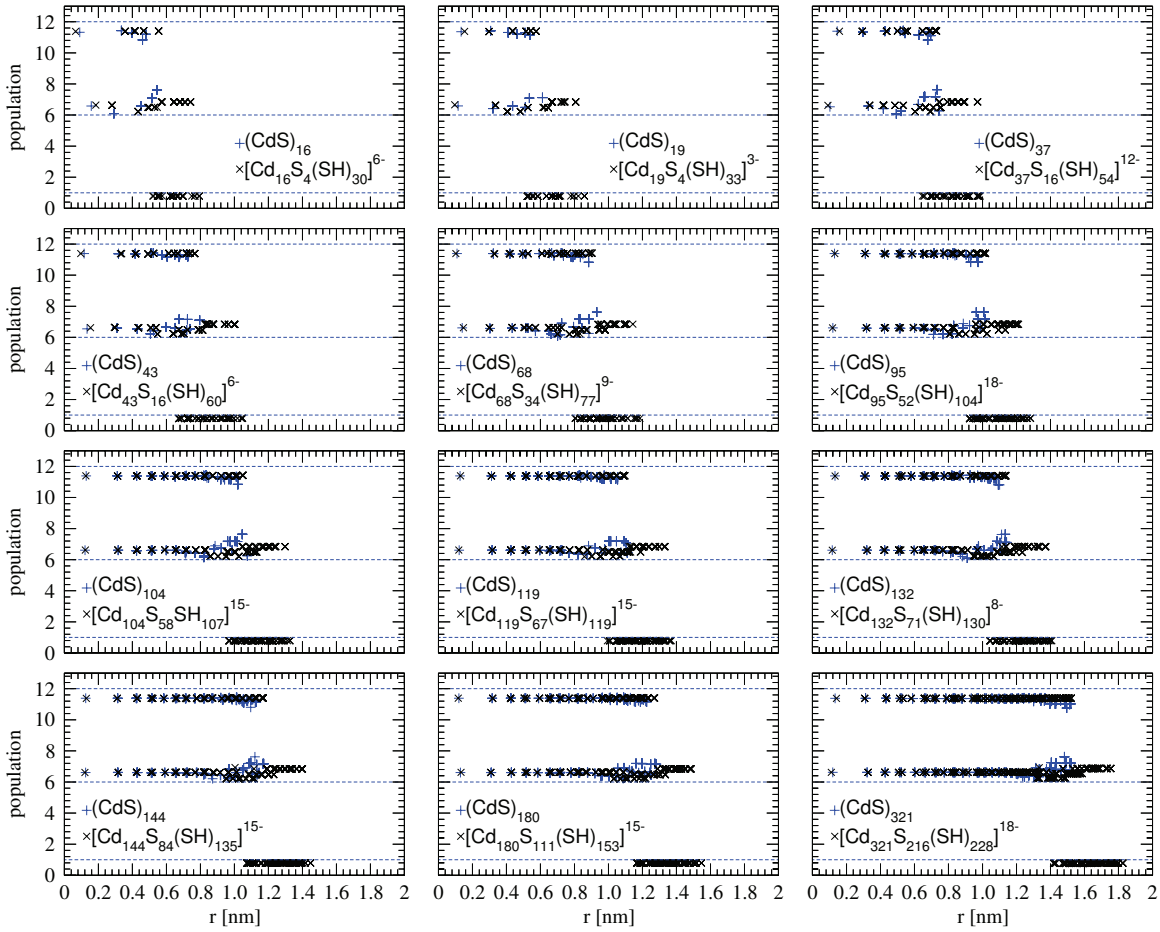


Figure 7.1: *Radial distribution of the Mulliken population for bare* $(CdS)_m$ *(blue symbols) and saturated* $[Cd_mS_n(SH)_i]^{2(m-n)-i}$ *nanoparticles (black symbols) calculated with SCF-DFTB. The number of valence electrons of the free neutral atoms (12 for Cd, 6 for S and 1 for H) is marked by the horizontal dashed lines. Further details on the structures and the computation are given in Section 7.1.*

investigated series, the Cd atoms have a balanced interatomic charge distribution, i. e., the CdS bulk governs. In analogy, this also applies for the sulphur atoms, except those which are directly bound to a surfactant. In the detail, the three different population values that result for these sulphur atoms, are due to the different chemical environment compared to the bulk CdS (cf. Section 6.1.3). The influence on the electronic structure with respect to different types of surfactants than R=H is not addressed, but may be relevant.

SCF-DFTB and DFTB give qualitatively the same results:[†] the *Mulliken* charges of the atoms in the core of the nanoparticles have the calculated values of the bulk. Thus, with improved CT description of SCF-DFTB they are approximately twice as large as with standard DFTB, and fit to the full DFT results (cf. Chapter 5).

### 7.2.2 Representing the electronic DOS of the CdS bulk

The calculated electronic DOS profiles (SCF-DFTB) of the bare ($(CdS)_m$) and saturated ($[Cd_mS_n(SH)_i]^{2(m-n)-i}$) CdS nanoparticles are given in Figure 7.2. For all structures the electronic DOS profiles for the occupied states are rather similar. They, further, correspond to the electronic DOS of the bulk structure (cf. Figure 7.7). However, the unoccupied states of the saturated particles with different sizes are similar, while the non-saturated structures differ qualitatively. Here, the most noticeable feature is the much smaller HOMO-LUMO gap compared to the saturated structures and to the bulk. The analysis of the projected DOS (pDOS) shows that these states can be addressed to low-lying 5*s* states of surface-located Cd atoms with dangling bonds. Clear from Figure 7.3, these are lowered in energy compared to the complete saturated structures, which result in smaller values of the HOMO-LUMO gap.

The results for the electronic DOS of the bare structures are in agreement with *Joswig et al.*, who studied bare CdS nanoparticles with the standard DFTB method. Moreover, previous investigations on the electronic structure of CdS nanoparticles using different theoretical models result in rather similar electronic DOS profiles, which also correspond to the electronic DOS of the bulk structure [101, 102, 103, 104].

### 7.2.3 The QCE and the HOMO-LUMO gap

For nanoparticles of direct semiconductors the value of the HOMO-LUMO gap energy should approximately represent the lowest optical excitation energy. Due to the quantum confinement effect (QCE), an overall decrease of these values with respect to an increasing size of the nanoparticles is observed experimentally (e. g., cf. Ref. [2]).

Using the SCF-DFTB method, the HOMO-LUMO gap energies $\Delta_G$ of bare and full saturated nanoparticles are shown in Figure 7.4 as a function of their diameter. Additionally,

[†]For the saturated structures this has been proven in this work, but is not further highlighted.

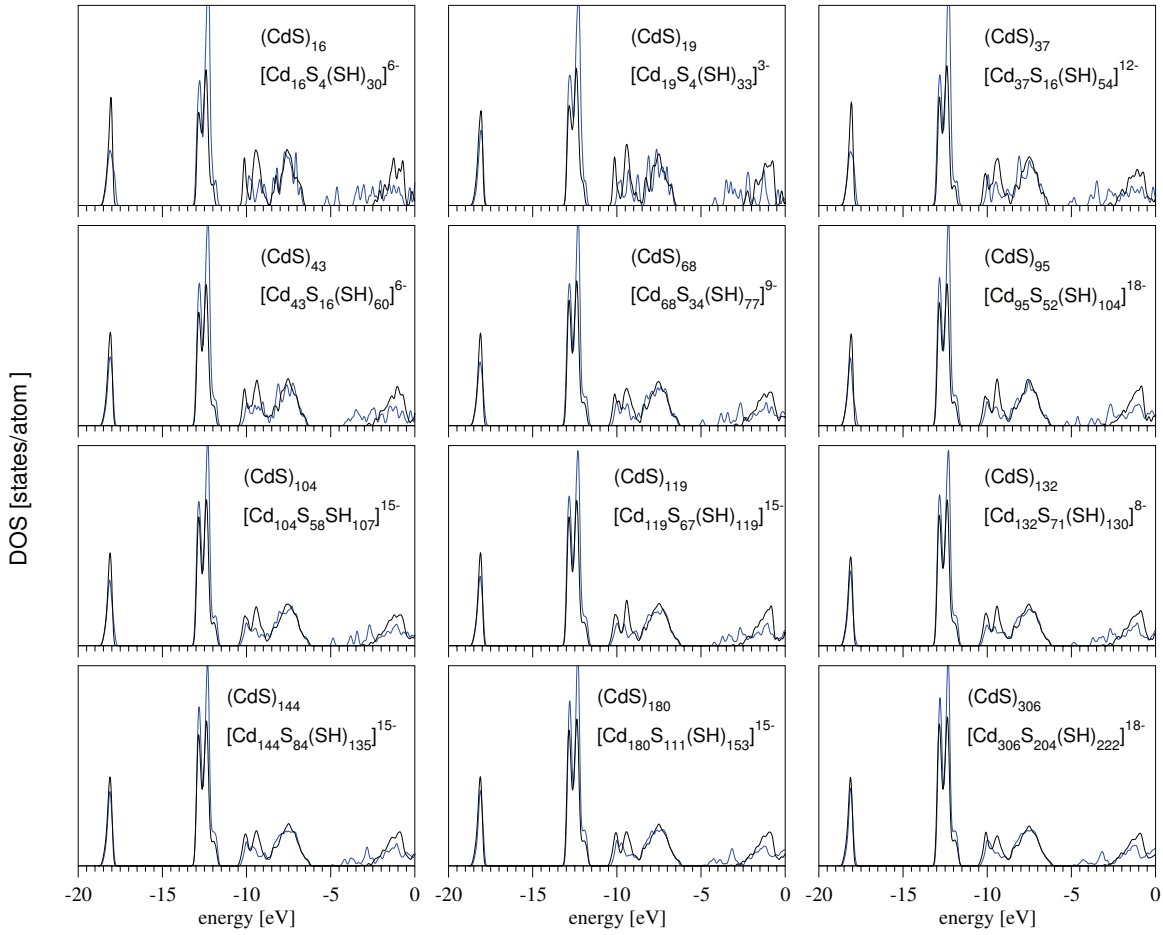


Figure 7.2: *Calculated electronic DOS of spherical CdS (zinc blende) nanoparticles: Bare* $(CdS)_m$ *(blue curves) and completely saturated* $[Cd_mS_n(SH)_i]^{2(m-n)-i}$ *(black curves). The values are broadened with Gaussian functions for better depiction. Further details on the structures and the computation are given in Section 7.1.*

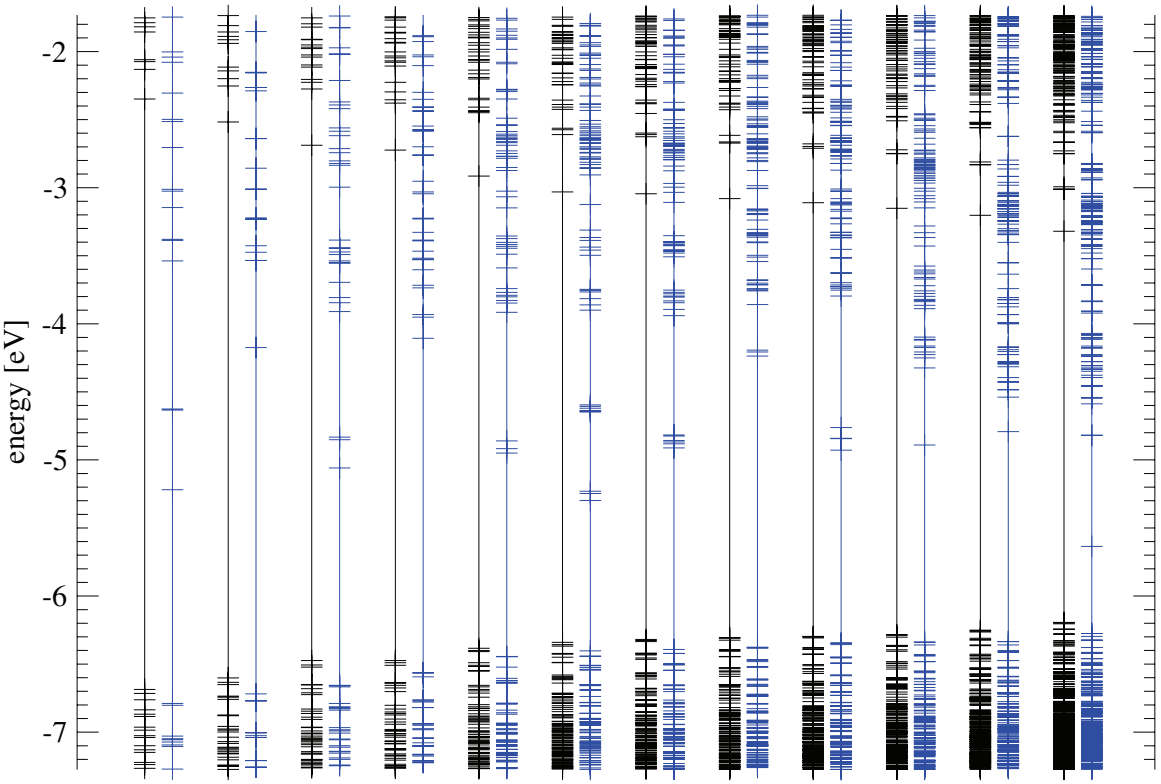


Figure 7.3: *Calculated eigenvalue spectra of the states around the Fermi-level: MO energies of bare (blue curves) and completely surface-saturated (black curves) are drawn pair wise for increasing particle size corresponding to structures presented in Figure 7.2. The HOMO of these structures is located between* $-6.7$ *and* $-6.2eV$.

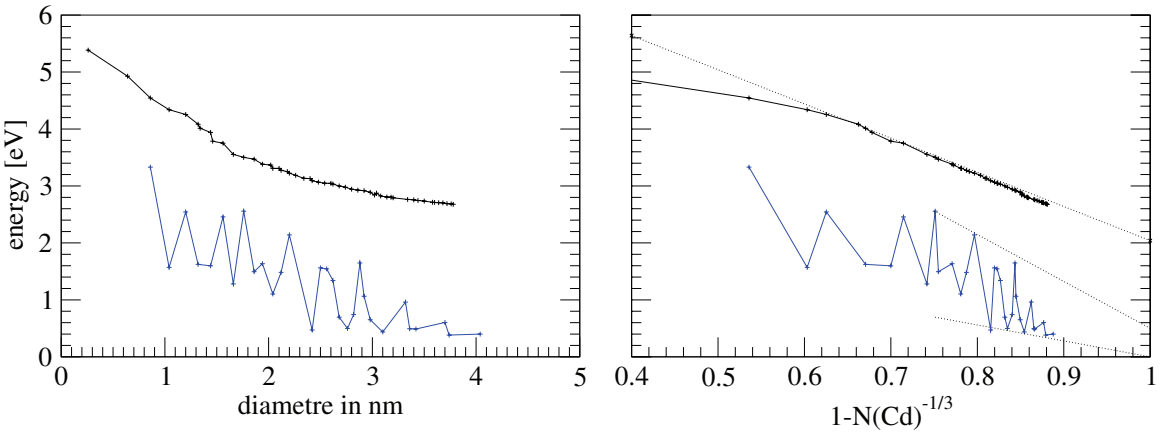


Figure 7.4: *Calculated HOMO-LUMO gap energies of spherical nanoparticles with zinc blende structure: Bare* $(CdS)_n$ *(blue symbols) and complete saturation at the surface* $[Cd_mS_n(SH)_i]^{2(m-n)-i}$ *(black symbols) using SCF-DFTB. Further details on the structures and the computation are given in Section 7.1.*

the gap size is drawn as a function of

$$\lim_{n_{\mathrm{Cd}}\to\infty} \Delta_G \left(1 - n_{\mathrm{Cd}}^{-1/3}\right) = \Delta_G^{\mathrm{bulk}}, \tag{7.2}$$

with $n_{\mathrm{Cd}}$ being the number of Cd atoms, CdS pairs, respectively. The advantage of the latter representation is the direct comparison to the band gap value of the bulk $\Delta_G^{\mathrm{bulk}}$, with

$$\lim_{n_{\mathrm{Cd}}\to\infty} \left(1 - n_{\mathrm{Cd}}^{-1/3}\right) = 1. \tag{7.3}$$

For bare nanoparticles, the gap energies are irregularly oscillating with increasing size of the particles, but they show a weak overall decrease. These oscillations are due to the varying number of singly bonded Cd atoms at the surface. For those structures with a high number of these atoms the extrapolated HOMO-LUMO gap energy (7.2) for infinite particle size (7.3) would asymptotically lead to a zero gap. Thus, the character of the surface becomes metallic-like. Nanoparticles with a low number of singly bound Cd atoms at the surface result in larger values for the HOMO-LUMO gap energy. Here, Eq. (7.3) results in a non-zero gap for the bulk limit, as shown in Figures 7.4 and 7.8. The size of this extrapolated gap is $\approx$ 0.7eV, which is still below the calculated value for the zinc blende bulk with 2.2eV.[‡] Thus, the experimentally observed QCE is not obtained for structures without surface saturation.

However, these results are in qualitative agreement with the investigation of bare CdS nanoparticles with the standard DFTB method [171]. Quantitatively, the obtained value of the extrapolated HOMO-LUMO gap energy for the particles with a minimum number of singly bound Cd atoms is double as large. This difference is of methodological origin, since the applied standard DFTB method overestimates the band gap energies (cf. Section 5.1).

Nonetheless, the QCE for the HOMO-LUMO gap energy is obtained for complete surface-saturated nanoparticles ($[\mathrm{Cd_mS_n(SH)_i}]^{2\,(\mathrm{m-n})-\mathrm{i}}$). In Figure 7.4 the calculated gap energies are depicted. For all structures the corresponding value decreases asymptotically towards the calculated value of the bulk (2.2eV). This is clear from Figure 7.5. The absolute energy values of the HOMO and LUMO trend asymptotically towards the valence band and conduction band edge. Moreover, in this Figure 7.4 the electronic structure of CdS is directly compared starting from the molecular level and toward the bulk limit: With increasing size of the structures the "condensation" of the electronic states takes place, which in the extended bulk form bands. Here, the conduction band and the valence band show dispersion at the Γ-point. This corresponds to spatial delocalisation of the electronic wavefunction. When comparing this with the electronic DOS of the bulk Figure 5.3, the conduction band exhibit the *free electron* character. A similar behaviour results for corresponding electronic DOS of the finite structures. Here the lowest unoccupied molecular orbitals (LUMOs) have a correspondingly low DOS. Nonetheless, the QCE is more pronounced for the LUMOs, than

[‡]cf. Section 5.3

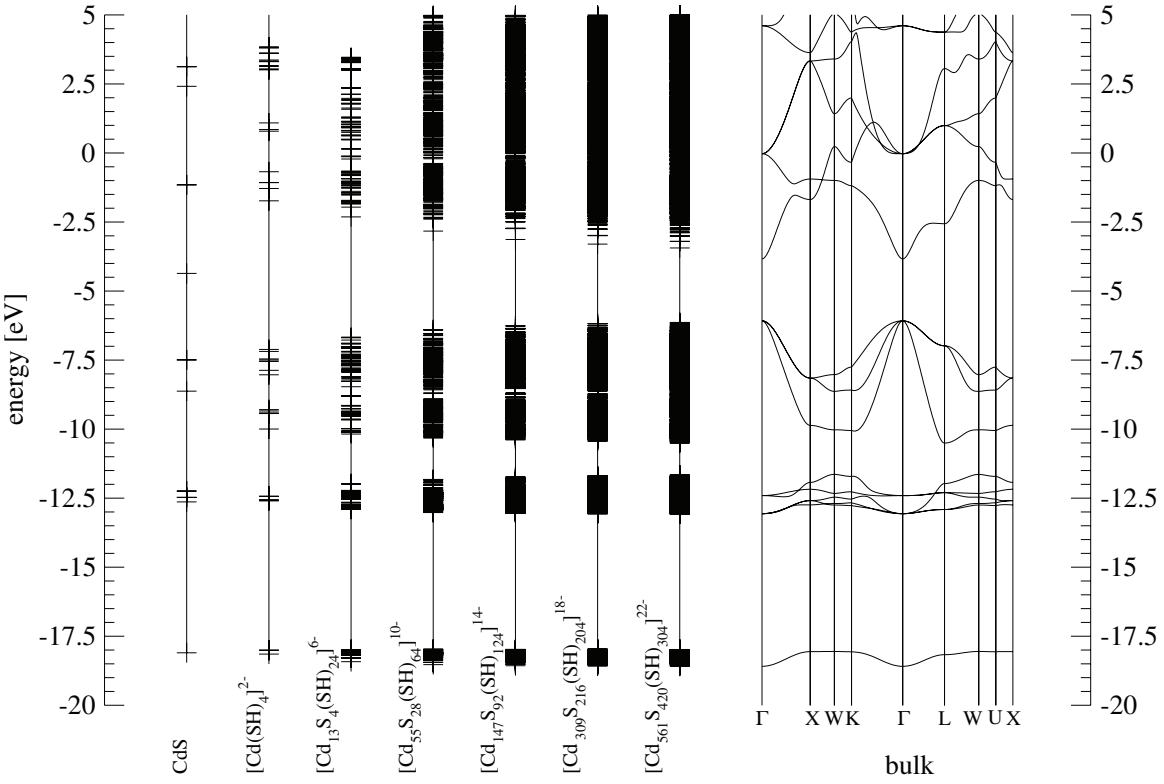


Figure 7.5: *Size-dependent eigenvalue spectra (SCF-DFTB) from CdS-dimer to the bulk bandstructure (zinc blende), with the valence band edge at* $-6.07eV$ *(*$\Gamma-$*point). The structures (zinc blende) in between are of cuboctahedral shape. Further details on the structures and the computation are given in Section 7.1.*

for the HOMOs.[§] The spacing between the energy levels is much larger for the LUMOs, than for the HOMOs.

The results of the HOMO-LUMO gap energy of completely saturated CdS nanoparticles are in agreement with the measured values of the lowest absorption energies of the corresponding, saturated experimental structures, e. g., cf. Ref. [16]). Moreover, they are in agreement to investigations using empirical TB models or semi-empirical pseudopotential methods for the calculations of non-saturated CdS (CdSe) nanoparticles, e. g., cf. [122, 172, 121, 168]. The authors excluded the dangling bond orbitals explicitly and the latter one used point charges for compensating these dangling bonds. This explains the contrary results compared to this work.

### 7.2.4 The frontier orbitals and reactivity

Detailed knowledge of the frontier orbitals, i. e., HOMO and LUMO, are important for understanding the optical processes, but they also contribute as well to the understanding of the reactivity of the nanoparticles, e. g., the binding of surfactants.

Therefore, spherical averaged orbital densities are calculated from the projections of the atomic functions contributing to the HOMO and LUMO, which are obtained from SCF-DFTB calculations. The results for bare and complete saturated CdS nanoparticles are given in Figure 7.6: Independent of the size of the particles, the HOMO is spatially delocalised over the structure. In contrast, due to the non-saturated Cd atoms the LUMO is localised to a large extend at the surface atoms at dangling bonds. These results are in agreement to the similar investigation, bare CdS nanoparticles using the standard DFTB method [102, 171].

As it has been shown in the previous section, at the surface the electronic structure is destabilised due to the reduced coordination, which is compensated by increased ionicity and lowering of the unoccupied MO energies (mid-gap states). In the framework of the *hard and soft acids and bases* (HSAB) principle [143], the surface atoms are of increased reactivity: The dangling bonds at the Cd atom(s) (mainly Cd 5s states) are electron acceptors (*Lewis* acids). The S atoms are electron donators (*Lewis* bases).

In contrast, if the dangling bonds are completely saturated by surfactants the spatial localisation of the LUMO at the surface vanishes. This fact is clear from the calculated spherically averaged orbital densities of the HOMO and the LUMO in Figure 7.6). Both frontier orbitals are fully delocalised over the whole nanoparticle. A projection to the atomic contributions shows, that the HOMO consists mainly of S $3p$ functions, whereas Cd $5s$ functions mainly participate in the LUMO. This delocalisation is similar to the electronic structure of the valence and conduction band at the $\Gamma-$point CdS bulk (cf. Figure 7.5).

Thus, these completely saturated structures are less reactive, since in fabrication surfactants are also used to decrease their reactivity. However, dangling bonds are

[§]The LUMOs are shifted to higher energies, while the HOMOs are shifted down, respectively.

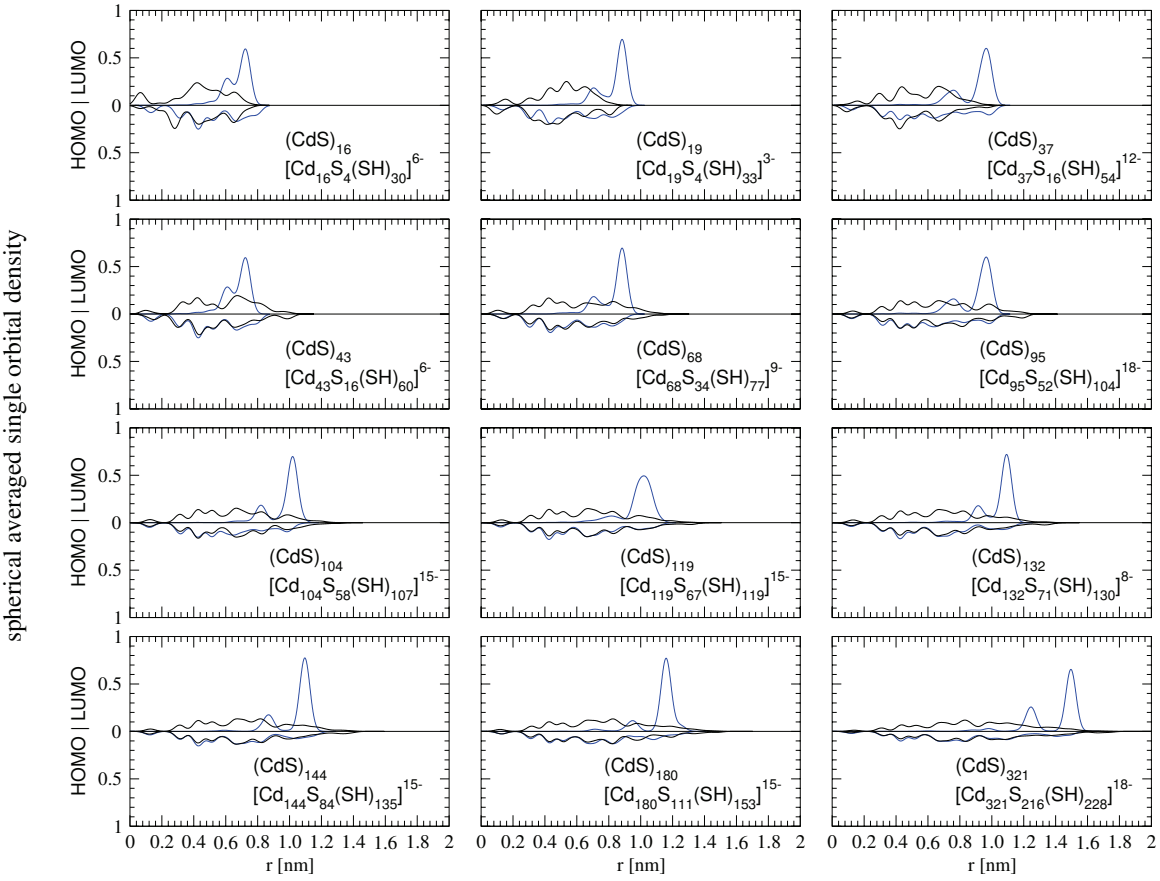


Figure 7.6: *Spherically averaged orbital densities of the HOMO (downward pointing) and the LUMO (upward pointing curves): Bare* $(CdS)_n$ *nanoparticles (blue curves) and complete surface-saturated nanoparticles* $[Cd_mS_n(SH)_i]^{2(m-n)-i}$ *(black curves). The values are broadened with Gaussian functions for better depiction. Further details on the structures and the computation are given in Section 7.1.*

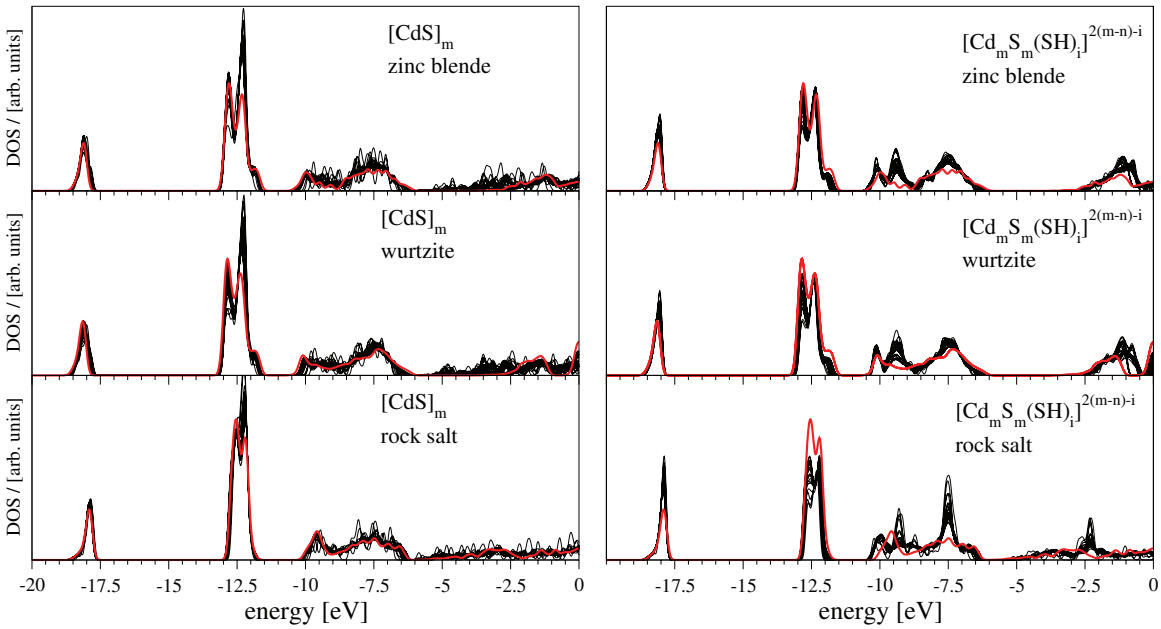


Figure 7.7: *Calculated electronic DOS of bare (left column) and complete surface-saturated (right column) nanoparticles representing the size-spectrum radii of* $r \approx 2$ *(black curves) and of the corresponding bulk modification (red curves). The energies of the HOMO and respectively valence band energies are the range of* $-6.7$ *and* $-6.2eV$*. Further details on the structures and the computation are given in Section 7.1.*

observed at both atom types for experimentally stable surface-saturated nanoparticles [103, 123, 139, 140, 125].

In general, the properties of this type of nanoparticles are depending sensitively on variations of the surface structure, which predominantly affects those properties, which are connected to the frontier orbitals, e. g., optical properties. On these we are focus in Section 8.3.

## 7.3 Structure and shape

In this section the electronic structure of the CdS nanoparticles are investigated focusing on the influence of crystal the structure and their shape. Thus, additionally to the zinc blende structure the wurtzite, as well as, the high-pressure rock salt phase will be considered. The influence of the shape is studied including spherical, cuboctahedral and tetrahedral geometries.

At first, the eigenvalue spectra of bare and fully surface-saturated, spherical nanoparticles based on the three modifications of bulk CdS are calculated with the SCF-DFTB method. The resulting electronic DOS of these structures in the size range of the radii $r = 0.5, \ldots, 2.0$ nm are given in Figure 7.7. For comparison, the corresponding electronic DOS profiles of the bulk are overlaid: In the first approximation the curves of the non-

saturated particles $[CdS]_m$ with $m = 1, \ldots, 600$ show no significant difference with respect to their different underlying structures. But the comparison to the electronic DOS of their corresponding bulk structure shows, that the electronic states, and especially that around frontier orbitals, deviate. In detail, the variation of the values of the LUMO energy caused by dangling bonds at surface-located Cd atoms is independent of the underlying crystal structure of the nanoparticles.

Secondly, calculations are repeated for complete saturated nanoparticles. These are of the composition $[Cd_mS_n(SH)_i]^{2(m-n)-i}$ with $m = 1, \ldots, 600$. The obtained electronic DOS profiles are very similar to each other and they are rather similar to the corresponding bulk structures. Minor deviations are caused by additional contributions of the ligands (R=H) at approximately 9.25eV. These are slightly more distinctive for the nanoparticles with rock salt structure. For this structure type the states at 7.5eV originate from S atoms at the surface linking to the surfactants with a high coordination of cadmium providing an excess electronic density (cf. Figure 7.7).

Previous investigations of CdS also give similar agreement of the electronic DOS between different sized nanoparticles and the corresponding bulk [105, 106, 107, 108, 109, 110, 102].

Furthermore, the trend of the HOMO-LUMO gap energies with respect to the size and the crystal structure is clear from Figure 7.8: Qualitative and nearly quantitative agreement of the gap energies is obtained for the zinc blende and wurtzite structure (cf. Section 7.2.3). Thus, the structural and energetic similarities of the bulk are achieved also for the nano-size regime. The curves of the saturated particles with the rock salt structure show the same decaying behaviour. However, minor deviations are emerging, which can be addressed to the non-relaxed atomic geometries (cf. Section 7.1). Further refinement could be obtained by simulating these structures at experimental conditions [173, 174, 22], e. g., using a pressure bath.

Also for particles, which miss any surface protection the energy values of the HOMO-LUMO gap are independent of the underlying crystal structure. As shown in Figure 7.8, these result in much smaller values, which are below those of the corresponding bulk. They show an irregular oscillating behaviour for all three crystal structures (cf. Section 7.2.3).

An influence of the shape of the nanoparticles is also not obtained. The calculated energy values of the HOMO-LUMO gap of completely saturated structures with spherical, cuboctahedral and tetrahedral shape are summarised in Figure 7.9. The trend curves of the gap energy with respect to the size of the clusters coincide.[¶]

Finally, the investigations show, that the QCE is independent of the crystal structure and the shape, but essentially depend on the surface structure of the nanoparticles.

[¶]Here, the number of Cd atoms is used to specify the size of the cluster.

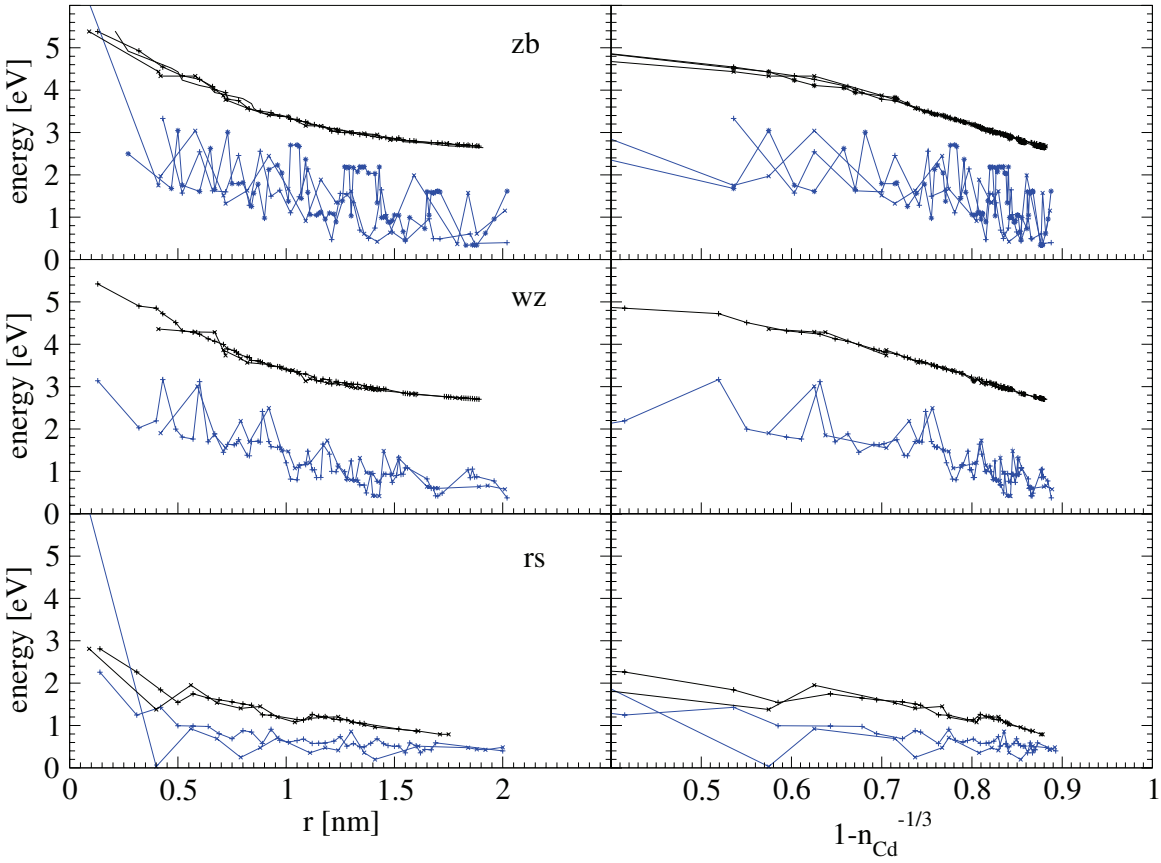


Figure 7.8: *Calculated HOMO-LUMO gap energies of the CdS nanoparticles with respect to the different structures: zinc blende (zb), wurtzite (wz) and rock salt (rs) of bare* $[CdS]_m$ *(blue curves) and surface-saturated* $[Cd_mS_n(SH)_i]^{2(m-n)-i}$ *(black curves). On the left side of the panel the gap energies are plotted with respect to the radius r of the structures, while on the right side they follow Eq. (7.2). Further details on the structures and the computation are given in Section 7.1.*

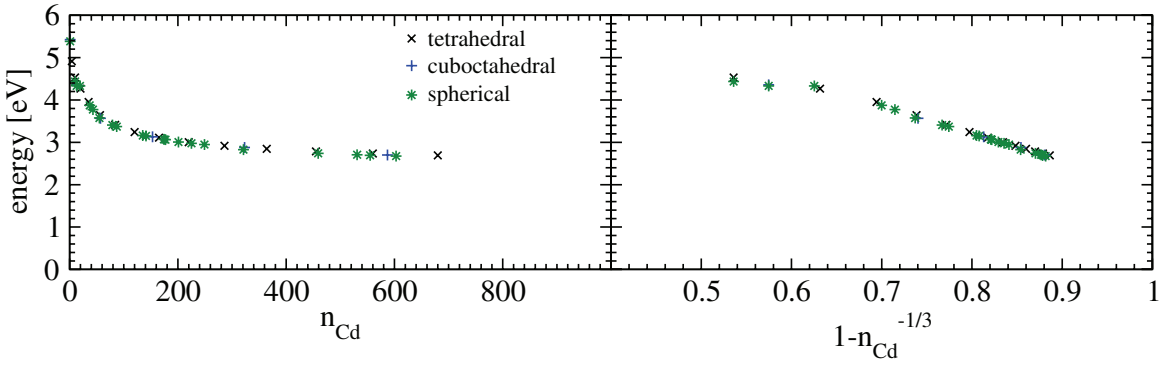


Figure 7.9: *Size-dependence of the HOMO-LUMO gap with respect to a different shaping of CdS nanoparticles: Spherical, cuboctahedral and tetrahedral. The underlying structures are zinc blende based, surface-saturated nanoparticles* $[Cd_mS_n(SH)_i]^{2(m-n)-i}$ *calculated with SCF-DFTB. Further details on the structures and the computation are given in Section 7.1.*

# 8 Optical properties of CdS nanoparticles

In the previous chapters it has been shown, that the electronic structure of CdS nanoparticles is sensitive to the underlying atomic structure. Especially that of the surface has a major impact on the orbitals closest to the *Fermi* level. Hence, the role of surface passivation also becomes of elementary relevance for the optical properties of the particles.

Extensive experimental investigation of the optical processes in semiconductor nanoparticles have been made possible through the availability of monodisperse size fractions [16]. The results of these studies and those obtained from theoretical models give a clear evidence, that the electronic states located at the surface of the nanoparticles are involved in the optical process [175, 176, 103, 107, 101, 109, 165, 125]. Defects in the surface saturation are known to generate dangling bonds, which in turn cause trapped states. In contrast, the best efficiency in the photoluminescence quantum yield, a so-called "bright point", was reported, for nanoparticles with an optimal, defect-free and thus a charge-carrier trap-free surface structure [25, 26, 27].

In the following, the focus is set on the influence of the surface states and their passivation with respect to the optical excitation spectra of CdS nanoparticles. Therefore the calculation scheme of the $\gamma$-approximation is applied, which in a linear-response scheme taking into account collective effects and selection rules (cf. Section 3.8). Moreover, the underlying structure becomes of interest, if the type of semiconductor changes from a direct band gap semiconductor to an indirect one [173, 174, 22].

At first, the $\gamma$-approximation is tested for the CdS system. Therefore a set of smaller clusters is chosen, from which the structure is known experimentally (cf. Chapter 6).

## 8.1 Details of the computation

For the investigation of the optical properties of CdS nanoparticles the same atomic structures are used, as in the previous chapter. The corresponding details are given in Section 7.1.

For the calculation of the absorption spectra the $\gamma-$approximation is applied, which has been introduced in Section 3.8. The MO energies and coefficients, that are needed, have been calculated with the SCF-DFTB method. The $\omega_I$ in Eq.(3.27) denote the linear-response excitation energies, and $\omega^{KS}$ are the single particle excitation energies of the static *Kohn-Sham* calculation. These are also constructed from the SCF-DFTB eigenvalues and eigenvectors, include selection rules, but no collective effects. The oscillator strengths $f^I$ are calculated within a dipole approximation [cf. Eq. (3.36)]. Likewise, the single-particle

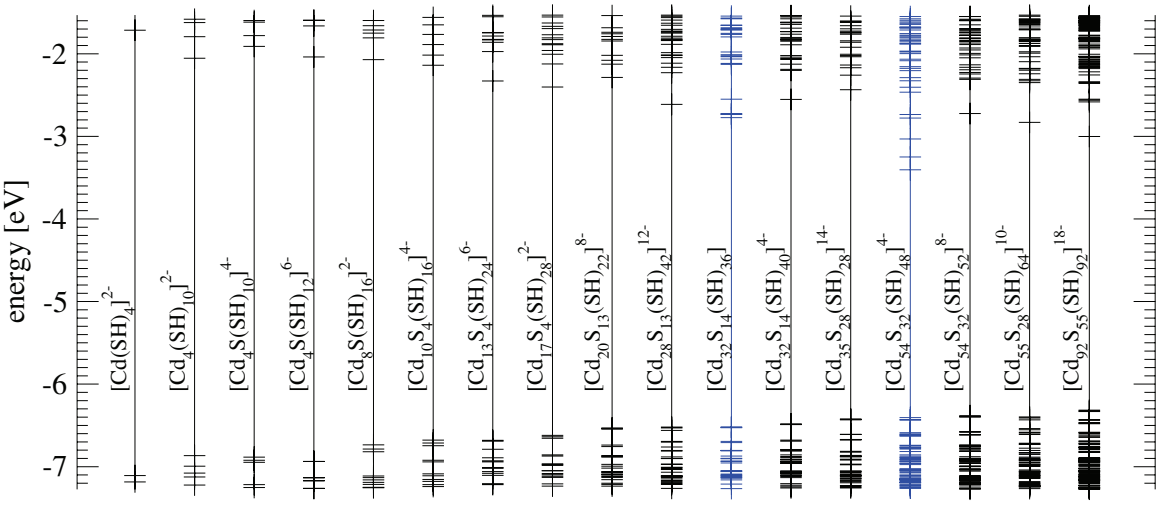


Figure 8.1: *Calculated eigenvalue spectra of the MO's close to the Fermi level: Small surface-saturated (black curves) nanoparticles and two with missing four ligands each (blue curves). More information in the structures are given in Table 8.1 and the corresponding optical excitation spectra in Figure 8.2.*

spectra are obtained neglecting the coupling-terms. The presented spectra are broadened by *Gaussian* functions.

## 8.2 Reference calculation – small CdS nanoparticles

### 8.2.1 Onset excitation

The clusters of the test set are summarised in Table 8.1 including the appropriate references.* Further the calculated lowest excitation energies $\omega_I$ and $\omega^{KS}$ are summarised and compared to the corresponding experimentally determined values. The calculated MO eigenvalue spectra of the states closest to the *Fermi* level are given in Figure 8.1.

In agreement with the experimental values, the calculated ones are decreasing with increasing number of cadmium atoms, and Cd–S pairs respectively. Their absolute values result in the range of $5.5-3.4$eV, which is above the bulk limit (2.58eV [11]). In general, the calculated lowest singlet-excitation energies $\omega_I$ vary within $\pm 20\%$ compared to the experimental values. These deviations may be due to several reasons: First, model structures are used, which are saturated with hydrogen atoms instead of thiol-phenolate or aliphatic thiolate ligands, as in the experiment. Thus, the influence of larger ligand molecules on the optical properties is not covered. The deviations are especially large when the surfactant is a chromophore (e. g., phenolate) itself that is incorporated in the optical process [141]. Second, the overbinding effect of the LDA has to be considered, as the absolute value for band gap of CdS is underestimated by 10% compared to the experiment by using SCF-DFTB.

*A general structure classification of small CdS nanoparticles is given in the Appendix A.

Table 8.1: *Calculated lowest excitation energies of small CdS nanoparticles. The corresponding cluster structures are depicted in Figure 6.1. Further details on the computation and on the used symbols are given in Section 8.1.*

| Compound | Structure[a] | $\omega^{KS}$ [eV] | $\omega_I$ [eV] | $\omega_{\text{exp}}$ [eV] | Reference |
|---|---|---|---|---|---|
| $[Cd(SR)_4]^{2-}$ | mix | 5.39 | 5.54 | 5.17[b], 4.40[c] | [146] |
| $[Cd_4(SR)_{10}]^{2-}$ | tetr | 4.81 | 4.90 | 4.98[c] | [147, 146] |
| $[Cd_4S(SR)_{10}]^{4-}$ | wz | 4.97 | 5.04 | | [24] |
| $[Cd_4S(SR)_{12}]^{6-}$ | cubo | 4.80 | 4.98 | 4.77[b] | [122] |
| $[Cd_8S(SR)_{16}]^{2-}$ | mix | 4.67 | 4.72 | 4.43[b] | [148] |
| $[Cd_{10}S_4(SR)_{16}]^{4-}$ | tetr | 4.54 | 4.59 | 4.88,[b] 4.25[c] | [113, 114, 146] |
| $[Cd_{13}S_4(SR)_{24}]^{6-}$ | cubo | 4.35 | 4.43 | | [122] |
| $[Cd_{17}S_4(SR)_{28}]^{2-}$ | mix | 4.22 | 4.27 | 4.28[b] | [119] |
| $[Cd_{20}S_{13}(SR)_{22}]^{8-}$ | tetr | 4.25 | 4.29 | 3.53[c] | [149] |
| $[Cd_{28}S_{13}(SR)_{42}]^{12-}$ | cubo | 3.91 | 3.97 | | [122] |
| $[Cd_{32}S_{14}(SR)_{36}]^{0}$ | mix | 3.75 | 3.75 | 3.82,[b] 3.46[c] | [120, 118] |
| $[Cd_{32}S_{14}(SR)_{40}]^{4-}$ | mix | 3.93 | 3.99 | | [d] |
| $[Cd_{35}S_{28}(SR)_{28}]^{14-}$ | tetr | 3.99 | 4.03 | 3.82[c] | [149] |
| $[Cd_{54}S_{32}(SR)_{48}]^{4-}$ | mix | 3.00 | 3.04 | 3.70[b] | |
| $[Cd_{54}S_{32}(SR)_{52}]^{8-}$ | mix | 3.66 | 3.71 | | [d] |
| $[Cd_{55}S_{28}(SR)_{64}]^{10-}$ | cubo | 3.57 | 3.63 | | [122] |
| $[Cd_{92}S_{55}(SR)_{92}]^{18-}$ | cubo | 3.31 | 3.36 | 3.35[b] | [122] |

[a] The abbreviations denote different shapes and crystal structures: wz: wurtzite; tetr: zinc blende tetrahedron; cubo: zinc blende cuboctahedron; mix: mixed zinc blende-wurtzite.

[b] The ligands are aliphatic thiolates.

[c] The ligands are thiophenolates.

[d] These structures are modelled by adding four additional ligands to each of the edges of the experimental structures $[Cd_{32}S_{14}(SR)_{36}]^0$ and $[Cd_{54}S_{32}(SR)_{48}]^{4-}$.

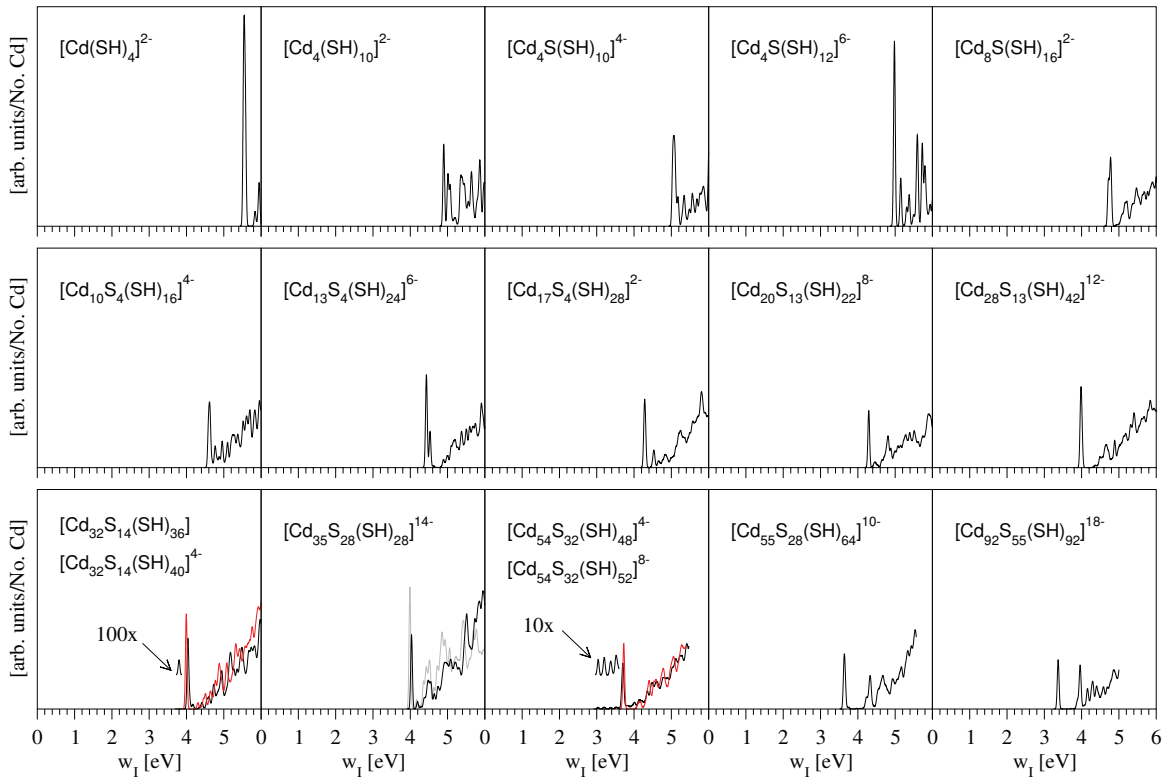


Figure 8.2: *Calculated linear-response singlet-absorption spectra ($\gamma$-approximation) of small surface-saturated CdS nanoparticles (black curves). The trapped states are depicted with scaled oscillator strength. Additionally, the corresponding spectra for the complete saturation structures $[Cd_{32}S_{14}(SR)_{40}]^{4-}$ and $[Cd_{54}S_{32}(SR)_{52}]^{8-}$ are added (red colour). All curves are normalised with respect to the number of Cd atoms. For one structure the excitation spectra within single particle scheme is given (grey colour). Further details on the used symbols and computation are given in Section 8.1.*

This effect is hardly compensated by the $\gamma$-approximation, which is known to overestimate the singlet-excitation energies.[†] Furthermore, solvent effects are found to have no significant impact on the electronic and optical properties and can be neglected in the calculation [168]. In summary, the calculated values are well within the error bars of the experiments (cf. Figure 8.12).

### 8.2.2 Absorption spectra

The calculated singlet-absorption spectra of the test set are shown in Figure 8.2. Beside the energies of the onset excitation, the most eye-catching feature in almost all spectra is the high oscillator strength of the onset absorption peak. These excitations are of excitonic character.[‡] The hole wavefunction consist mainly of contributions from the HOMO$-i$ with

[†] cf. Section 3.8.3

[‡] An electron-hole pair is names "exciton".

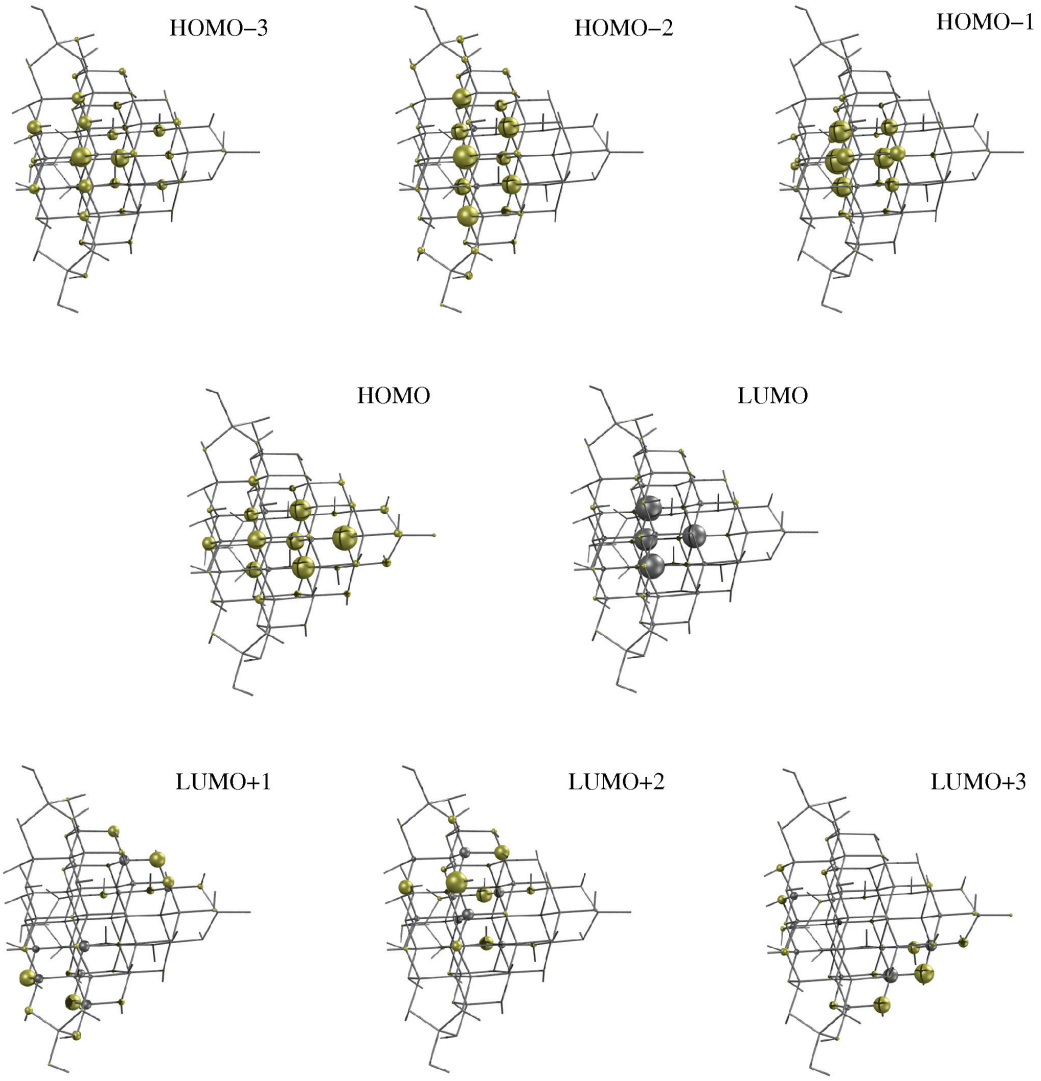


Figure 8.3: *Frontier orbitals of* $[Cd_{32}S_{14}(SR)_{40}]^{4-}$*: The four missing ligands at the vertices of the structure* $[Cd_{32}S_{14}(SR)_{36}]^{0}$ *(cf. Figure 8.4) are added. The optical properties are discussed in Sections 8.2 and 8.4. More information in the structures are given in Table 8.1 and the corresponding optical excitation spectrum in Figure 8.2. The SCF-DFTB MO energies are depicted in Figure 8.1. For better depiction the MO's (SCF-DFTB) are approximated by the projected atomic contributions (sulphur yellow; cadmium grey colour) to the orbital (*Mulliken*-population analysis) represented as spheres centred at the corresponding atom.*

$i = 0, 1, 2$, whereas the electron wavefunction is exclusively from the LUMO. The HOMO$-i$ are almost degenerated, as they span the maximum energy range of 1meV. A projection of the atomic contributions to these orbitals using the *Mulliken* population analysis shows, that all HOMO$-i$ and LUMO are spatially delocalised over the nanoparticle. Thus, both, electron and hole wavefunctions are of $s$ character (cf. Figures 8.3 and B.4). The contributions to the occupied orbitals HOMO$-i$ originate 80 % from S atoms ($3p$ functions) and 20% Cd atoms ($5s5p$ functions), whereas that of the LUMO are 70% from mainly Cd $5s$ functions and 30% S $3p3d$ functions. For the latter ones are to a large extend located at the surface S atoms to which the ligands bind, as visualised in Figure B.5.

### 8.2.3 Surface states

The result changes for the nanoparticles with dangling bonds, since each of the four missing ligands cause "trapped states". These are located at the non-saturated Cd atoms at the surface, which can be directly seen in Figures 8.4 and B.3 showing the atomic contributions to MO's.[§] Clear from Figure 8.2, their onset absorptions have lower excitation energies and almost negligible oscillator strength. However, a strong excitonic absorption, that correspond to the onset peak in the spectra of the completely saturated structures, is obtained for both structures, with slightly higher excitation energies, but reduced oscillator strengths. Here the following MO's contribute to the hole and electron wavefunction: HOMO$-i$, with $i = 0, 1, 2$ and LUMO+4. Further investigations of saturation defects (dangling bond(s)) and their impact on the optical properties follow at the end of this chapter in Section 8.4.

Already, this small nanoparticles exhibit an excitonic character in the onset excitation. This is due to the same spatial delocalisation of the MO's involved in the transition (HOMO$-i$ and LUMO) and, thus, a maximum overlap of the excitonic wavefunction.

In contrast, collective effects are of minor importance. Here the excitation spectra calculated with the single particle (SP) scheme fit to the $\gamma$-approximation. The excitation energies $\omega^{KS}$ (SP) underestimate the $\omega_I$ by $\leq 2\%$ as summarised in Table 8.1. The oscillator strengths are about one third larger. Beside the physical relevance, the computation time can be reduced drastically especially in the case of very large structures, since the most time-consuming diagonalisation of a response matrix is circumvented.[¶]

## 8.3 Optical properties of nanoparticles with complete and no surface saturation

Corresponding to Chapter 7, we have now calculated the optical absorption spectra with the linear-response scheme. The obtained singlet-excitation spectra are summarised in Fig-

[§]The corresponding eigenvalue spectra of $[Cd_{32}S_{14}(SR)_{36}]^0$ and $[Cd_{54}S_{32}(SR)_{48}]^{4-}$ are shown in Figure 8.1.

[¶]cf. Section 3.8.3

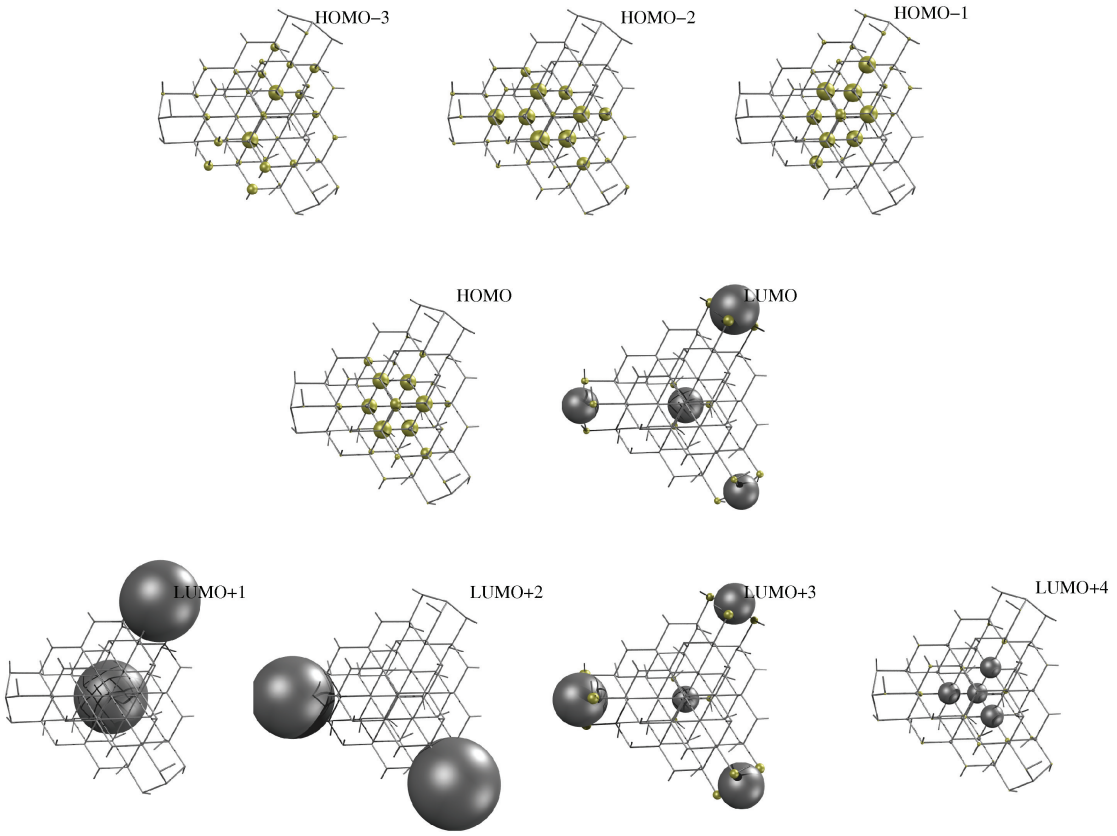


Figure 8.4: *Frontier orbitals of* $[Cd_{32}S_{14}(SR)_{36}]^0$ *with saturation defect: The four missing ligands at the vertices cause dangling bonds which affect the optical properties. These are discussed in Section 8.4). More information in the structures are given in Table 8.1 and the corresponding optical excitation spectrum in Figure 8.2. The SCF-DFTB MO energies are depicted in Figure 8.1. For better depiction the MO's (SCF-DFTB) are approximated by the projected atomic contributions (sulphur yellow; cadmium grey colour) to the orbital (*Mulliken-*population analysis) represented as spheres centred at the corresponding atom.*

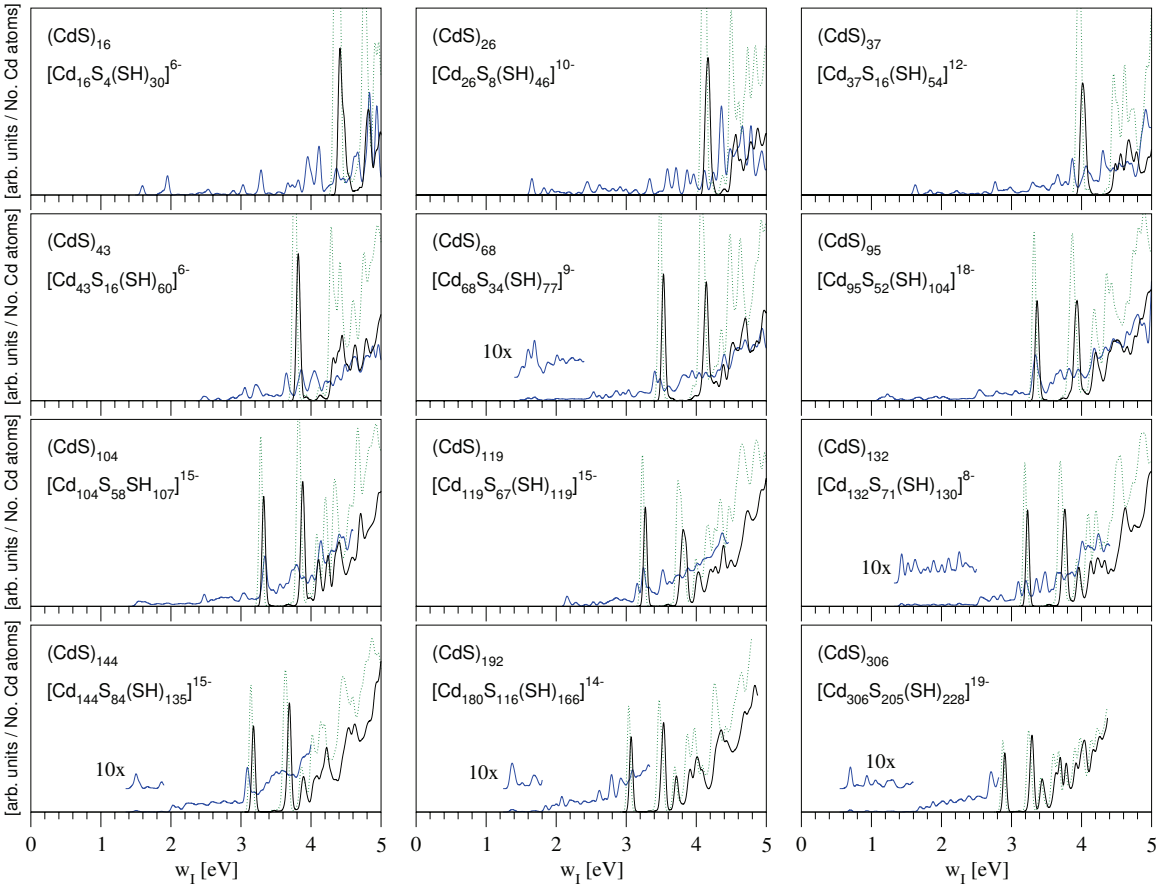


Figure 8.5: *Calculated linear-response singlet-excitation spectra ($\omega_I$) of bare (blue curves) and completely surface-saturated (black curves) zinc blende derived, spherical CdS nanoparticles within the size range of $r = 0.5 - 1.5nm$. The dotted curves correspond to the single-particle spectra ($\omega^{KS}$). The corresponding eigenvalue spectra of the states closest to the Fermi level are depicted in Figure 7.3. Further details on the structures and the computation are given in Section 8.1.*

ure 8.5: Instead of depending on the particle size, the onset excitation energies of the unsaturated nanoparticles show irregular fluctuations, and thus do not follow the QCE. This is caused by excitations involving the surface states. Their excitation energies are below the experimental bulk band gap (2.58eV [11]), as well as for the corresponding saturated nanoparticles [135]. The oscillator strength of those low-lying excitations are very weak, but increase with the number of unsaturated Cd atoms.

These results are in agreement to *Joswig et al.*, who used similar structures to calculate the optical properties with the $\gamma$-approximation scheme [171]. They stressed that these low-lying excitations have a collective character, as observed experimentally in metal clusters as surface plasmon excitations [177] or an exciton, which is a common excitation in direct band-gap semiconductors. The differences between the excitation energies in this work and in Ref. [171] can be addressed to the different methods that are used to determine the electronic ground-state properties.[‖] However, the resulting picture is qualitatively the same: Thus, a large number of excitations is located at smaller energies than the lowest one of the corresponding bulk structure. Moreover, these low-lying excitations in the spectra, but also excitations at higher energies, exhibit rather weak oscillator strengths. Hence an evidence for a plasmon- or an exciton-like character is not given.

Continuing the study with the same, but completely surface-saturated structures, the principle features are reproduced, that were obtained for the test set (cf. previous section). The calculated excitation spectra are given in Figure 8.5. The energy of the onset excitation is located above the corresponding value of the bulk and is decaying toward it, which is shown in Figure 8.12 and will be discussed later. Furthermore, over the large size-range all spectra have exhibit the excitonic onset peak with large oscillator strength. The transition is of $s-s$ type, which corresponds with that of the test set of small nanoparticles.

Additionally, a second excitonic absorption peak of similar oscillator strength occurs in the direct neighbourhood of the onset peak at higher energies. This is not observed as a feature of the smaller structures, but rather becomes characteristic for a particle radius larger than 1nm. This transition is mainly of $p-p$ type. Similar to the first excitonic excitation, this second has the following contributions: The hole wavefunction consist mainly of the up to fivefold degenerated HOMO$-i$ with $i = 3, 4, 5, 6, (7)$ and the electron wavefunction of the threefold degenerated LUMO$+j$ with $j = 1, 2, 3$. The wavefunctions of these MO's have a symmetry corresponding to a hydrogen $1p$ function.

In contrast to the onset excitation, this second one has also minor contributions from transitions which are collectively excited. These originate form occupied MO's with lower energy to the LUMO (cf. Figure 8.6). Moreover, this intermixing has a relevant contribution to the absorption. With an increase of the excitation energy the corresponding oscillator strength of these higher-lying transitions is also increasing. It further increases with the

[‖]Herein SCF-DFTB is used. In contrast, Ref. [171] uses standard DFTB which results in orbital energies, that are about twice as large as the energy values obtained in this work (cf. Section 7.2.3).

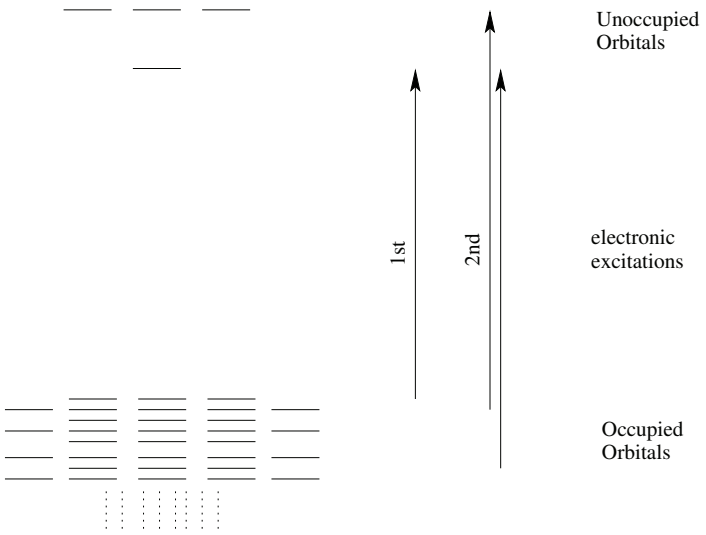


Figure 8.6: *Scheme of the electronic excitation: Discretisation of the excitation spectra in semiconductor nanoparticles (saturated CdS) due to the confinement of the unoccupied orbitals (QCE).*

particle size. This effect is due to the increasing density of the electronic states (forming band a in the bulk limit). Further, this intermixing of several single transitions at higher energies does not allow any assignment of further angular moments.

In summary, the observed discretisation of the excitonic absorption peaks in the calculated spectra is directly related to the QCE. For lower particle sizes ($r \leq 1$nm) only the angular moment $s$ of the MO wavefunction is observed, whereas, larger structures seem to allow also higher values. This angular momentum series up to $p$ is shown for CdS nanoparticles in Figures B.5, 8.7 and 8.11 for different sizes and shapes of the structures.

A similar behaviour is known from the *Jellium*-model for metal clusters [145], which can be interpreted in the sense of molecular orbital theory [178, 179]. However, for semiconductors the confinement affects mainly the unoccupied orbitals. Thus, the absence of "magic numbers" for certain stable cluster or nanoparticle structures is obvious.

### 8.3.1 Underlying structure

It has been shown in the previous chapter, that nanoparticles derived from the zinc blende and wurtzite modification isomorphs exhibit almost identical electronic properties. The impact of the structure on the optical properties of these structures is now studied in the following.

The calculated singlet-excitation spectra of particles with wurtzite structure are shown in Figure 8.8. Qualitatively, they are rather similar to that of the zinc blende structures in Figure 8.5. The differences are marginal: For the wurtzite type structures the onset excitation

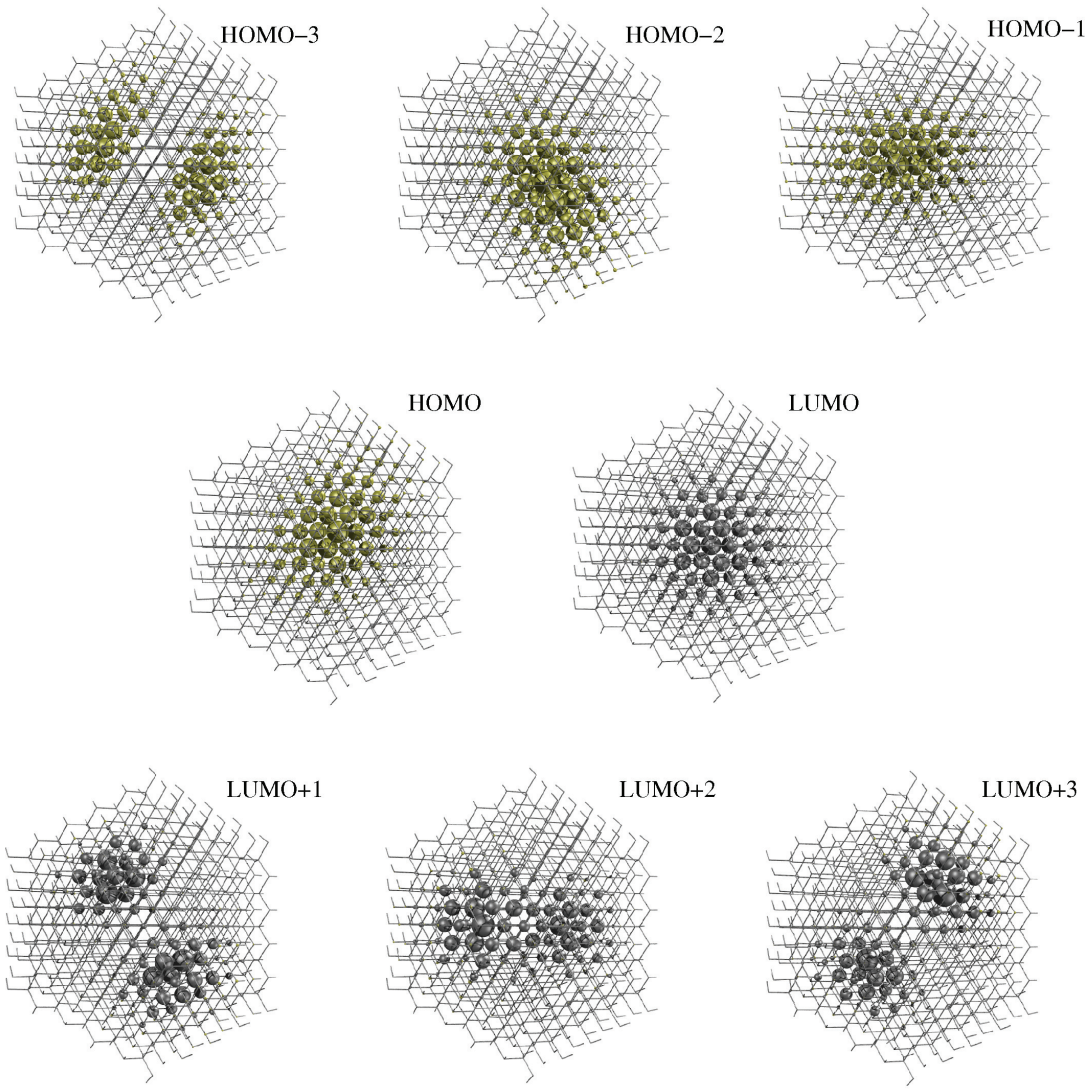


Figure 8.7: *Frontier orbitals in a cuboctahedral confinement: The electronic wavefunctions of the MO's closest to the Fermi level show a spatial angular momentum splitting, which is shown exemplarily for* $[Cd_{309}S_{216}(SH_{204})]^{18-}$. *For better depiction the MO's (SCF-DFTB) are approximated by the projected atomic contributions, represented as spheres centred at the corresponding atom (sulphur yellow; cadmium grey colour). The corresponding eigenvalue spectrum is given in Figure 7.5 and the optical excitation spectrum in Figure 8.10. Additional details of computation are given in Section 8.1.*

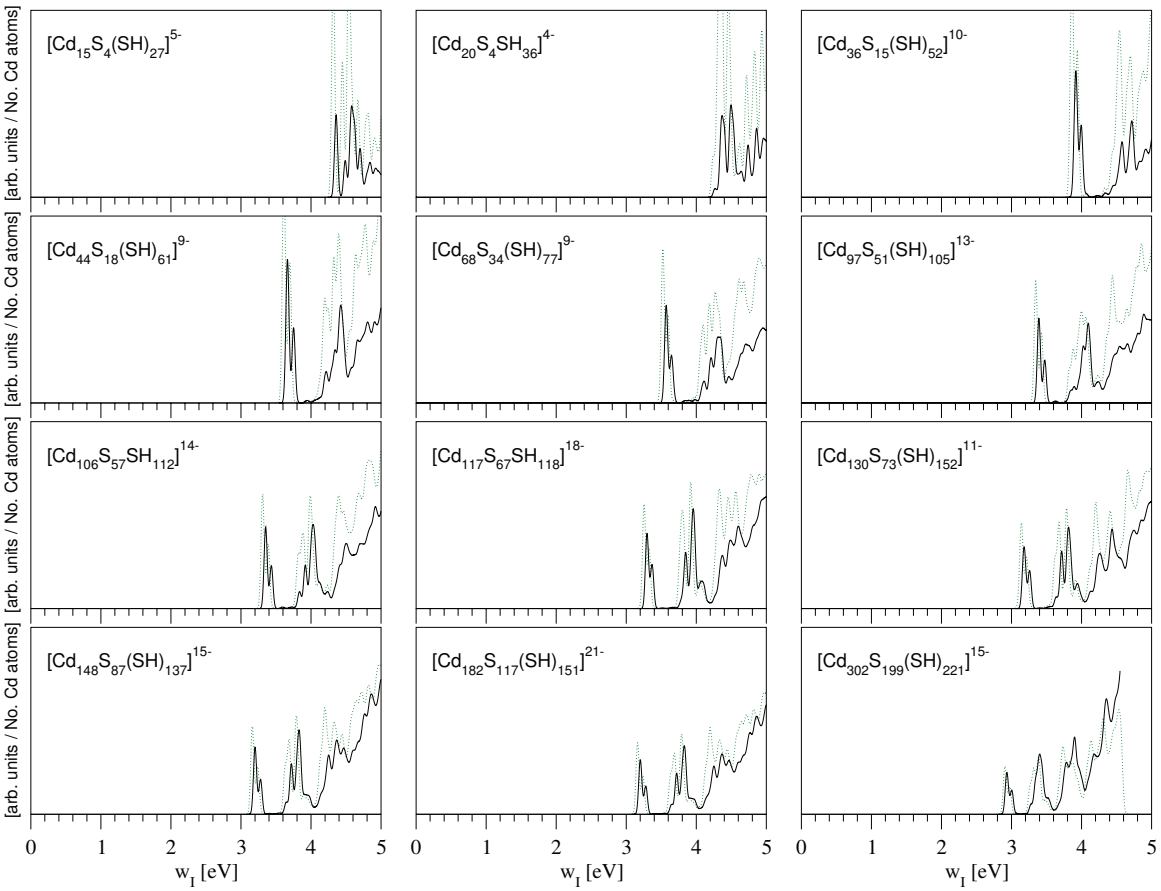


Figure 8.8: *Calculated linear-response singlet-excitation spectra ($\omega_I$) of completely surface-saturated (black curves) wurtzite derived, spherical CdS nanoparticles within the size range of $r = 0.5 - 1.5nm$. The dotted curves correspond to the single-particle spectra ($\omega^{KS}$). Further details on the structures and the computation are given in Section 8.1.*

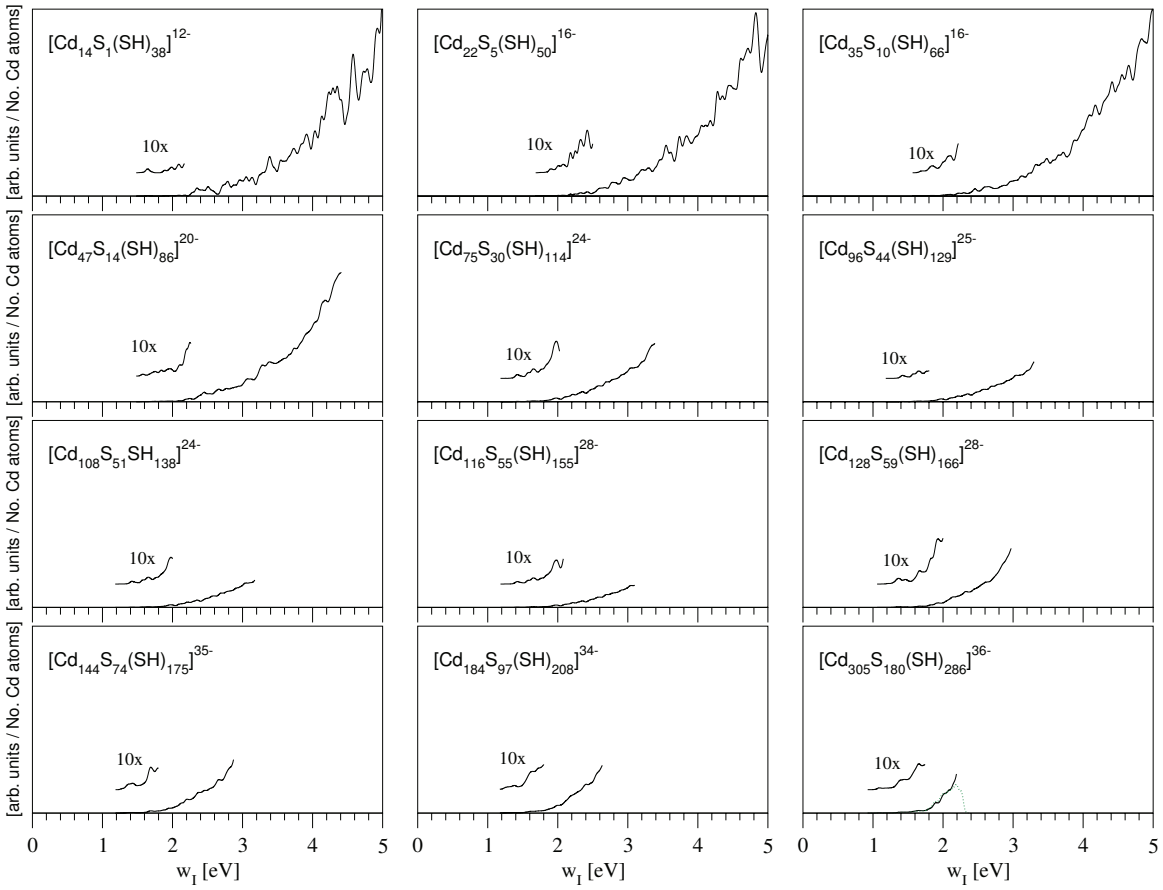


Figure 8.9: *Calculated linear-response singlet-excitation spectra ($\omega_I$) of completely surface-saturated (black curves) rock salt derived, spherical CdS nanoparticles within the size range of $r = 0.5 - 1.5nm$. The dotted curves (exemplarily shown in the lower right panel) correspond to the single-particle spectra ($\omega^{KS}$), which for the saturated structures are identical to the $\omega_I$. Further details on the structures and the computation are given in Section 8.1.*

is a double peak with a splitting smaller than 0.1eV. It is caused by the lowered symmetry of the wurtzite structure, which reduce the degeneracy of the HOMO. Respectively, this feature continues in the spectra also for the second and higher excitonic absorption peaks compared to the zinc blende phase.

However, the characteristics of the optical property of the semiconductor changes completely, when the underlying structure is transformed to the rock salt modification [22, 173, 174]. Figure 8.9 shows the calculated spectra of completely saturated spherical nanoparticles with this crystal structure. According to the experiment, their spectra look typical for an indirect semiconductor: The oscillator strength of the lower excitations is reduced for some orders of magnitude. The single excitations are close in energy, that effectively a continuous, featureless spectrum arises. Thus, no excitonic peak is observed. However, the onset excitation energies of the nanoparticles with compete saturated surface decrease with increasing particle size and, thus, following the QCE.

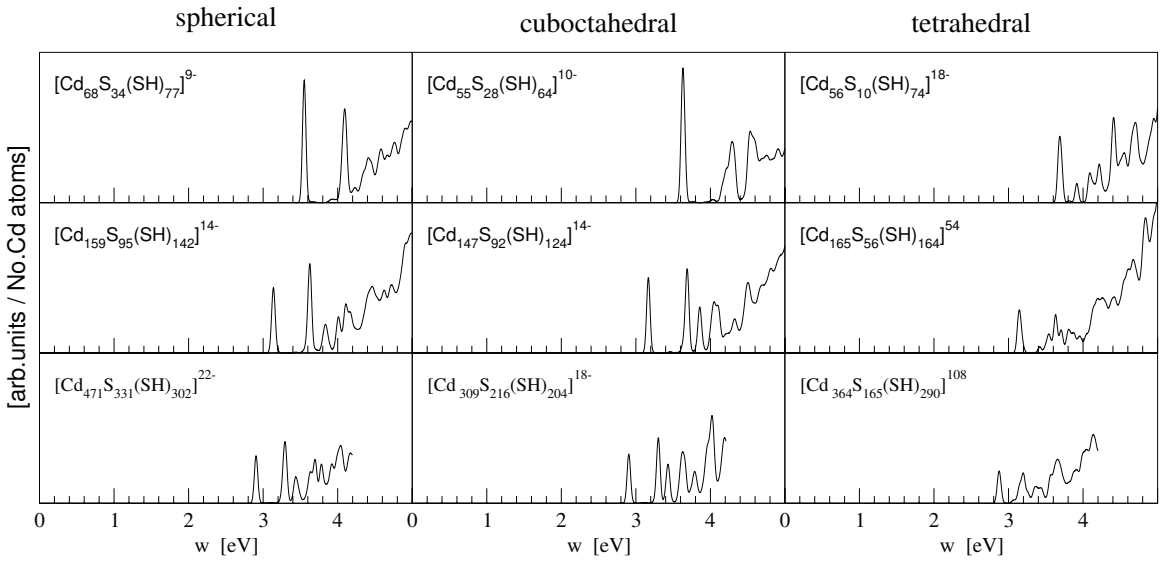


Figure 8.10: *Calculated linear-response singlet-excitation spectra of surface-saturated CdS nanoparticles with a different shape and size: spherical (left column), cuboctahedral (middle column) and tetrahedral (right column). The underlying structure of the particles is of zinc blende type. Further computational details are given in Section 8.1.*

### 8.3.2 Influence of the particle shape

The results of the previous sections have shown that in a spherical confinement the wave functions of the orbitals closest to the *Fermi*-level feature the hydrogen angular momenta. Since a different confinement may influence the optical properties of the nanoparticles the influence of their shape is investigated below.

In Figure 8.10 the calculated excitation spectra of completely surface-saturated CdS nanoparticles are shown, which have spherical, tetrahedral and cuboctahedral geometries and zinc blende structure: In general, all optical properties, that have been found for the spherical geometries are reproduced for the other two shapes. The spectra of spherical and cuboctahedral nanoparticles are almost identical, since their structures have only minor differences. These are more pronounced for the smaller nanoparticles. While the spherical structures are centred at a Cd-S NN bond, the cuboctahedral (and tetrahedral) ones have a Cd atom at the central position.** However, for particles with a similar number of Cd atoms and respectively volume the shape has no influence on the onset excitation energy (cf. Figure 8.12). Moreover, this holds also for the higher excitations in the spectra.

Furthermore, the strong oscillator strengths of tetrahedral structures is about half as high as that of the spherical and cuboctahedral ones. This is independent from the size of the particle, but is directly coupled to the shape. Clear from Figure 8.11, confinement in

**cf. Section 6.1.2

the tetrahedral environment is different and the effective overlap between electron and hole wavefunctions is smaller.

### 8.3.3 QCE of the onset excitation

In Figure 8.12 the lowest excitation energies of the CdS nanoparticles are summarised with respect to the particle size. The calculated values are contrasted with experimental data, which have been obtained for small (cf. Section 8.2) and larger [135, 136] sized particles: In general, these curves are well reproduced by the computed values. When extrapolating the particle size toward the bulk limit, the experimentally observed asymptotic decay toward the lowest absorption energy of the bulk is also reproduced. The calculated values underestimate the experimental ones by 10%, which is mainly due to the LDA overbinding effect. Further reasons for the deviation have been discussed in Section 8.2.

However, without this systematic error the calculated lowest excitation energies would fit to the experimental values, which correspond to the alkylthiol saturated nanoparticles (cf. Figure 8.12). The deviation for thiophenol saturated clusters can be addressed to the direct incorporation of these ligands in the optical processes of the onset excitation [180, 141].

Moreover, clear from Figures 8.5, 8.8 and 8.9 the single-particle scheme represents an alternative for the computation of the excitation spectra. Especially the onset excitation are reproduced compared to the $\gamma-$approximation ($\omega^I$). While for the small clusters these values are underestimated by 2%, with increasing particle size of the particles this error is decaying. This result is in agreement with TD-LDA investigations of CdSe particles [155]. Thus, for large nanoparticles the single-particle approach allows the efficient, as well as, accurate computation of the excitation spectra compared to linear response schemes (TD-DFRT).

## 8.4 Impact of dangling bonds on the optical properties

The investigation of the structural properties in Section 6.3.3 has been shown, that the charge q as well as the presence of dangling bonds is of crucial relevance for the local stabilisation of the surface of the nanoparticles.

In a first investigation the importance of q for the optical properties is highlighted: The optical excitation spectra of two sets of completely saturated CdS nanoparticles $[Cd_mS_n(SH)_i]^q$, one with q=2(m−n)−i and the other with q=0, and 2(m−n)−i≠0 are calculated using the $\gamma$-approximation. The obtained singlet-excitation spectra are depicted in Figure 8.13. Only for the structures with q=2(m−n)−i characteristic spectra are obtained. The structures with q=0, for 2(m−n)−i≠0 have numerous excitations at very low energies with large oscillator strengths. For excitation energies, which are higher than the onset excitation of the charged structures, the spectra similarly continue.

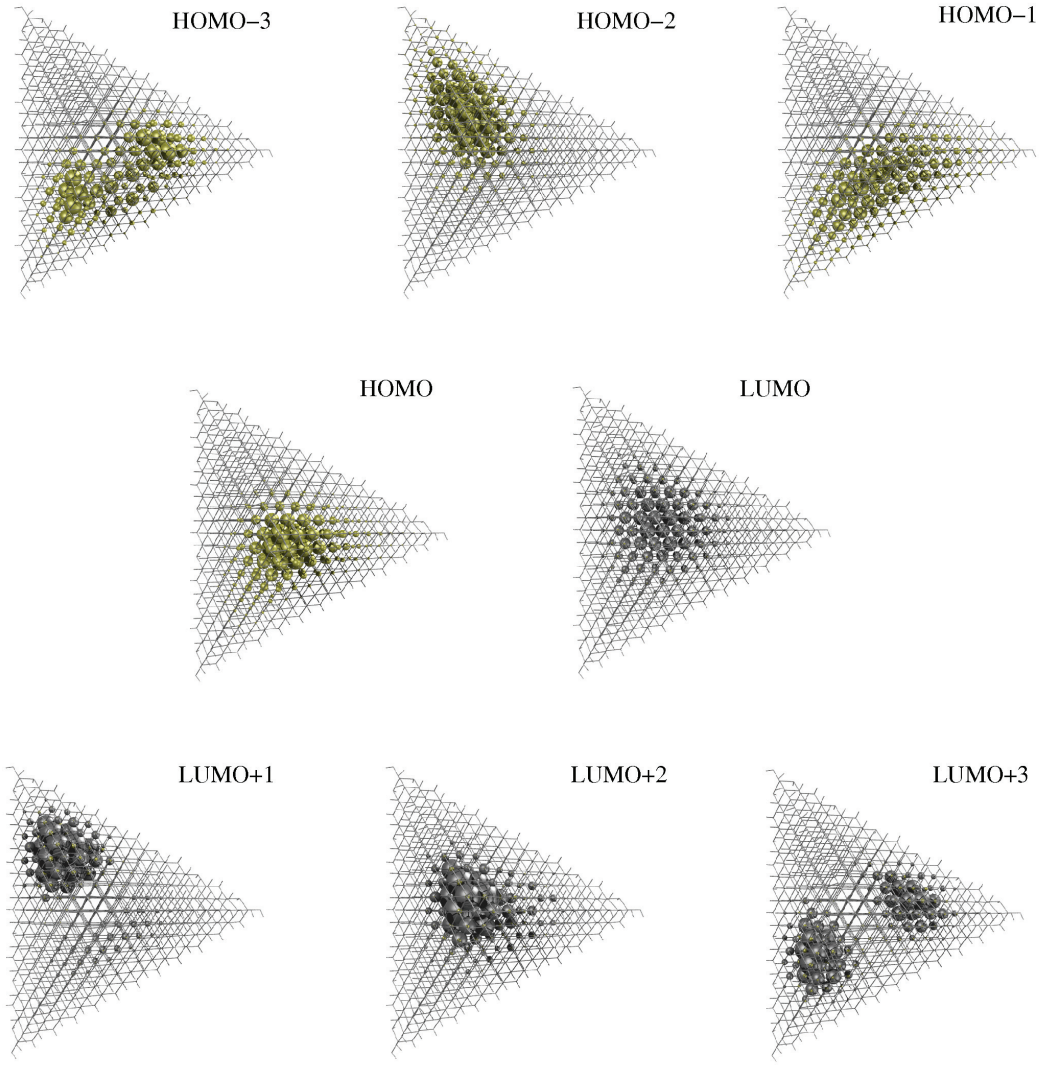


Figure 8.11: *Frontier orbitals in a tetrahedral confinement: The electronic wavefunctions at of the MO's closest to the Fermi level show a spatial angular momentum splitting, which is shown for* $[Cd_{364}S_{290}(SH_{290})]^{108+}$. *For better depiction the MO's (SCF-DFTB) are approximated by the projected atomic contributions, represented as spheres centred at the corresponding atom (sulphur yellow; cadmium grey colour). The optical excitation spectrum is given in Figure 8.10. Additional details of computation are given in Section 8.1.*

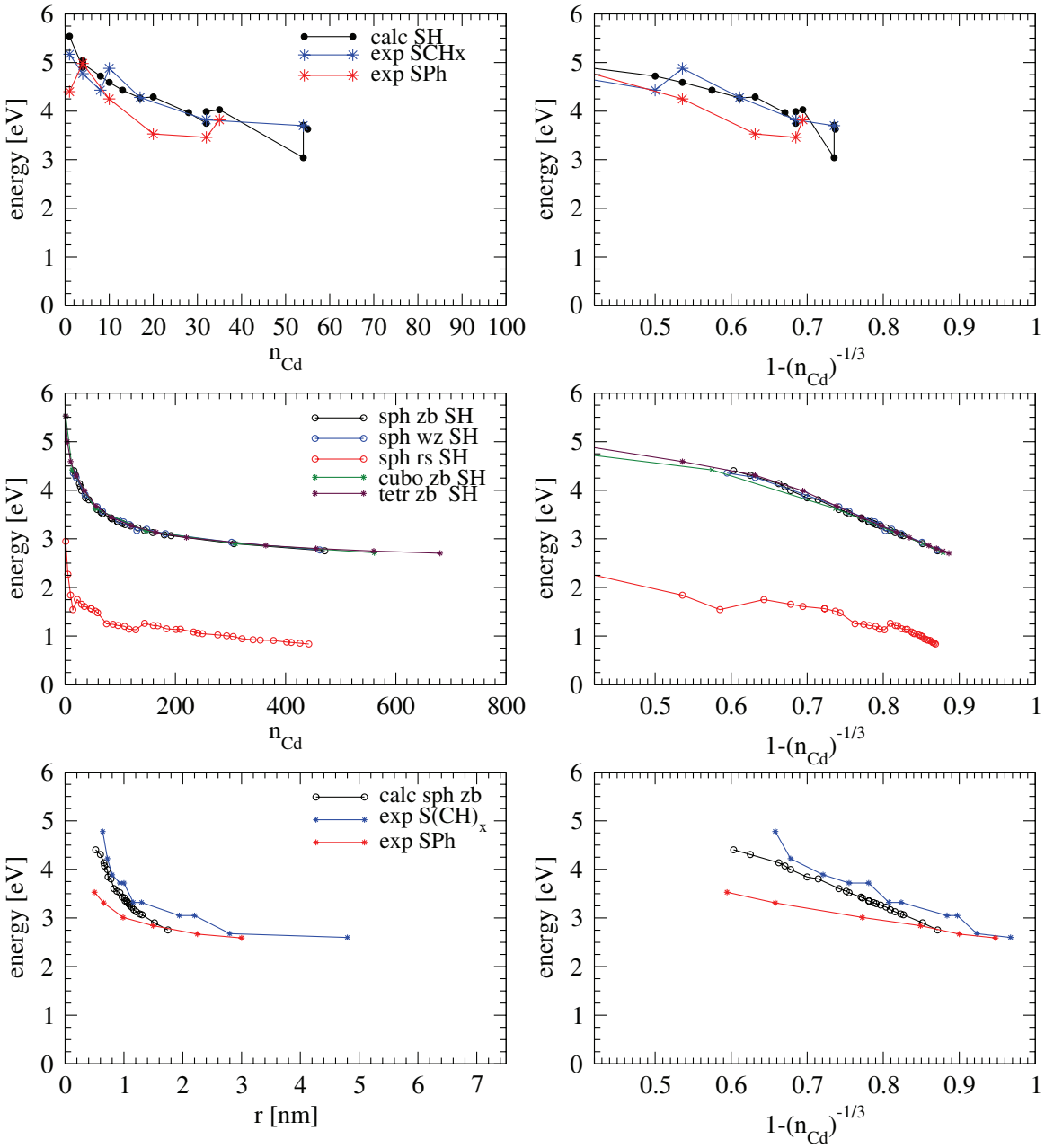


Figure 8.12: *Size dependence of the lowest excitations of* $[Cd_mS_n(SR)_i]^q$ *nanoparticles with respect their surface saturation: Upper panels: Calculated and experimental values of small nanoparticles (cf. Table 8.1). Middle panels: Calculated values of spherical (sph), cuboctahedral (cubo) and tetrahedral (tetr) shaped nanoparticles, as well as, zinc blende (zb), wurtzite (wz) and rock salt (rs) type structure. Lower panels: Comparison of the calculated to experimental values of comparable nanoparticles structures with different saturation (SPh [135] and* $SCH_x$ *[136]). The abbreviations in the legends denote the following: SH R=H atom, SPh R=Phenyl and* $SCH_x$ *R=Alkyl. Further details the computation cf. Section 8.1.*

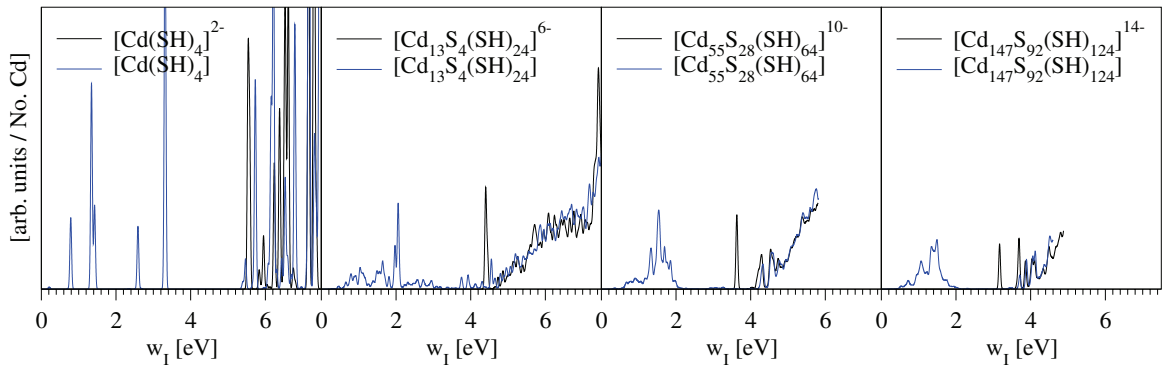


Figure 8.13: *Impact of the compensating charge q on the optical properties: Calculated linear-response singlet-excitation spectra of completely surface-saturated CdS nanoparticles with cuboctahedral shape. The black curves denote to structures* $[Cd_mS_n(SH)_i]^q$ *with q=2(m−n)−i while blue curves to nanoparticles with q=0. Further computational details are given in Section 8.1.*

Furthermore, in a second investigation the impact of single dangling bonds is highlighted. Therefore, single surfactants are removed explicitly from distinct positions at the surface of the nanoparticle $[Cd_{147}S_{92}(SH_{124})]^{14-}$: ††

a) Missing one ligand R at $(\cdots Cd)_1-S-R$ causing a dangling bond $(\cdots Cd)_1-S$

b) Missing one ligand R at $(\cdots Cd)_2=S-R$ causing a dangling bond $(\cdots Cd)_2=S$

c) Missing one ligand R at $(\cdots Cd)_3\equiv S-R$ causing a dangling bond $(\cdots Cd)_3\equiv S$

d) Missing one ligand S-R at $(\cdots S)_3\equiv Cd-SR$ causing a dangling bond $(\cdots S)_3\equiv Cd$.

The calculated singlet-excitation spectra are depicted in Figure 8.14. For spectra of the structures with dangling bonds at a S atom (a,b and c) the result is in complete agreement to that of the completely saturated nanoparticles (cf. Figure 8.13).

In contrast, for the nanoparticles with a dangling bond at a Cd atom (d) the impact on the optical properties is larger. Despite the consideration of q, a sub-band gap state is created, which in the absorption spectra causes an excitation slightly below the onset excitations with weak oscillator strength. According to the participation analysis of the MO's close to the *Fermi* energy, the sub-band-gap state is located at exactly the introduced saturation defect (cf. Figure 8.15. The next higher states show again the characteristic spatial delocalisation, as well as the angular moment dependence of the electronic wavefunction. However, the LUMO+1, which corresponds to the electron wavefunction in the first excitonic absorption, has also large contributions from the surface defect. Thus, the oscillator strength of all excitonic absorptions is reduced by approximately 20%, by this single saturation defect.

††For the herein used nomenclature cf. Section 6.1.

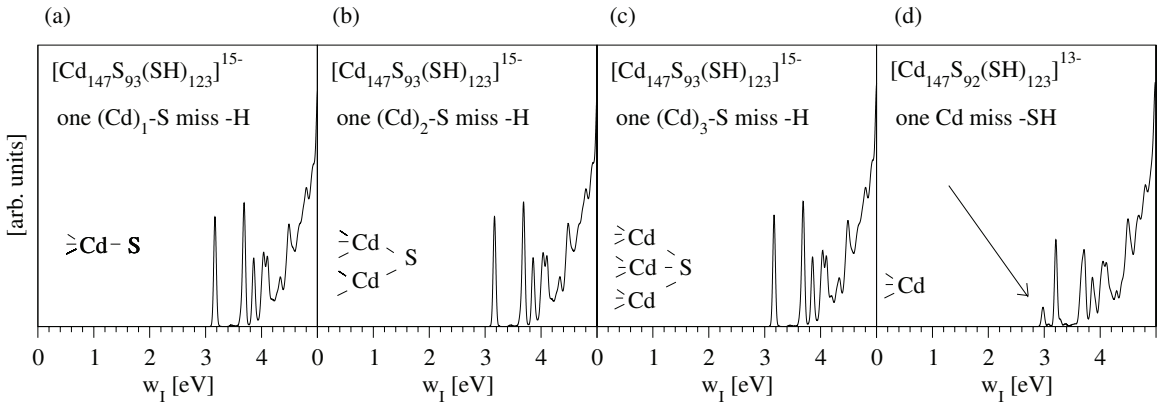


Figure 8.14: *Impact of a single defect in the saturation on the optical excitation spectra: Calculated linear-response singlet-excitation spectra of surface-saturated CdS nanoparticles with cuboctahedral shape. The numbering of the panels (a,b,c and d) refers to items in Section 8.4. Further computational details are given in Section 8.1.*

Similarly, results are found for the small tetrahedral shaped nanoparticles, which have been investigated in Section 8.2. These miss each the four surfactants (corresponding (d)) at the vertices, as well as, further ligands at the faces of the tetrahedron (corresponding to (c)). Hence, in general only dangling bonds at the Cd atoms influence the optical absorption properties.

Alternatively, the experimental results of *Lifshitz et al.* [175, 176] on the excitation relaxation processes for CdSe systems suggest the presence of a sub-band-gap state with a clear dependence on the nanoparticle structure. The authors argue that the recombination takes place at a low-symmetry site, such as one near the surface, and, furthermore, that the hole is delocalised, whereas the electron is localised at the surface. Accordingly, *Bawendi et al.* [103] observed by optical hole burning and photoluminescence measurements that the band-edge luminescence is from a surface-trapped state and not from the exciton state. These experimental observations are in agreement with the results of the present work.

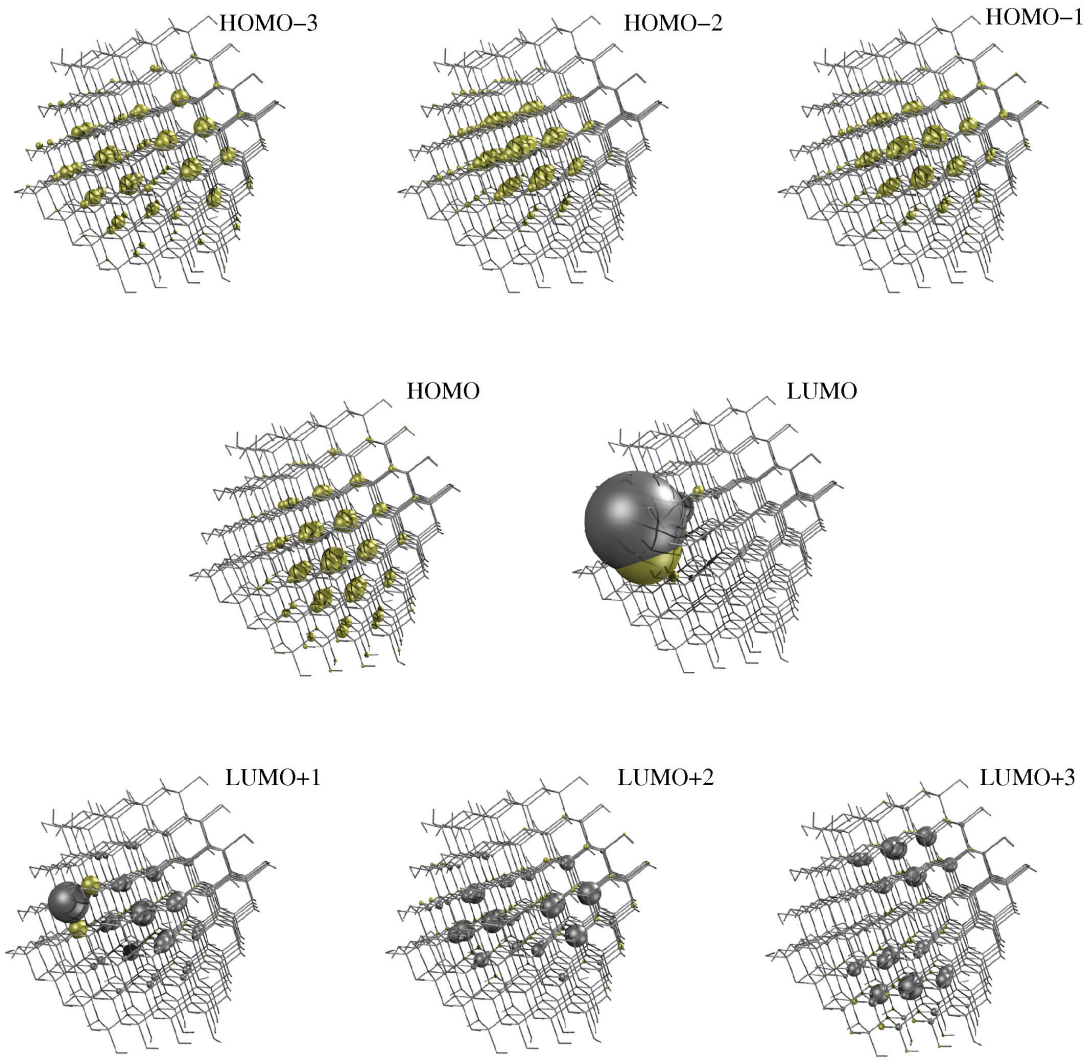


Figure 8.15: *Frontier orbitals with a localised surface state (dangling bond): CdS cuboctahedral nanoparticle* $[Cd_{147}S_{92}(SH_{123})]^{13-}$*, which is missing a single* $-SH$ *at a Cd atom. For better depiction the MO's (SCF-DFTB) are approximated by the projected atomic contributions, represented as spheres centred at the corresponding atom (sulphur yellow; cadmium grey colour). The corresponding optical excitation spectra is given in Figure 8.9.*

# 9 Organised structures of CdS nanoparticles

After the discussion of the properties of single CdS semiconductor nanoparticles, we will focus now on the effects due to their organisation. Nanocrystals are potential candidates for application as building blocks in electronic and optical devices. Thus, solvent-free particles (i. e., particles in a non-liquid phase), either deposited on a substrate or incorporated into a solid phase, are advantageous to obtain adequate material handling. Some effort has been made to organise semiconductor nanoparticles [181, 182, 183, 184, 185, 186]: *Weller* and co-workers have synthesised tetrahedral $Cd_mS_n$ nanoparticles organised in a tetragonal super-structure [119, 120, 187, 188]. Their building-block structures are similar to those reported previously [117, 118], but owe different organic ligands for stabilisation. The stoichiometries within the super-network are $Cd_{17}S_4(SCH_2CH_2OH)_{26}$ and $Cd_{32}S_{14}[SCH_2CH(CH_3)OH]_{36}$. Their non-saturated counterparts are $Cd_{17}S_{32}$ and $Cd_{32}S_{50}$. The corresponding structures of single clusters have been investigated in this work (cf. Section 8.2). These nanoparticles have a tetragonal shape and are connected by shared corner atoms to form a three-dimensional network with a diamond-like super structure. Both, the single tetrahedron and the unit cell of the superstructure are depicted in Figure 9.1 for $Cd_{17}S_{32}$ exemplarily.

## 9.1 Details of the calculations

The structures of the single clusters and those of the superstructures are relaxed in their geometries with MD simulations. Using the standard DFTB scheme the MD simulation is carried out in an NVT ensemble with the following options: MD temperature $T = 0$ K, which is controlled by a *Berendsen* thermostat [154] applied to each atom independently, and a MD time step $\Delta t = 2$ fs. Thus, the final maximal gradient has a value below $10^{-4}$ Ha/Bohr.

The electronic structure is calculated with the own SCF-DFTB scheme. The corresponding details of these calculation are given in Sections 5.2.2 and 7.1.

## 9.2 Structural properties

From the performed calculations on saturated and unsaturated tetrahedral CdS clusters, both in the gas phase and in the tetragonal superstructure the following results have been obtained: In the singly unsaturated clusters, strong deformations are observed, which are caused by the structural relaxation. However, less charge-transfer within the single cluster is observed when saturating the dangling bonds at the surface with hydrogen atoms and,

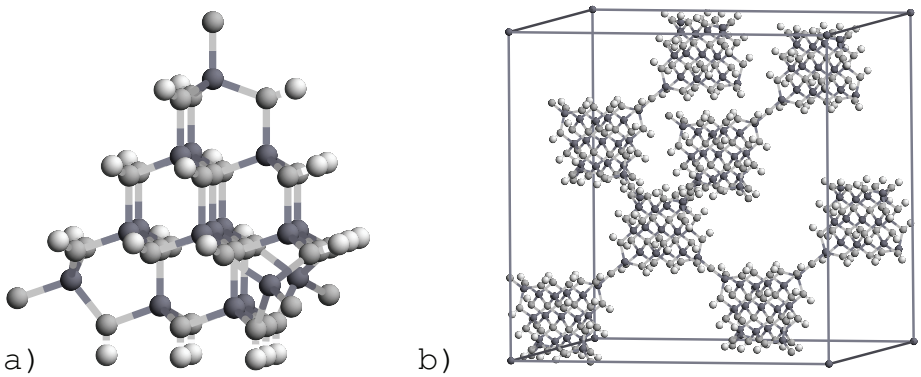


Figure 9.1: *a) Single building block* $[Cd_{17}S_4(SH)_{26}]$ *and b) the arrangement of eighth single clusters as periodic super-structure* $[Cd_{17}S_4(SH)_{26}]^{3d}_{\infty}$ *in a unit cell. Cd and S are shown as dark grey and light grey, respectively. The ligands are approximated by H atoms which are represented by white spheres.*

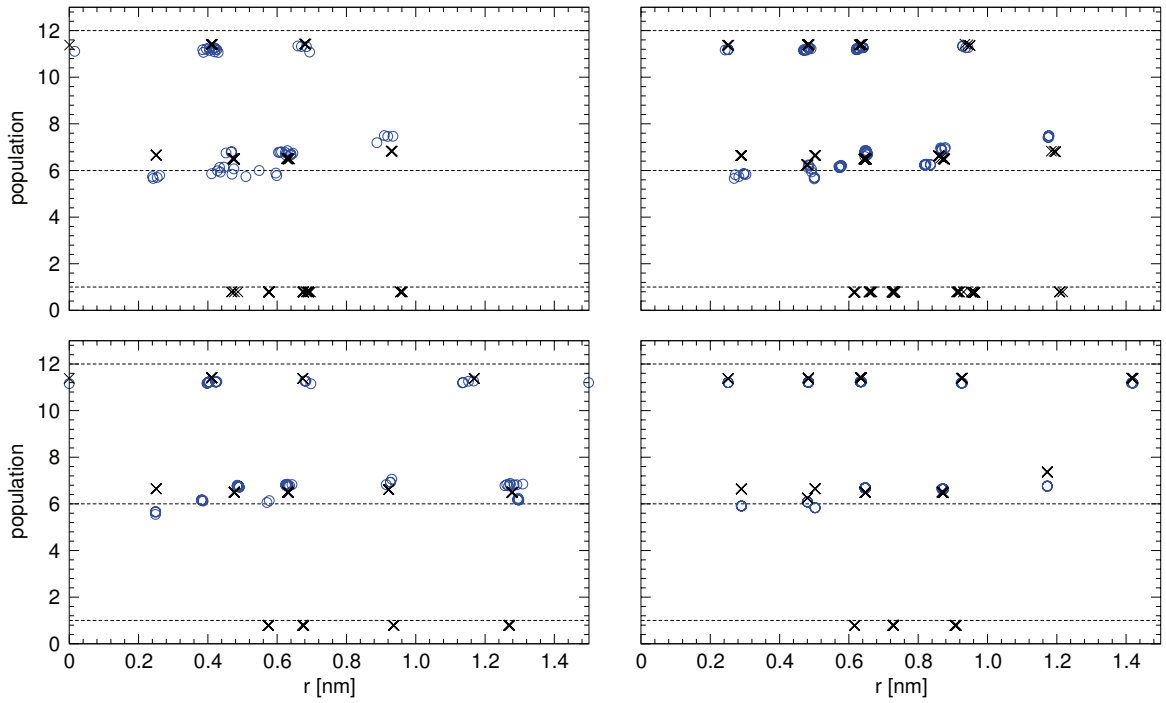


Figure 9.2: *Radial distribution of the Mulliken gross population:* $Cd_{17}S_{32}$ *and* $[Cd_{17}S_4(SH)_{28}]^{2-}$ *[(a) single tetrahedron, (c) periodic structure], and* $Cd_{32}S_{54}$ *and* $[Cd_{32}S_{14}(SH)_{40}]^{2-}$ *[(b) single tetrahedron, (d) periodic structure]. Open circles and crosses mark atoms in the unsaturated and the saturated clusters, respectively. The dashed lines mark the number of valence electrons of the single atoms in Cd (12), S (6) and H (1).*

moreover, the structural relaxations are marginal with respect to the initial (experimentally characterised) clusters. These results are in agreement to those obtained in this work (cf. previous Chapters 6 and 7).

## 9.3 Electronic Properties

The electronic properties of the investigated clusters show a strong dependence on saturation. For example those are given by the Mulliken gross populations in Figure 9.2. An influence of the periodic arrangement on the properties could, however, hardly be observed: The Mulliken populations, but also the electronic DOS (cf. Figure 9.3) are very similar for the single clusters and for the periodic structure. However, in detail for the single non-saturated clusters have no mid- or sub-band-gap states, which vanish when these non-saturated structures are arranged in periodic superstructures. However, their *Fermi* level is not located in the band gap, but at lower energies in the S $3p$ band. If the surface is completely saturated the electronic DOS of cluster and superstructure have a band-gap without defect-states. The *Fermi* level is in the middle of the gap. Moreover, for all periodic struc-

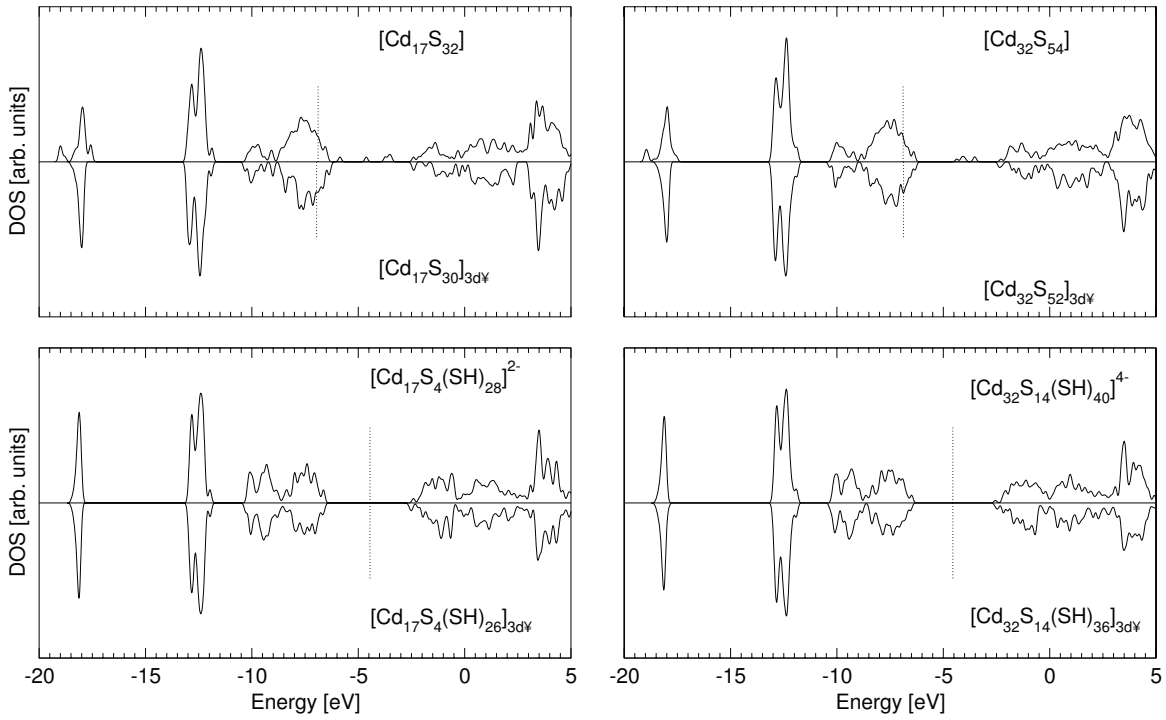


Figure 9.3: *Electronic DOS of the tetrahedral nanoparticles* $[Cd_{17}S_{32}$ *(left column) and* $[Cd_{32}S_{54}$ *(right column). The upper panels show the electronic DOS for the bare clusters. The lower panels show it for those ones that are surface-saturated (R=H). In each panel the curve pointing upward refers to the isolated nanoparticles, whereas the curve pointing downward refers to the periodic super-structures. The dashed line mark the* Fermi *level.*

tures the corresponding bandstructures have been calculated. These show no dispersion of the electronic bands and therefore the banstructure is not presented.

Nevertheless, the surfactants itself are stabilised in the cavity, which is due to their dense packing and covalent linking. Likewise, the organisation of such nanoparticles in *Langmuir-Blodgett* films or their embedding in a polymer matrix strongly influences an ordering or fixation of the ligands. In all cases, the reproducibility of the surface structure of single nanoparticles is increased. Thus, the surface structure is mainly affecting the electronic and optical properties of single nanoparticles, rather than those of the superstructure. This is in agreement to the results of this work (cf. Sections 7 and 8).

# 10 Summary and Conclusion

In this work, the structural, electronic, and optical properties of CdS nanoparticles with sizes up to 4 nm have been calculated. In particular the effects of surface saturation have been studied. To overcome inaccuracies in the description of the unoccupied states by the applied DFTB method, the new SCF-DFTBmethod has been developed.

In the context of this work the DFTB part of the `deMon` DFT code has been extended with the implementation of the routines for the calculation of optical properties in the $\gamma$-approximation and the orbital and atom resolved population analysis (pDOS).

In SCF-DFTB, methodological problems of the charge-transfer description of the standard DFTB scheme are corrected. For this purpose, two-centre contributions are treated self-consistently for the specific electronic system. The onsite contributions are described by free, neutral atoms. Thus, the new SCF-DFTB method represents a systematic improvement of DFTB towards SCF-DFT and, therefore, provides further validation of the DFTB approximations. Hence, it confirms the physical picture, that electronic systems, i. e., molecules and bulk, are in the first instance composed of atoms. The description of covalent binding is already achieved by the two centre interactions, which cover the spatial region in-between the atoms, that is, where chemical bonds are located. If these interactions are treated correctly the electronic structure is described to a large extent.

Calculation of the electronic structure of the unoccupied states of CdS demonstrate the capabilities of the new SCF-DFTB method: As the charge transfer phenomena are described correctly, the SCF-DFTB band structures are in almost quantitative agreement with the full potential SCF-DFT level. However, the introduction of a SCF scheme causes an enormous increase of computing time, which is in the magnitude of SCF-DFT. To improve the computational efficiency, an approximate SCF-DFTB scheme has been developed and tested. It provides the same efficiency as the standard DFTB and is absolutely necessary for studying large semiconductor structures.

A further result of this work was a development of a recipe to generate model structures of CdS nanoparticles. For this task, a saturation scheme of the nanoparticles surface has been developed which respects experimental observations. This scheme has been implemented in a computer algorithm. It allows the creation and saturation of semiconductor nanoparticles structures by cutting out distinct fragments of the corresponding solid structure. The nanoparticles can be selected by specification of different crystal structures, sizes, shapes and saturation patterns. This is important as the shape of the particle as well as its crystal structure influences the optical properties.

For the correct treatment of properties of CdS nanoparticles it has been shown that not only a complete saturation of the surface atoms, but also their charge is important for structural stabilisation, especially for the surface atoms. These results have been validated by reference calculations on experimentally determined structures.

The calculations of electronic structure and linear-response excitation spectra of these nanoparticles show that they depend to a large extent on the way their surfaces are saturated. As the nanoparticles can be modelled now correctly, the theoretical results agree for the quantum size effect (QSE), in particular for HOMO-LUMO gap energies and the lowest excitation energies, with experiment and with high-level reference calculations.

The very good agreement between theory and experiment holds also for the impact of surface saturation and charge $q$ to the electronic states at the *Fermi* level. For these states, an angular dependence of the MO wavefunctions have been obtained. HOMO$-i$ with $i = 0, 1, 2$ and LUMO are of $s$ character, even for the smallest structures. Higher angular momenta have been obtained for larger particles. Thus, through this spatial overlap of hole and electron wavefunction the onset excitation ($s$-$s$) and for larger structures the excitations with the next higher energies ($p$-$p$) are excitonic.

The investigations of partial saturation and single dangling bonds have demonstrated that already one missing surfactant has a strong influence on the electronic structure of the states closest to the *Fermi* level. A change of the saturation of the surface is crucial for the electronic structure and, thus, optical processes. It has been shown that already a single dangling bond at a Cd atom causes a sub-band gap state which is located at this atom. This dangling bond not only reduces the oscillator strengths in the complete absorption spectra, but also introduces additional, low-lying excitations.

Finally, the effects of periodic organisation of tetrahedral clusters to superstructures are investigated. Despite the different overall structure and the organisation, the effects of surface saturation, which have been found for the single nanoparticles, are also found for these systems. However, the periodic arrangement shows no evidence of introducing major changes in the electronic properties. Nevertheless, organisation prevents structural changes at the sites of conjunction, although this may be considered as a special type of structural and electronic saturation. It further shows that surface saturation is very important for properties of semiconductor nanoparticles. Studying them should be a central subject for any investigation of large, but finite, systems.

This work establishes the DFTB (SCF-DFTB) method as general tool for the accurate and efficient investigation of properties of nanoparticles and related systems. Giving an outlook therefore provides the basis for the investigation of other II–VI semiconductor binary nanoparticles compounds, e. g., CdSe, CdTe, ZnS, ZnSe and ZnTe, as well as for the III–V analogues. For material research DFTB is predestined, since it allows the investigation of highly complex systems, e. g., core/shell structures, nanorods and tetrapods.

# Appendix A Series of experimentally characterised CdS clusters

This Section provides a systematic summary of the structures of CdS clusters. These structures are assigned to size series, which characterise them by crystal structure and shape [141]. Most of them exhibit a tetrahedral in some cases even cuboctahedral shape within the atomic structure being dominated by the bulk CdS modifications zinc blende and wurtzite or a mixture of them. The existence of both structures not surprising since the energetic difference between these two structures is small although the basic processes of the structure formation are not yet known in detail.

## A.1 Zinc blende structure and tetrahedral shape

This series of clusters is derived from tetrahedral fragments of the cubic sphalerite lattice wherein the adamantine ($C_6H_{10}$) framework can be identified as central structural element [114]. $[Cd_4(SR)_{10}]^{2-}$, $[S_4Cd_{10}(SR)_{16}]^{4-}$, $[S_{13}Cd_{20}(SR)_{22}]^{8-}$ and $[S_{28}Cd_{35}(SR)_{28}]^{14-}$.

The thiolate ligands terminating the edges and vertices of the supertetrahedron, without disruption of the molecular lattice structure or modification of the metal coordination stereochemistry, and the thiolate ligands do not affect the faces.

*Hagen et al.* [189] where able to isolate the smallest cluster of this series $[Cd_4(SR)_{10}]^{2-}$ with (R=Ph). The four Cd atoms are located at the vertex of a triangular pyramid.

When placing one more Cd atoms to each of the edge positions the decanuclear complex $[Cd_{10}(SR)_{16}]^{4-}$ was obtained by *Lacelle et al.* [115]. If thiolate surfactants at the planes of this cluster are replaced by single S atoms $[Cd_{10}(SR)_{12}]$ is formed. The $[S_4Cd_{10}(SCH_2CH_2OH)_{16}]^{4-}$ have been synthesised by *Strickle* [113]. This cluster has mercaptoethanol ligands. It is obtained by adding four $-SR$ ligands that coordinate to each Cd atom at the four vertexes of the $Cd_{10}S_{16}$-tetrahedron. The equivalent cluster $[S_4Cd_{10}(SCH_2CH_2OH)_{16}]^{4-}$ with thiophenolate ligands was found by *Dance et al.* [114].

Larger clusters in this series are $[S_{13}Cd_{20}(SR)_{22}]^{8-}$ and $[S_{28}Cd_{35}(SR)_{28}]^{14-}$ which are constructed by adding for or five Cd atoms on each side of the triangular pyramid. The latter pyramidal cluster seems unstable, because the four Cd atoms at the vertex tend to leave the cluster through the MO-calculation process with geometry optimisation [149].

## A.2 Wurtzite structure with tetrahedral shape

CdS clusters exhibiting only structural elements of wurtzite have not been observed experimentally, which is explained with a large electric polarisation for the small clusters [24]. The smallest member if such a series may be $[S_1Cd_4(SR)_{10}]^{4-}$ with a barelanoid* like cage structure. The instability of these may from the large electric polarisation in a small cluster. $[S_1Cd_4(SH)_{10}]^{4-}$ is 14.0D, while that of zinc blende type $[Cd_4(SH)_{10}]^{2-}$ is 1.5D. To form wurtzite type Cd-thiolate clusters this large dipole moment neutralised.

## A.3 Zinc blende/wurtzite mixed structure with tetrahedral shape

A first cluster series is constructed tetra capped tetrahedral-core (wurtzite) topology [117] , with barelanoid cages at the core/cap interfaces: $[SCd_8(SR)_{12}]^{2+}$ being the first member, $[S_6Cd_{26}(SR)_{28}]^{8-}$ (second) and $[S_{50}Cd_{60}(SR)_{40}]^{20-}$ (third). When $n$ is the number of layers of $[CdS_4]$ tetrahedron in the core the total number $N$ of Cd atoms can be derived by $N = (n + l)(n + 2)(5n + 3)/6$. In the case of $[SCd_8(SR)_{12}]^{2+}$ the large dipole moment mentioned in the previous is compensated by assembling four barelanoid units that have the central $SCd_4^-$ unit in common.

The second series consists of a adamantine core structure with barelanoid caps at the tetrahedral pyramid vertices [117]: $[S_4Cd_{17}(SR)_{28}]^{2-}$ is the third member with a Cd atom in the centre, $[S_{14}Cd_{32}(SR)_{40}]^{4-}$ the fourth member and $[S_{32}Cd_{54}(SR)_{52}]^{8-}$ the fifth member.

These clusters with mixed structures are most reported. One reason, mainly discussed for their appearance is their almost zero dipole moment which stabilise them. From the first series only the $[SCd_8(SR)_{12}]^{2+}$ was reported [148], where as the second shows two main exponents. *Dance et al.* [117] reported of $Cd_{17}S_4(SC_6H_5)_{28}]^{2-}$ in which all Cd atoms are fourfold coordinated and the surface S atoms are bridging two Cd atoms except the four at the vertex that are just single bonded. *Herron et al.* [118] report of $[Cd_{32}S_{14}(SPh)_{36}]^{4-}$ and with similar a build up, but the centre is not located at a Cd atom than in the a adamantine like unit. Moreover *Vossmeyer et al.* succeeded in arranging this clusters periodically in a crystal structure $Cd_{17}S_4(SCH_2CH_2OH)_{26}$ [119] and $Cd_{32}S_{14}(SCH_2CH(CH_3)OH)_{36}$ [120].

## A.4 Zinc blende structure with cuboctahedral shape

The series of cuboctahedral shaped zinc blende derived clusters is a successive build-up of nearest-neighbour bonds shells whereas the centre of the cluster is located at an atom position [122]. When this is a Cd atom $Cd(SR)_4$ is the smallest representative of the series: $[S_4Cd_{13}(SR)_{24}]^{6-}$ and $[S_{28}Cd_{55}(SR)_{64}]^{10-}$ correspond to four and six shells, that are added.

*(The barelanoidal structure corresponds to the 1,4-diazabicyclo[2.2.2]octane (DABCO) framework.

If a S at the centre, $[S_1Cd_4(SR)_{12}]^{6-}$ is obtained within three shells. $[S_{13}Cd_{28}(SR)_{42}]^{12-}$ and $[S_{55}Cd_{92}(SR)_{92}]^{18-}$ have five and seven shells, respectively. Alternatively this cuboctahedral shaped particles can be considered as tetrahedron from which the vertices have been removed.

# Appendix B Additional Figures

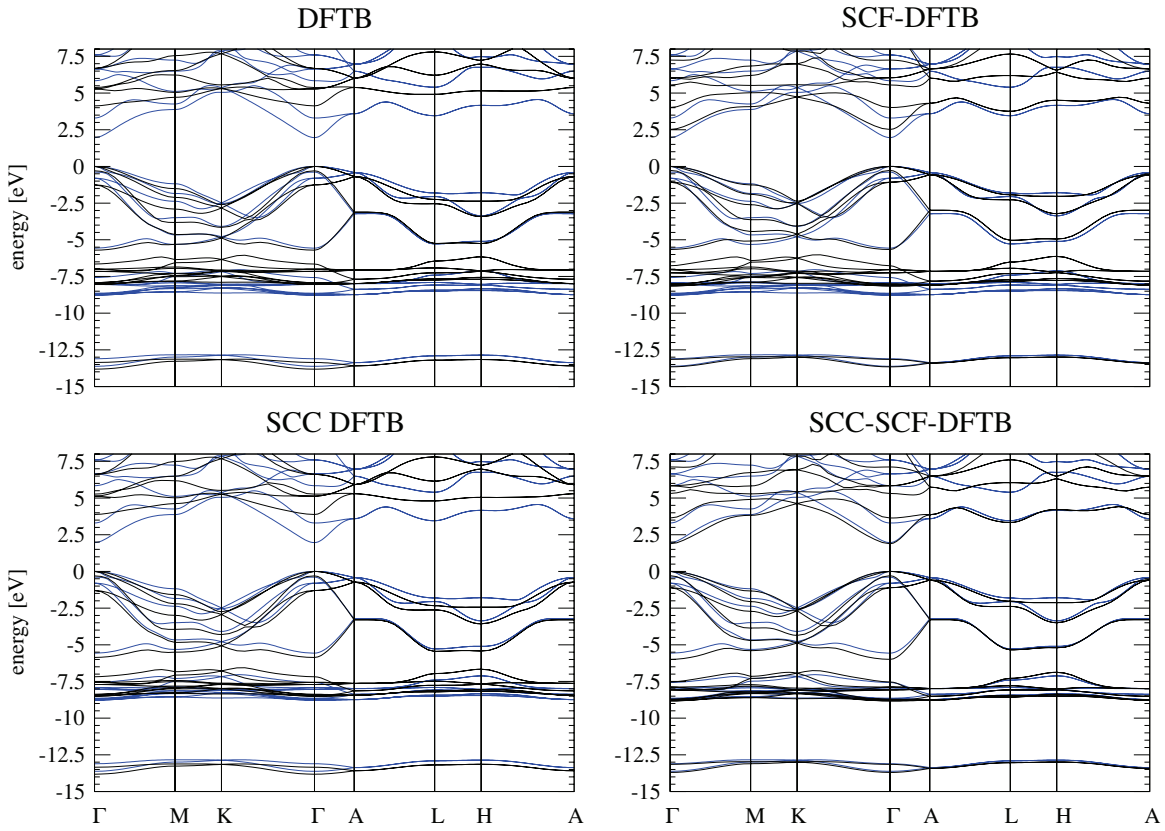


Figure B.1: *Calculated bandstructures of wurtzite CdS using DFTB (left panels), SCF-DFTB (right panels) and the results which include the SCC-correction (lower panels). The reference bandstructure is represented by a SCF-DFT calculation (blue curves). The Further details of the calculations are given in Section 5.2.*

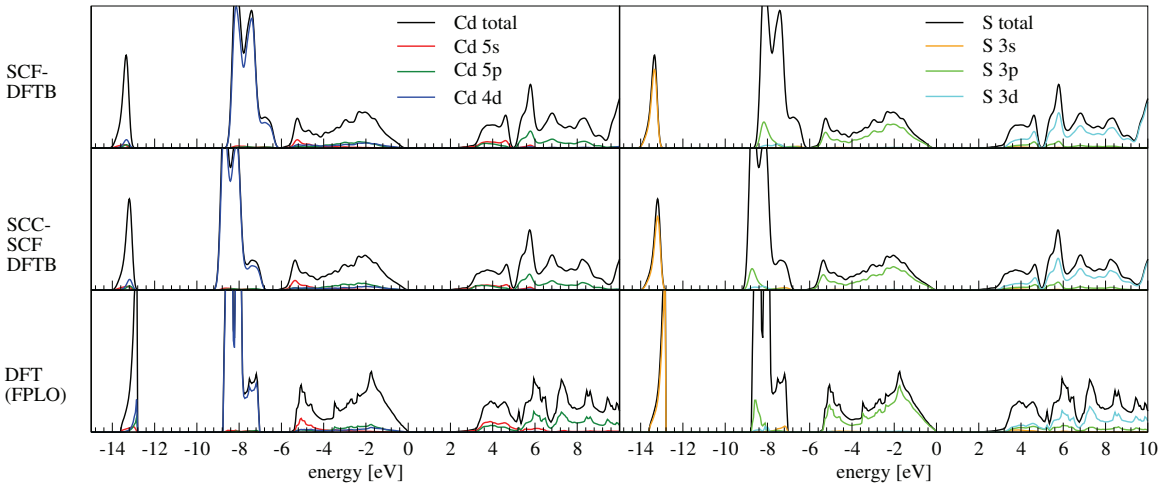


Figure B.2: *Calculated electronic DOS of wurtzite CdS bulk corresponding to the band-structures in Figure B.1. Additionally the projected DOS (p-DOS) to the atomic functions of Cd (left column) and S (right column) is depicted. The valence band edge is shifted to* 0 *eV. Further details of the calculations are given in Section 5.2.*

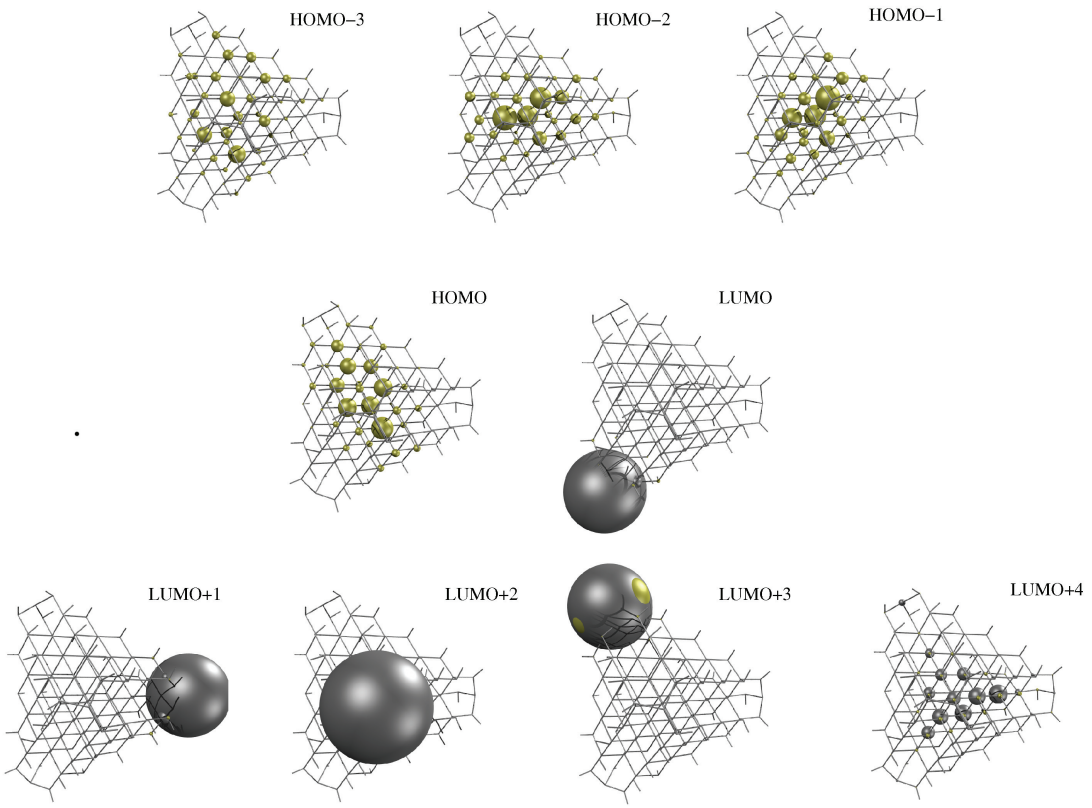


Figure B.3: *Frontier orbitals of* $[Cd_{54}S_{32}(SR)_{48}]^{4-}$ *with saturation defect: The four missing ligands at the vertices cause dangling bonds which affect the optical properties. These are discussed in (cf. Section 8.4). More information in the structures are given in Table 8.1 and the corresponding optical excitation spectrum in Figure 8.2. The SCF-DFTB MO energies are depicted in Figure 8.1. For better depiction the MO's (SCF-DFTB) are approximated by the projected atomic contributions (sulphur yellow; cadmium grey colour) to the orbital (*Mulliken-*population analysis) represented as spheres centred at the corresponding atom.*

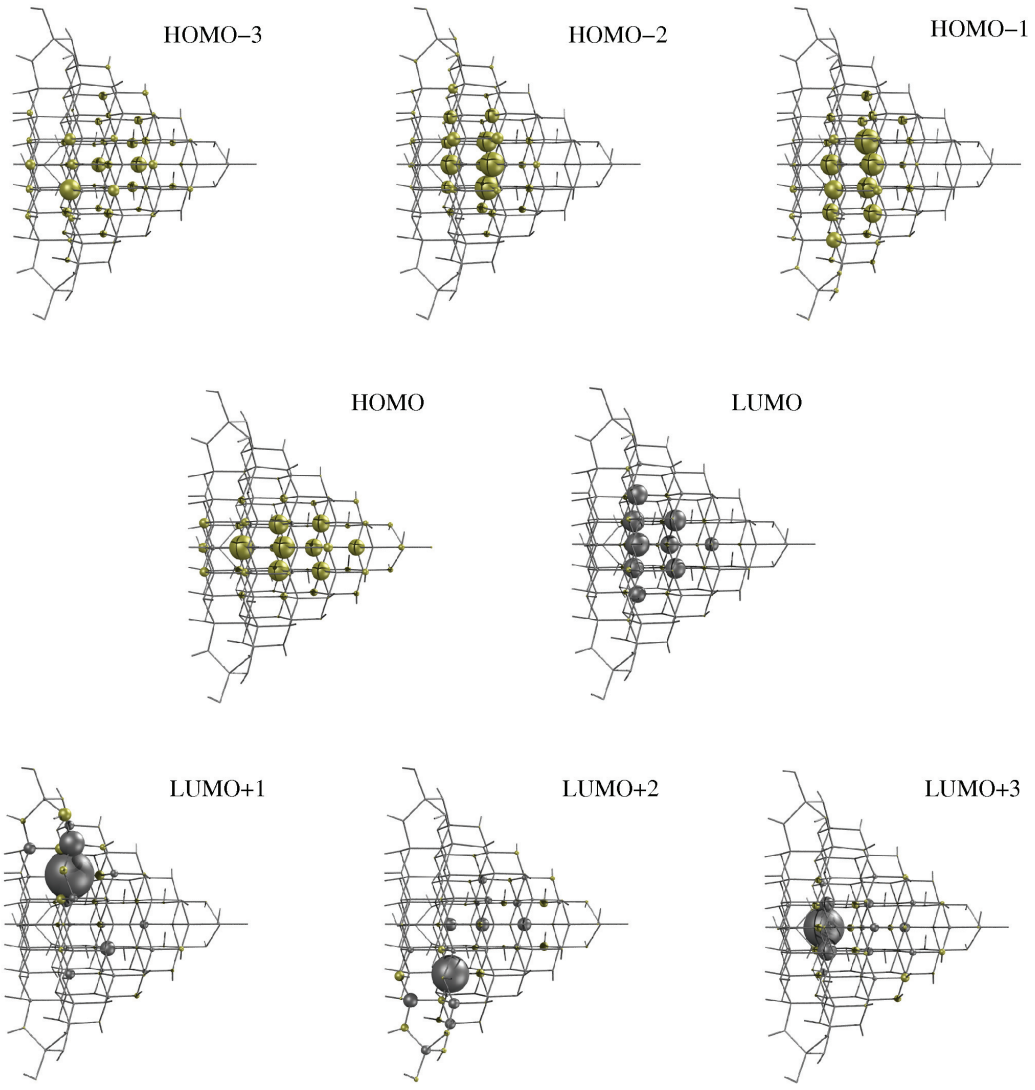


Figure B.4: *Frontier orbitals of* $[Cd_{54}S_{32}(SR)_{52}]^{8-}$*: The four missing ligands at the vertices of the structure* $[Cd_{54}S_{32}(SR)_{48}]^{4-}$ *(cf. Figure 8.4) are added. The optical properties are discussed in Sections 8.2 and 8.4. More information in the structures are given in Table 8.1 and the corresponding optical excitation spectrum in Figure 8.2. The SCF-DFTB MO energies are depicted in Figure 8.1. For better depiction the MO's (SCF-DFTB) are approximated by the projected atomic contributions (sulphur yellow; cadmium grey colour) to the orbital (*Mulliken*-population analysis) represented as spheres centred at the corresponding atom.*

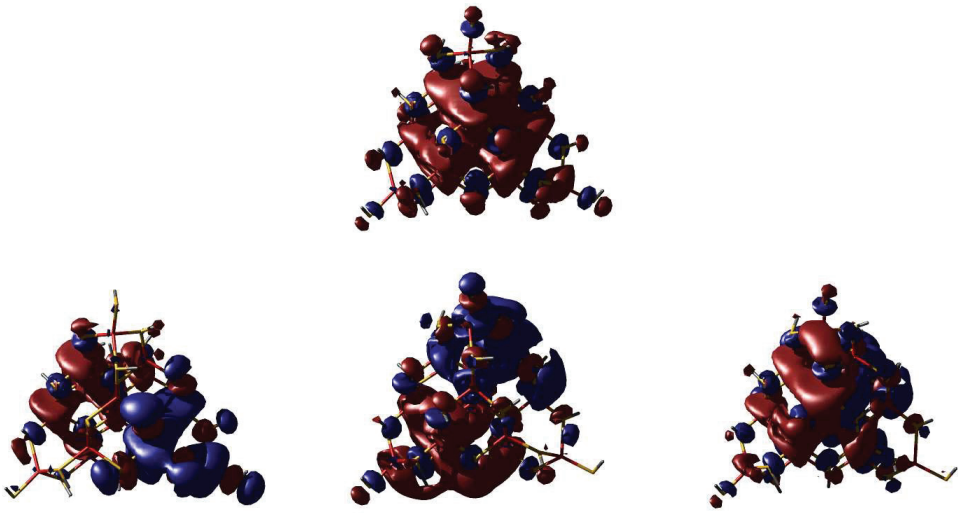

Figure B.5: *Frontier orbitals of* $[Cd_{17}S_4(SH_{28})]^{2-}$*: LUMO (upper structure) and the energetically degenerated LUMO+1, LUMO+2 and LUMO+3 (lower structures).*

# Bibliography


[1] Yoffe, A. D., Semiconductor quantum dots and related systems: electronic, optical, luminescence and related properties of low dimensional systems, Advances in Physics **50**, 1–208 (2001). 1

[2] Schmid, G., (ed.) *Nanoparticles. From Theory to Application* (Wiley-VCH, Weinheim, 2004). 1, 35, 58

[3] Chan, W. C. W. and Nie, S., Quantum dot bioconjugates for ultrasensitive nonisotopic detection, Science **281**, 2016–2018 (1998). 1

[4] Bruchez, M., J., Moronne, M., Gin, P., Weiss, S., and Alivisatos, A. P., Semiconductor nanocrystals as fluorescent biological labels, Science **281**, 2013–2016 (1998). 1

[5] Jaiswal, J. K., Goldman, E. R., Mattoussi, H., and Simon, S. M., Use of quantum dots for live cell imaging, Nature Methods **1**, 73–78 (2004). 1

[6] Colvin, V. L., Schlamp, M. C., and Alivisatos, A. P., Light-emitting diodes made from cadmium selenide nanocrystals and a semiconducting polymer, Nature **370**, 354–357 (1994). 1

[7] Huynh, W. U., Dittmer, J. J., and Alivisatos, A. P., Hybrid nanorod-polymer solar cells, Science **295**, 2425–2427 (2002). 1

[8] Gur, I., Fromer, N. A., Geier, M. L., and Alivisatos, A. P., Air-stable all-inorganic nanocrystal solar cells processed from solution, Science **310**, 462–465 (2005). 1

[9] Klimov, V. I., Mikhailovsky, A. A., Xu, S., Malko, A., Hollingsworth, J. A., Leatherdale, C. A., Eisler, H.-J., and Bawendi, M. G., Optical gain and stimulated emission in nanocrystal quantum dots, Science **290**, 314–317 (2000). 1

[10] Achermann, M., Petruska, M. A., Kos, S., Smith, D. L., Koleske, D. D., and Klimov, V. I., Energy-transfer pumping of semiconductor nanocrystals using an epitaxial quantum well, Nature **429**, 642–646 (2004). 1

[11] Madelung, O. and Schulz, M., *Crystal and Solid: Semiconductors*, in Madelung, O. and Schulz, M., (eds.) *Landholt-Börnstein*, vol. Vol: 17a and 22a of *Nummerical Data and Functional Relationships in Science and Technology*, chap. Semiconductors, p.

194 (Springer, Berlin, Heidelberg, New York, London, Paris, Tokio, 1986). 1, 27, 35, 36, 46, 70, 77

[12] Holleman, A. F., Wiberg, E., and Wiberg, N., *Holleman-Wiberg – Lehrbuch der Anorganischen Chemie*, chap. Die Zinkgruppe, p. 1375, 101 edn. (de Gruyter, Berlin - New York, 1995). 1

[13] Henglein, A., *Photochemistry of colloidal cadmium sulfide. 2. Effects of adsorbed methyl viologen and of colloidal platinum*, Ber. Bunsenges. Phys. Chem. **86**, 301–305 (1982). 1

[14] Brus, L. E., A simple model for the ionization potential, electron affinity, and aqueous redox potentials of small semiconductor crystallites, The Journal of Chemical Physics **79**, 5566–5571 (1983). 1, 55

[15] Eychmüller, A., *3.1.1 Synthesis and characterization of II-VI nanoparticles; 4.1Semiconductor nanoparticles*, in Schmid, G., (ed.) *Nanoparticles* (Wiley-VCH, Weinheim, 2004). 1

[16] Murray, C. B., Norris, D. J., and Bawendi, M. G., Synthesis and Characterization of Nearly Monodisperse Cde (E = S, Se, Te) Semiconductor Nanocrystallites, Journal of the American Chemical Society **115**, 8706–8715 (1993). 1, 38, 39, 55, 63, 69

[17] Brus, L. E., Electron–electron and electron-hole interactions in small semiconductor crystallites: The size dependence of the lowest excited electronic state, The Journal of Chemical Physics **80**, 4403–4409 (1984). 1

[18] Henglein, A., *Mechanism of reactions on colloidal microelectrodes and size quantization effects*, in Steckhan, E., (ed.) *Electrochemistry II*, vol. 143 of *Topics in Current Chemistry*, chap. Mechanism of reactions on colloidal microelectrodes and size quantization effects, pp. 113–180 (Springer Berlin / Heidelberg, 1988). 1, 55

[19] Ekimov, A. I., Efros, A. L., Ivanov, M. G., Onushchenko, A. A., and Shumilov, S. K., Donor-like exciton in zero-dimension semiconductor structures, Solid State Communications **69**, 565–568 (1989). 1

[20] Yoffe, A. D., Low-dimensional systems: Quantum size effects and electronic properties of semiconductor microcrystallites (zero-dimensional systems) and some quasi-two-dimensional systems, Advances in Physics **51**, 799–890 (2002). 1

[21] Goldstein, A. N., Echer, C. M., and Alivisatos, A. P., Melting in semiconductor nanocrystals, Science **256**, 1425–1427 (1992). 1

[22] Tolbert, S. H. and Alivisatos, A. P., The wurtzite to rock salt structural transformation in CdSe nanocrystals under high pressure, The Journal of Chemical Physics **102**, 4642–4656 (1995). 1, 66, 69, 81

[23] Alivisatos, A., Perspectives on the Physical Chemistry of Semiconductor Nanocrystals, Journal of Physical Chemistry **100**, 13226–13239 (1996). 2, 55

[24] Eychmüller, A., Structure and photophysics of semiconductor nanocrystals, Journal of Physical Chemistry B **104**, 6514–6528 (2000). 2, 43, 71, 98

[25] Qu, L. and Peng, X., Control of photoluminescence properties of CdSe nanocrystals in growth, Journal of the American Chemical Society **124**, 2049–2055 (2002). 2, 50, 69

[26] Talapin, D., Rogach, A., Shevchenko, E., Kornowski, A., Haase, M., and Weller, H., Dynamic distribution of growth rates within the ensembles of colloidal II-VI and III-V semiconductor nanocrystals as a factor governing their photoluminescence efficiency, Journal of the American Chemical Society **124**, 5782–5790 (2002). 2, 50, 69

[27] Gomez, D. E., van Embden, J., Jasieniak, J., Smith, T. A., and Mulvaney, P., Blinking and surface chemistry of single CdSe nanocrystals, Small **2**, 204–208 (2006). 2, 69

[28] Banin, U., Bruchez, M., Alivisatos, A. P., Ha, T., Weiss, S., and Chemla, D. S., Evidence for a thermal contribution to emission intermittency in single CdSe/CdS core/shell nanocrystals, The Journal of Chemical Physics **110**, 1195–1201 (1999). 2

[29] Cao, Y. and Banin, U., Growth and properties of semiconductor core/shell nanocrystals with InAs cores, Journal of the American Chemical Society **122**, 9692–9702 (2000). 2

[30] Gerion, D., Pinaud, F., Williams, S., Parak, W., Zanchet, D., Weiss, S., and Alivisatos, A., Synthesis and Properties of Biocompatible Water-Soluble Silica-Coated CdSe/ZnS Semiconductor Quantum Dots, Journal of Physical Chemistry B **105**, 8861–8871 (2001). 2

[31] Malik, M., O'Brien, P., and Revaprasadu, N., A Simple Route to the Synthesis of Core/Shell Nanoparticles of Chalcogenides, Chemistry of Materials **14**, 2004–2010 (2002). 2

[32] Schrödinger, E., Quantisierung als Eigenwertproblem (Erste Mitteilung), Annalen der Physik **384**, 361–376 (1926). 5

[33] Schrödinger, E., Quantisierung als Eigenwertproblem, Annalen der Physik **384**, 489–527 (1926). 5

[34] Schrödinger, E., Quantisierung als Eigenwertproblem, Annalen der Physik **385**, 437–490 (1926). 5

[35] Born, M. and Oppenheimer, R., Zur quantentheorie der molekeln, Annalen der Physik **389**, 457–484 (1927). 6

[36] Møller, C. and Plesset, M. S., Note on an Approximation Treatment for Many-Electron Systems, Physical Review **46**, 618–622 (1934). 6

[37] Szabo, A. and Ostlund, N., *Modern Quantum Chemistry* (McGraw-Hill, New York, 1989). 6

[38] Parr, R. and Yang, W., *Density-functional theory of atoms and molecules*, no. 16 in International Series of Monographs on Chemistry (Oxford University Press, Oxford, 1989). 7, 8, 16

[39] Scherz, U., *Quantenmechanik* (B.G. Teubner, Stuttgart, 1999). 7

[40] Hohenberg, P. and Kohn, W., Inhomogeneous electron gas, Physical Review **136**, B864–B871 (1964). 7

[41] Kohn, W. and Sham, L. J., Self-Consistent Equations Including Exchange and Correlation Effects, Physical Review **140**, A1133–A1138 (1965). 7, 8

[42] Fermi, E., *Un metodo statistico per la determinazione di alcune proprietà dell'atomo*, in *Rend. Accad. Lincei* [43], pp. 602–607. 7

[43] Fermi, E., *Eine statistische Methode zur Bestimmung einiger Eigenschaften des Atoms und ihre Anwendung auf die Theorie des periodischen Systems der Elemente*, Zeitschrift für Physik **48**, 73 (1928). 7, 110

[44] Lieb, E. H., Thomas-Fermi and related theories of atoms and molecules, Reviews in Modern Physics **53**, 603–641 (1981). 7

[45] March, N., *Electron Density Theory of Atoms and Molecules*, Theoretical Chemistry; a Series of Monographs (Academic Press, London, 1992). 7

[46] Dreizler, R. and Gross, E., *Density-functional-theory* (Springer-Verlag, Berlin, 1990). 8

[47] Slater, J. C., A Simplification of the Hartree-Fock Method, Physical Review **81**, 385–390 (1951). 9

[48] Gaspar, R., *Über eine Approximation der hartreefogkschen Potentials durch eine universelle Potentialfunktion*, Acta Phys. Acad. Sci. Hung. **3**, 263–286 (1954). 9

[49] Schwarz, K., Optimization of the Statistical Exchange Parameter $\alpha$ for the Free Atoms H through Nb, Physical Review B **5**, 2466–2468 (1972). 9

[50] Ceperley, D. M. and Alder, B. J., Ground state of the electron gas by a stochastic method, Physical Review Letters **45**, 566–569 (1980). 9

[51] Hedin, L. and Lundqvist, B. I., Explicit local exchange-correlation potentials, Journal of Physics C: Solid State Physics **4**, 2064–2083 (1971). 9

[52] Vosko, S., Wilk, L., and Nusair, M., Accurate spin-dependent electron liquid correlation energies for local spin density calculations: A critical analysis, Canadian Journal of Physics **58**, 1200–1211 (1980). 9

[53] Perdew, J. P., Density-functional approximation for the correlation energy of the inhomogeneous electron gas, Physical Review B **33**, 8822–8824 (1986). 10

[54] Becke, A. D., Density-functional exchange-energy approximation with correct asymptotic behavior, Physical Review A **38**, 3098–3100 (1988). 10

[55] Lee, C., Yang, W., and Parr, R. G., Development of the Colle-Salvetti correlation-energy formula into a functional of the electron density, Physical Review B **37**, 785–789 (1988). 10

[56] Perdew, J. P. and Wang, Y., Accurate and simple analytic representation of the electron-gas correlation energy, Physical Review B **45**, 13244–13249 (1992). 10

[57] Perdew, J. P., Chevary, J. A., Vosko, S. H., Jackson, K. A., Pederson, M. R., Singh, D. J., and Fiolhais, C., Atoms, molecules, solids, and surfaces: Applications of the generalized gradient approximation for exchange and correlation, Physical Review B **46**, 6671–6687 (1992). 10

[58] Burke, K., Perdew, J., and Ernzerhof, M., Why the generalized gradient approximation works and how to go beyond it, International Journal of Quantum Chemistry **61**, 287 (1997). 10

[59] Eschrig, H., *Optimized LCAO method and the electronic structure of extended systems* (Akademie-Verlag, Berlin, 1988). 10, 13, 29

[60] Seifert, G., Eschrig, H., and Bieger, W., Eine approximativ Variante des LCAO-$X_\alpha$-Verfahrens, Zeitschrift für physikalische Chemie (Leipzig) **267**, 529 (1986). 11, 12, 13

[61] Porezag, D., Frauenheim, T., Köhler, T., Seifert, G., and Kaschner, R., Construction of tight-binding-like potentials on the basis of density-functional theory: Application to carbon, Physical Review B **51**, 12947–12957 (1995). 11, 12, 14, 23

[62] Frauenheim, T., Seifert, G., Elsterner, M.and Hajnal, Z., Jungnickel, G., Porezag, D., Suhai, S., and Scholz, R., A self-consistent charge density-functional based tight-binding method for predictive materials simulations in physics, chemistry and biology, physica status solidi (b) **217**, 41–62 (2000). 11

[63] Frauenheim, T., Seifert, G., Elstner, M., Niehaus, T., C., K., Amkreutz, M., Sternberg, M., Hajnal, Z., di Carlo, A., and Suhai, S., Atomistic simulations of complex materials: Ground-state and excited-state properties, Journal of Physics: Condensed Matter **14**, 3015–3047 (2002). 11

[64] Goringe, C. M., Bowler, D. R., and Hernández, E., Tight-binding modelling of materials, Reports on Progress in Physics **60**, 1447–1512 (1997). 11

[65] Elstner, M., Porezag, D., Jungnickel, G., Elsner, J., Haugk, M., Frauenheim, T., Suhai, S., and Seifert, G., Self-consistent-charge density-functional tight-binding method for simulations of complex materials properties, Physical Review B **58**, 7260–7268 (1998). 11, 15

[66] Köhler, C., Seifert, G., Gerstmann, U., Elstner, M., Overhof, H., and Frauenheim, T., Approximate density-functional calculations of spin densities in large molecular systems and complex solids, Physical Chemistry Chemical Physics **3**, 5109–5114 (2001). 11

[67] Niehaus, T. A., Suhai, S., Della Sala, F., Lugli, P., Elstner, M., Seifert, G., and Frauenheim, T., Tight-binding approach to time-dependent density-functional response theory, Physical Review B **63**, 085108 (2001). 11, 17, 18

[68] Köhler, T., Frauenheim, T., and Jungnickel, G., Stability, chemical bonding, and vibrational properties of amorphous carbon at different mass densities, Physical Review B **52**, 11837–11844 (1995). 11

[69] Jackson, K., Pederson, M. R., Porezag, D., Hajnal, Z., and Frauenheim, T., Density-functional-based predictions of Raman and IR spectra for small Si clusters, Physical Review B **55**, 2549–2555 (1997). 11

[70] Sternberg, M., Frauenheim, T., Zimmermann-Edling, W., and Busmann, H. G., STM images from diamond surfaces: steps towards comparisons of experiment and theory, Surface Science **370**, 232–244 (1997). 11

[71] Heine, T., Buhl, M., Fowler, P. W., and Seifert, G., Modelling the $^{13}$C NMR chemical shifts of $C_{84}$ fullerenes, Chemical Physics Letters **316**, 373–380 (2000). 11

[72] Heine, T., Seifert, G., Fowler, P., and Zerbetto, F., A tight-binding treatment for $^{13}C$ NMR spectra of fullerenes, Journal of Physical Chemistry A **103**, 8738–8746 (1999). 11

[73] Heine, T., Zerbetto, F., Seifert, G., and Fowler, P., $^{13}C$ NMR patterns of odd-numbered $C_{119}$ fullerenes, Journal of Physical Chemistry A **104**, 3865–3868 (2000). 11

[74] Sternberg, M., Galli, G., and Frauenheim, T., NOON – A non-orthogonal localised orbital order-N method, Computer Physics Communications **118**, 200–212 (1999). 11

[75] Hazebroucq, S., Picard, G. S., Adamo, C., Heine, T., Gemming, S., and Seifert, G., Density-functional-based molecular-dynamics simulations of molten salts, The Journal of Chemical Physics **123**, 134510 (pages 9) (2005). 11

[76] Frenzel, J., Gemming, S., and Seifert, G., Electronic structure of $Ga_{84}$ cluster compounds, Physical Review B **70**, 235404 (pages 8) (2004). 11

[77] Frenzel, J., Oliveira, A. F., Duarte, H. A., Heine, T., and Seifert, G., Structural and electronic properties of bulk gibbsite and gibbsite surfaces, Zeitschrift für anorganische und allgemeine Chemie **631**, 1267–1271 (2005). 11

[78] Frenzel, J., Joswig, J.-O., Sarkar, P., Seifert, G., and Springborg, M., The effects of organisation, embedding and surfactants on the properties of cadmium chalcogenide (CdS, CdSe and CdS/CdSe) semiconductor nanoparticles, European Journal of Inorganic Chemistry **18**, 3585–3596 (2005). 11, 37

[79] Heine, T., Fowler, P. W., and Seifert, G., $C_{36}$: from dimer to bulk, Solid State Communications **111**, 19–22 (1999). 11

[80] Haugk, M., Elsner, J., Frauenheim, T., Staab, T., Latham, C., Jones, R., Leipner, H., Heine, T., Seifert, G., and Sternberg, M., Structures, energetics and electronic properties of complex III-V semiconductor systems, physica status solidi (b) **217**, 473–511 (2000). 11

[81] Chen, Z., Jiao, H., Seifert, G., Horn, A. H. C., Yu, D., Clark, T., Thiel, W., and Schleyer, P. v. R., The structure and stability of $Si_{60}$ and $Ge_{60}$ cages: A computational study, Journal of Computational Chemistry **24**, 948–953 (2003). 11

[82] Elstner, M., The SCC-DFTB method and its application to biological systems, Theoretical Chemistry Accounts: Theory, Computation, and Modeling (Theoretica Chimica Acta) **V116**, 316–325 (2006). 11

[83] Ivanovskaya, V. V., Heine, T., Gemming, S., and Seifert, G., Structure, stability and electronic properties of composite $Mo_{1-x}Nb_xS_2$ nanotubes, physica status solidi (b) **243**, 1757–1764 (2006). 11

[84] Enyashin, A. N. and Seifert, G., Structure, stability and electronic properties of $TiO_2$ nanostructures, physica status solidi (b) **242**, 1361–1370 (2005). 11

[85] Rogers, K. M., Fowler, P. W., and Seifert, G., Chemical versus steric frustration in boron nitride heterofullerene polyhedra, Chemical Physics Letters **332**, 43–50 (2000). 11

[86] Seifert, G., Terrones, H., Terrones, M., Jungnickel, G., and Frauenheim, T., On the electronic structure of $WS_2$ nanotubes, Solid State Communications **114**, 245–248 (2000). 11

[87] Elstner, M., Frauenheim, T., Kaxiras, E., Seifert, G., and Suhai, S., A self-consistent charge density-functional based tight-binding scheme for large biomolecules, physica status solidi (b) **217**, 357–376 (2000). 11

[88] Aradi, B., *DFTB$^+$ 2006*, Homepage: http://www.dftb.org, URL `http://www.dftb.org`. 11

[89] Köster, A., Flores-Moreno, R., Geudtner, G., Goursot, A., Heine, T., Reveles, J., Vela, A., Patchkovskii, S., and Salahub, D. R., *deMon 2004, NRC, Canada*, Hompage http://www.deMon-Software.com, URL `http://www.deMon-Software.com`. 11

[90] Phillips, J. C. and Kleinman, L., New method for calculating wave functions in crystals and molecules, Physical Review **116**, 287–294 (1959). 12

[91] Wigner, E. and Seitz, F., On the constitution of metallic sodium, Physical Review **43**, 804–810 (1933). 13, 21, 23

[92] Wigner, E. and Seitz, F., On the Constitution of Metallic Sodium. II, Physical Review **46**, 509–524 (1934). 13, 21, 23

[93] Eschrig, H. and Bergert, I., An optimized LCAO version for band structure calculations application to copper, physica status solidi (b) **90**, 621–628 (1978). 13, 29

[94] Tomańek, D. and Schlüter, M. A., Structure and bonding of small semiconductor clusters, Physical Review B **36**, 1208–1217 (1987). 15

[95] Mulliken, R. S., Electronic Population Analysis on LCAO – MO Molecular Wave Functions. I, The Journal of Chemical Physics **23**, 1833–1840 (1955). 16, 18, 24, 56

[96] Slater, J. C. and Koster, G. F., Simplified LCAO Method for the Periodic Potential Problem, Physical Review **94**, 1498–1524 (1954). 16

[97] Casida, M. E., *Time-dependent density functional response theory for molecules*, in Chong, D. P., (ed.) *Recent advances in density functional theory*, vol. Part I of *Recent Advances in Computational Chemistry*, p. 155 (World Scientific, Singapore, 1995), ISBN 981-02-2442-7. 17

[98] Casida, M. E., *Time-dependent density functional response theory of molecular systems: theory, computational methods, and functionals*, in Seminario, J. M., (ed.) *Recent developments and applications of modern density functional theory*, vol. 4 of *Theoretical and Computational Chemistry*, chap. 11, p. 391 (Elsevier, Amsterdam, 1996). 17

[99] Koepernik, K. and Eschrig, H., Full-potential nonorthogonal local-orbital minimum-basis band-structure scheme, Physical Review B **59**, 1743–1757 (1999). 29, 30, 46

[100] von Barth, U. and Hedin, L., A local exchange-correlation potential for the spin polarized case., Journal of Physics C: Solid State Physics **5**, 1629–1642 (1972). 29

[101] Hill, N. A. and Whaley, K. B., Electronic structure of semiconductor nanoclusters: A time dependent theoretical approach, The Journal of Chemical Physics **99**, 3707–3715 (1993). 30, 37, 55, 58, 69

[102] Joswig, J.-O., Springborg, M., and Seifert, G., Structural and electronic properties of cadmium sulfide clusters, Journal of Physical Chemistry B **104**, 2617–2622 (2000). 30, 37, 38, 45, 46, 49, 50, 55, 56, 58, 63, 66

[103] Bawendi, M. G., Wilson, W. L., Rothberg, L., Carroll, P. J., Jedju, T. M., Steigerwald, M. L., and Brus, L. E., Electronic structure and photoexcited-carrier dynamics in nanometer-size CdSe clusters, Physical Review Letters **65**, 1623–1626 (1990). 30, 39, 40, 50, 58, 65, 69, 87

[104] Gurin, V. S., Electronic structure of CdS cores in Cd thiolate complexes and clusters, Journal of Physical Chemistry **100**, 869–872 (1996). 30, 50, 58

[105] Kobayashi, A., Sankey, O. F., Volz, S. M., and Dow, J. D., Semiempirical tight-binding band structures of wurtzite semiconductors: AlN, CdS, CdSe, ZnS, and ZnO, Physical Review B **28**, 935–945 (1983). 34, 66

[106] Chang, K. J., Froyen, S., and Cohen, M. L., Electronic band structures for zinc-blende and wurtzite CdS, Physical Review B **28**, 4736–4743 (1983). 34, 66

[107] Wang, Y. R. and Duke, C. B., Cleavage faces of wurtzite CdS and CdSe: Surface relaxation and electronic structure, Physical Review B **37**, 6417–6424 (1988). 34, 46, 50, 56, 66, 69

[108] Horsky, T. N., Brandes, G. R., Canter, K. F., Duke, C. B., Paton, A., Lessor, D. L., Kahn, A., Horng, S. F., Stevens, K., Stiles, K., and Mills, A. P., Analysis of the atomic geometries of the (1010) and (1120) surfaces of CdSe by low-energy-electron diffraction and low-energy-positron diffraction, Physical Review B **46**, 7011–7026 (1992). 34, 50, 56, 66

[109] Schröer, P., Krüger, P., and Pollmann, J., Self-consistent electronic-structure calculations of the (1010) surfaces of the wurtzite compounds ZnO and CdS, Physical Review B **49**, 17092–17101 (1994). 34, 50, 56, 66, 69

[110] Vogel, D., Krüger, P., and Pollmann, J., Ab initio electronic-structure calculations for II-VI semiconductors using self-interaction-corrected pseudopotentials, Physical Review B **52**, R14316–R14319 (1995). 34, 66

[111] Ulrich, F. and Zachariasen, W., *On the crystal structure of alpha and beta CdS, and wurtzite.*, Zeitschrift fuer Kristallographie **62 (3/4)**, 260–273 (1925). 35

[112] Rooymans, C. J. M., Structure of the high pressure phase of CdS, CdSe and InSb, Physical Letters **4 (3)**, 186–187 (1963). 35, 46

[113] Strickle, P., Structure of a novel polynuclear complex related to sphalerite lattice, Journal of the Chemical Society D-Chemical Communications **12**, 655 (1969). 37, 43, 71, 97

[114] Dance, I. G., Choy, A., and Scudder, M. L., Syntheses, properties, and molecular and crystal-structures of $(Me_{4n})_4$ $S_4Zn_{10}(SPh)_{16}$ $(Me_{4n})N$ $Se_4Cd_{10}(SPh)_{16}$ - Molecular supertetrahedral fragments of the cubic metal chalcogenide lattice, Journal of the American Chemical Society **106**, 6285–6295 (1984). 37, 43, 71, 97

[115] Lacelle, S., Stevens, W. C., Kurtz, D. M., Richardson, J. W., and Jacobson, R. A., Crystal and Molecular-Structure of $Cd_{10}(SCH_2CH_2OH)_{16}(ClO_4)_4{\cdot}8H_2O$ - Correlations with $^{113}Cd$ NMR-spectra of the solid and implications for cadmium thiolate ligation in proteins, Inorganic Chemistry **23**, 930–935 (1984). 37, 97

[116] Dance, I. G., The structural chemistry of metal thiolate complexes, Polyhedron **5**, 1037–1104 (1986). 37, 39

[117] Lee, G. S. H., Craig, D. C., Ma, I., Scudder, M. L., Bailey, T. D., and Dance, I. G., $[S_4Cd_{17}(SPh)_{28}]^{2-}$, the 1st member of a 3rd series of tetrahedral $[S_mM_x(SR)_y]^{z-}$ clus-

ters, Journal of the American Chemical Society **110**, 4863–4864 (1988). 37, 39, 89, 98

[118] Herron, N., Calabrese, J. C., Farneth, W. E., and Wang, Y., Crystal-structure and optical-properties of $Cd_{32}S_{14}(SC_6H_5)_{36}\cdot DMF_4$, a cluster with a 15-Angstrøm CdS Core, Science **259**, 1426–1428 (1993). 37, 39, 41, 43, 71, 89, 98

[119] Vossmeyer, T., Reck, G., Katsikas, L., Haupt, E. T. K., Schulz, B., and Weller, H., A "double-diamond superlattice" built up of $Cd_{17}S_4(SCH_2CH_2OH)_{26}$ clusters, Science **267**, 1476–1479 (1995). 37, 39, 43, 71, 89, 98

[120] Vossmeyer, T., Reck, G., Schulz, B., Katsikas, L., and Weller, H., Double-layer superlattice structure built up of $Cd_{32}S_{14}(SCH_2CH(OH)CH_3)_{36}\cdot$ 4 $H_2O$ clusters, Journal of the American Chemical Society **117**, 12881–12882 (1995). 37, 39, 41, 43, 71, 89, 98

[121] Wang, L.-W. and Zunger, A., Pseudopotential calculations of nanoscale CdSe quantum dots, Physical Review B **53**, 9579–9582 (1996). 37, 55, 63

[122] Lippens, P. E. and Lannoo, M., Calculation of the band gap for small CdS and ZnS crystallites, Physical Review B **39**, 10935–10942 (1989). 37, 43, 55, 63, 71, 98

[123] Hill, N. A. and Whaley, K. B., A theoretical study of the influence of the surface on the electronic structure of CdSe nanoclusters, The Journal of Chemical Physics **100**, 2831–2837 (1994). 37, 65

[124] Leung, K. and Whaley, K. B., Surface relaxation in CdSe nanocrystals, The Journal of Chemical Physics **110**, 11012–11022 (1999). 37, 40, 50, 55

[125] Pokrant, S. and Whaley, K. B., Tight-binding studies of surface effects on electronic structure of CdSe nanocrystals: the role of organic ligands, surface reconstruction, and inorganic capping shells, European Physical Journal D **6**, 255–267 (1999). 37, 40, 50, 55, 65, 69

[126] Eichkorn, K. and Ahlrichs, R., Cadmium selenide semiconductor nanocrystals: A theoretical study, Chemical Physics Letters **288**, 235–242 (1998). 37, 40, 50, 55

[127] Troparevsky, M. C. and Chelikowsky, J. R., Structural and electronic properties of CdS and CdSe clusters, The Journal of Chemical Physics **114**, 943–949 (2001). 37, 50

[128] Puzder, A., Williamson, A. J., Gygi, F., and Galli, G., Self-healing of CdSe nanocrystals: First-principles calculations, Physical Review Letters **92**, 217401 (pages 4) (2004). 37, 50

[129] Joswig, J. O., Roy, S., Sarkar, P., and Springborg, M., Stability and bandgap of semiconductor clusters, Chemical Physics Letters **365**, 75–81 (2002). 37, 49

[130] Sarkar, P. and Springborg, M., Density-functional study of size-dependent properties of $Cd_mSe_n$ clusters, Physical Review B (Condensed Matter and Materials Physics) **68**, 235409 (pages 7) (2003). 37, 49

[131] Sarkar, P., Springborg, M., and Seifert, G., A theoretical study of the structural and electronic properties of CdSe/CdS and CdS/CdSe core/shell nanoparticles, Chemical Physics Letters **405**, 103–107 (2005). 37, 49

[132] Kasuya, A., Sivamohan, R., Barnakov, Y. A., Dmitruk, I. M., Nirasawa, T., Romanyuk, V. R., Kumar, V., Mamykin, S. V., Tohji, K., Jeyadevan, B., Shinoda, K., Kudo, T., Terasaki, O., Liu, Z., Belosludov, R. V., Sundararajan, V., and Kawazoe, Y., Ultra-stable nanoparticles of CdSe revealed from mass spectrometry, Nature Materials **3**, 99–102 (2004). 37, 39

[133] Katari, J. E. B., Colvin, V. L., and Alivisatos, A. P., X-ray photoelectron-spectroscopy of CdSe nanocrystals with applications to studies of the nanocrystal surface, Journal of Physical Chemistry **98**, 4109–4117 (1994). 38

[134] Spanhel, L., Haase, M., Weller, H., and Henglein, A., Photochemistry of colloidal semiconductors: 20. Surface modification and stability of strong luminescing CdS particles, Journal of the American Chemical Society **109**, 5649–5655 (1987). 39

[135] Wang, Y. and Herron, N., Quantum size effects on the exciton energy of CdS clusters, Physical Review B **42**, 7253–7255 (1990). 39, 77, 83, 85

[136] Vossmeyer, T., Katsikas, L., Giersig, M., Popovic, I. G., Diesner, K., Chemseddine, A., Eychmüller, A., and Weller, H., CdS nanoclusters - synthesis, characterization, size-dependent oscillator strength, temperature shift of the excitonic-transition energy, and reversible absorbency shift, Journal of Physical Chemistry **98**, 7665–7673 (1994). 39, 83, 85

[137] Herron, N., Wang, Y., and Eckert, H., Synthesis and characterization of surface-capped, size-quantized cadmium sulfide clusters. Chemical control of cluster size, Journal of the American Chemical Society **112**, 1322–1326 (1990). 39

[138] Farias, P. M. d., Santos, B. S., Longo, R. L., Ferreira, R., and Cesar, C. L., CdS nanoparticles: structural and energetical correlations, Materials Chemistry and Physics **89**, 21–27 (2005). 39

[139] Hines, M. A. and Guyot-Sionnest, P., Synthesis and characterization of strongly luminescing ZnS-Capped CdSe nanocrystals, Journal of Physical Chemistry **100**, 468–471 (1996). 40, 50, 65

[140] Carter, A. C., Bouldin, C. E., Kemner, K. M., Bell, M. I., Woicik, J. C., and Majetich, S. A., Surface structure of cadmium selenide nanocrystallites, Physical Review B **55**, 13822–13828 (1997). 40, 41, 50, 65

[141] Nosaka, Y. and Tanaka, H., Effect of Phenyl-Capping and Dimer Formation on the Electronic States of CdS Nanoparticles by Means of Semiempirical Molecular Orbital Calculations, Journal of Physical Chemistry B **106**, 3389–3393 (2002). 40, 70, 83, 97

[142] Rabani, E., Structure and electrostatic properties of passivated CdSe nanocrystals, The Journal of Chemical Physics **115**, 1493–1497 (2001). 40

[143] Pearson, R. G., *Chemical Hardness – Aplication from Molecules to Solids* (Whiley-VCH, Weinheim, 1997). 42, 63

[144] Brack, M., The physics of simple metal clusters: self-consistent jellium model and semiclassical approaches, Reviews of Modern Physics **65**, 677–732 (1993). 42

[145] de Heer, W. A., The physics of simple metal clusters: experimental aspects and simple models, Reviews in Modern Physics **65**, 611–676 (1993). 42, 78

[146] Turk, T., Resch, U., Fox, M. A., and Vogler, A., Cadmium benzenethiolate clusters of the various sizemolecular-models for metal chalcogenide semiconductors, The Journal of Chemical Physics **96**, 3818–3822 (1992). 43, 71

[147] Dean, P. A. W. and Vittal, J. J., $^{113}$Cd nuclear-magnetic-resonance spectroscopy study of mixed-ligand tetranuclear clusterc of the type $[Cd_4(EPh)_X(E'R)_{10-X}]^{2-}$ and of the mixed-metal Clusters $[Cd_XZn_{4-X}(SPh)_{10}]^{2-}$, Inorganic Chemistry **25**, 514–519 (1986). 43, 71

[148] Nosaka, Y., Shigeno, H., and Ikeuchi, T., Formation steps of CdS clusters in aqueous solution containing 2-mercaptoethanol, Surface Review and Letters **3**, 1209–1213 (1996). 43, 71, 98

[149] Wang, Y. and Herron, N., Nanometer-sized semiconductor clusters - Materials synthesis, quantum size effects, and photophysical properties, Journal of Physical Chemistry **95**, 525–532 (1991). 43, 71, 97

[150] Joswig, J.-O., *Theoretical studies of properties of clusters*, Ph.D. thesis, Universität des Saarlandes (2003). 45

[151] Yeh, C.-Y., Lu, Z. W., Froyen, S., and Zunger, A., Zinc-blende/wurtzite polytypism in semiconductors, Physical Review B **46**, 10086–10097 (1992). 46

[152] Roy, S. and Springborg, M., Theoretical investigation of the influence of ligands on structural and electronic properties of indium phosphide clusters, The Journal of Chemical Physics **109**, 1324–1329 (2005), feb 24. 49

[153] Roy, S. and Springborg, M., Theoretical study of structural and electronic properties of naked stoichiometric and nonstoichiometric indium phosphide clusters, Journal of Physical Chemistry B **107**, 2771–2779 (2003). 49

[154] Berendsen, H. J. C., Postma, J. P. M., van Gunsteren, W. F., DiNola, A., and Haak, J. R., Molecular dynamics with coupling to an external bath, The Journal of Chemical Physics **81**, 3684–3690 (1984). 49, 51, 89

[155] Deglmann, P., Ahlrichs, R., and Tsereteli, K., Theoretical studies of ligand-free cadmium selenide and related semiconductor clusters, The Journal of Chemical Physics **116**, 1585–1597 (2002). 50, 83

[156] Puzder, A., Williamson, A., Zaitseva, N., Galli, G., Manna, L., and Alivisatos, A., The effect of organic ligand binding on the growth of CdSe nanoparticles probed by ab initio calculations, Nano Letters **4**, 2361–2365 (2004). 50

[157] Schön, J. C. and Jansen, M., First step towards planning of synthesis in solid-state chemistry: Determination of promising structure candidates by global optimisation, Angewandte Chemie (Int. Ed.) **35**, 1286 – 1304 (1996). 51

[158] Nirmal, M., Norris, D. J., Kuno, M., Bawendi, M. G., Efros, A. L., and Rosen, M., Observation of the "Dark Exciton" in CdSe Quantum Dots, Physical Review Letters **75**, 3728–3731 (1995). 55

[159] Gorer, S. and Hodes, G., *Nanostructure and size quantization in chemical solution deposited semiconductor films*, in Kamat, P. V. and Meisel, D., (eds.) *Semiconductor Nanoclusters- Physical, Chemical, and Catalytic Aspects*, vol. 103, pp. 297–320 (Elsevier Science Publ. B V, Amsterdam, 1997). 55

[160] Schmidt, H. M. and Weller, H., Quantum size effects in semiconductor crystallites: Calculation of the energy spectrum for the confined exciton, Chemical Physics Letters **129**, 615–618 (1986). 55

[161] Rama Krishna, M. V. and Friesner, R. A., Quantum confinement effects in semiconductor clusters, The Journal of Chemical Physics **95**, 8309–8322 (1991). 55

[162] Einevoll, G. T., Confinement of excitons in quantum dots, Physical Review B **45**, 3410–3417 (1992). 55

[163] Tomasulo, A. and Ramakrishna, M. V., Quantum confinement effects in semiconductor clusters.II, The Journal of Chemical Physics **105**, 3612–3626 (1996). 55

[164] Mizel, A. and Cohen, M. L., Electronic energy levels in semiconductor nanocrystals: A Wannier function approach, Physical Review B **56**, 6737–6741 (1997). 55

[165] Ren, S.-Y. and Ren, S.-F., Total and surface density of states in CdS semiconductor clusters, Journal of Physics and Chemistry of Solids **59**, 1327–1330 (1998). 55, 69

[166] Wang, L.-W. and Zunger, A., High-energy excitonic transitions in CdSe quantum dots, Journal of Physical Chemistry B **102**, 6449–6454 (1998). 55

[167] Leung, K., Pokrant, S., and Whaley, K. B., Exciton fine structure in CdSe nanoclusters, Physical Review B **57**, 12291–12301 (1998). 55

[168] Rabani, E.and Hetenyi, B., Berne, B. J., and Brus, L. E., Electronic properties of CdSe nanocrystals in the absence and presence of a dielectric medium, The Journal of Chemical Physics **110**, 5355–5369 (1999). 55, 63, 72

[169] Perez-Conde, J. and Bhattacharjee, A. K., Electronic structure of CdTe nanocrystals: a tight-binding study, Solid State Communications **110**, 259–264 (1999). 55

[170] Franceschetti, A., Fu, H., Wang, L. W., and Zunger, A., Many-body pseudopotential theory of excitons in InP and CdSe quantum dots, Physical Review B **60**, 1819–1829 (1999). 55

[171] Joswig, J.-O., Seifert, G., Niehaus, T., and Springborg, M., Optical properties of cadmium sulfide clusters, Journal of Physical Chemistry B **107**, 2897–2902 (2003). 55, 61, 63, 77

[172] Ramaniah, L. M. and Nair, S. V., Optical absorption in semiconductor quantum dots: A tight-binding approach, Physical Review B **47**, 7132–7139 (1993). 63

[173] Haase, M. and Alivisatos, A. P., Arrested solid-solid phase-transitions in 4-nm-Diameter CdS nanocrystals, The Journal of Chemical Physics **96**, 6756–6762 (1992). 66, 69, 81

[174] Tolbert, S. H., Herhold, A. B., Johnson, C. S., and Alivisatos, A. P., Comparison of quantum confinement effects on the electronic absorption spectra of direct and indirect gap semiconductor nanocrystals, Physical Review Letters **73**, 3266–3269 (1994). 66, 69, 81

[175] Lifshitz, E., Dag, I., Litvin, I., Hodes, G., Gorer, S., Reisfeld, R., Zelner, M., and Minti, H., Optical properties of CdSe nanoparticle films prepared by chemical deposition and sol-gel methods, Chemical Physics Letters **288**, 188–196 (1998). 69, 87

[176] Lifshitz, E., Dag, I., Litvitn, I. D., and Hodes, G., Optically detected magnetic resonance study of electron/hole traps on CdSe quantum dot surfaces, Journal of Physical Chemistry B **102**, 9245–9250 (1998). 69, 87

[177] de Heer, W. A., Selby, K., Kresin, V., Masui, J., Vollmer, M., Chatelain, A., and Knight, W. D., Collective dipole oscillations in small sodium clusters, Physical Review Letters **59**, 1805–1808 (1987). 77

[178] Martins, J. L., Buttet, J., and Car, R., Electronic and structural properties of sodium clusters, Physical Review B **31**, 1804–1816 (1985). 78

[179] Seifert, G., Electronic structure and magic number of alkaline metal clusters, Zeitschrift für Physik D Atoms, Molecules and Clusters **4**, 207–208 (1986). 78

[180] Bertoncello, R., Bettinelli, M., Casarin, M., Maccato, C., Pandolfo, L., and Vittadini, A., An experimental and theoretical study of the electronic structure of zinc thiophenolate-capped clusters, Inorganic Chemistry **36**, 4707–4716 (1997). 83

[181] Samokhvalov, A., Berfeld, M., Lahav, M., Naaman, R., and Rabani, E., Assemblies of cds quantum particles studied by the attenuated low energy photoelectron spectroscopy, Journal of Physical Chemistry B **104**, 8631–8634 (2000). 89

[182] Berfeld, M., Samokhvalov, A., Naaman, R., and Lahav, M., Photoelectron transmission through "cascade-like" Langmuir-Blodgett films containing CdS quantum particles, Advanced Materials **13**, 584–587 (2001). 89

[183] Guo, S., Konopny, L., Popovitz-Biro, R., Cohen, H., Porteanu, H., Lifshitz, E., and Lahav, M., Thioalkanoates as site-directing nucleating centers for the preparation of patterns of CdS nanoparticles within 3-D crystals and LB films of Cd alkanoates, Journal of the American Chemical Society **121**, 9589–9598 (1999). 89

[184] Carrot, G., Scholz, S., Plummer, C., Hilborn, J., and Hedrick, J., Synthesis and characterization of nanoscopic entities based on poly(caprolactone)-grafted cadmium sulfide nanoparticles, Chemistry of Materials **11**, 3571–3577 (1999). 89

[185] Bu, X. H., Zheng, N. F., and Feng, P. Y., Tetrahedral chalcogenide clusters and open frameworks, Chemistry - A European Journal **10**, 3356–3362 (2004). 89

[186] Zheng, N., Bu, X., and Feng, P., Synthetic design of crystalline inorganic chalcogenides exhibiting fast-ion conductivity, Nature **426**, 428–432 (2003). 89

[187] Döllefeld, H., Weller, H., and Eychmüller, A., Particle-particle interactions in semiconductor nanocrystal assemblies, Nano Letters **1**, 267–269 (2001). 89

[188] Döllefeld, H., Weller, H., and Eychmüller, A., Semiconductor nanocrystal assemblies: Experimental pitfalls and a simple model of particle-particle interaction, Journal of Physical Chemistry B **106**, 5604–5608 (2002). 89

[189] Hagen, K. S. and Holm, R. H., Stereochemistry of $[Cd_4(SC_6H_5)_{10}]^{2-}$, A cage complex related to the cadmium cysteinate aggregates In metallothioneins, Inorganic Chemistry **22**, 3171–3174 (1983). 97

# Versicherung § 5 Abs. 1 Nr. 5

Versicherung nach § 5 Abs. 1 Nr. 5 der Promotionsordnung der Fakultät Mathematik und Naturwissenschaften an der Technischen Universität Dresden in der Fassung vom 16. April 2003:

a) Hiermit versichere ich, dass ich die vorliegende Arbeit ohne unzulässige Hilfe Dritter und ohne Benutzung anderer als der angegebenen Hilfsmittel angefertigt habe; die aus fremden Quellen direkt oder indirekt übernommenen Gedanken sind als solche kenntlich gemacht. Die Arbeit wurde bisher weder im Inland noch im Ausland in gleicher oder ähnlicher Form einer anderen Prüfungsbehörde vorgelegt.

b) Die vorliegende Arbeit wurde in der Arbeitsgruppe Theoretische Chemie am Institut für Physikalische Chemie an der Technischen Universität Dresden unter der wissenschaftlichen Betreuung von Prof. Gotthard Seifert angefertigt.

c) Hiermit versichere ich, dass ich keine früheren erfolglosen Promotionsverfahren bestritten habe.

d) Hiermit erkenne ich die Promotionsordnung der Fakultät Mathematik und Naturwissenschaften an der Technischen Universität Dresden in der Fassung vom 16. April 2003 an.

Datum Unterschrift